TÉCNICO LISBOA

Modelling and Validation of Finite Element Structural Analysis of ISTSat-1

Leonard de Barros Pacheco Seara de Sá

Thesis to obtain the Master of Science Degree in

Aerospace Engineering

Supervisor: Prof. Luís Alberto Gonçalves de Sousa
Prof. João Paulo Lopes Monteiro

Examination Committee

Chairperson: Prof. Afzal Suleman
Supervisor: Prof. Luís Alberto Gonçalves de Sousa
Member of the Committee: Prof. Hugo Policarpo
Member of the Committee: Prof. Aurélio Lima Araújo

December 2021

I declare that this document is an original work of my own authorship and that it fulfils all the requirements of the Code of Conduct and Good Practices of the Universidade de Lisboa.

Acknowledgments

First of all, I would like to thank my supervisor, Professor Luís Sousa, for all his availability, tips, suggestions and help given for the last year. His input and guidance were essential for the writing of this document.

To the team at ISTSat, with whom I've being working for the last two years, I would like to thank their constant willingness to help, for answering time and time again all my doubts and questions, for their support during the experimental tests and overall companionship in this project. I wish to give special thanks to team leader João Paulo Monteiro for his guidance and for overseeing this work alongside Professor Luís Sousa.

I would also like to extend my gratitude to ESA, for their support through the FYS program throughout these two years and for giving me the opportunity to perform a vibration test at ESA's ESEC facilities, as this test campaign, while not the focus of the present work, became the foundation of the work done during this thesis.

Finally, I would like to thank my family and my friends for their constant support for the last five years.

Resumo

É apresentado neste trabalho um *CubeSat* desenvolvido e construído por estudantes da Universidade de Lisboa, com o objetivo de demonstrar um recetor e antena de sinal ADS-B (*Automatic Dependent Surveillance - Broadcast*).

É apresentado um modelo de Elementos Finitos do CubeSat, incluindo todas as decisões, premissas e simplificações feitas e os elementos e condições fronteira usados. Uma análise estática é realizada, demonstrando que o *CubeSat* suporta as cargas dinâmicas (convertidas em estaticamente equivalentes) durante o lançamento. São realizadas análises modais, providenciando os modos do *CubeSat*, tanto para correlação como para demonstrar que a frequência fundamental se encontra acima do nível de frequência exigido pela autoridade responsável pelo lançamento.

Os procedimentos e configurações de uma campanha de testes modais com martelo de impacto são explicados e os dados experimentais obtidos são apresentados, mostrando-se a boa qualidade dos mesmos. As frequências naturais, modos de vibração e os coeficientes de amortecimentos são extraídos com recurso a um algoritmo de extração modal.

Por último, os modos experimentais são comparados com os modos computacionais com recurso ao MAC (*Modal Assurance Criterion*) no intervalo [0,1400] Hz. Conclui-se que o Modelo de Elementos Finitos apresenta boa correlação até aos 1000 Hz, apesar de algumas discrepâncias, e aumentando a confiança no modelo de Elementos Finitos. Também é demonstrado que é viável o uso de martelos de impacto para testar *CubeSats* e validar modelos de Elementos Finitos, reduzindo a necessidade de testes de verificação demasiado agressivos, que acarretam o risco de danificar o *CubeSat* antes do lançamento.

Palavras-chave: *CubeSat*, Análise Estrutural, Método dos Elementos Finitos, Teste Modal, Validação

Abstract

In this work, it is presented a student developed and built CubeSat, from the University of Lisbon, meant to demonstrate a compact Automatic Dependent Surveillance - Broadcast receiver and antenna.

A Finite Element model of the CubeSat is shown, including all decisions, assumptions and simplifications made, and elements and boundary conditions used. A static analysis is performed, demonstrating that the CubeSat can endure the dynamic loads (converted into statically equivalent) during launch. Modal analyses are also conducted, providing the CubeSat's modes, both for correlation purposes and to demonstrate that the fundamental frequency is above the frequency level required by the authorities responsible for the launch.

The procedures and set-up of an impact hammer modal test campaign are explained, the experimental data is presented, and its good quality is shown. The natural frequencies, damping coefficients and mode shapes are extracted from the experimental data with the use of a modal fitting algorithm.

Finally, the experimental modes are correlated to the computational modes with the Modal Assurance Criterion in the [0-1400] Hz range. It is concluded that, despite some issues and discrepancies, the Finite Element model shows good correlation up to 1000 Hz, increasing confidence in the CubeSat's Finite Element model. It is also demonstrated that it is feasible to test CubeSats through impact testing and validate its Finite Element model, reducing the need for aggressive verification tests that have a risk of overstressing and damaging the CubeSat before launch.

Keywords: CubeSat, Structural Analysis, Finite Element Method, Modal Testing, Validation

Contents

Acknowledgments v
Resumo vii
Abstract ix
List of Tables xv
List of Figures xvii
Nomenclature xxi
List of Abbreviations xxv

1 Introduction **1**
1.1 Motivation and Background 1
1.1.1 CubeSats 2
1.1.2 ISTSat Team 3
1.1.3 Standards 4
1.2 Objectives and Deliverables 5
1.3 Thesis Outline 5

2 State of the Art **7**
2.1 Finite Element Analysis 7
2.2 Experimental Testing 9
2.3 Correlation and FE model Validation 9

3 Theoretical and Experimental Background **11**
3.1 Solid Mechanics 11
3.1.1 Displacement 11
3.1.2 Strain 12
3.1.3 Stress 12
3.1.4 Constitutive Equation 13
3.1.5 Equilibrium Equation 14
3.2 Equation of Motion 14
3.2.1 Static Analysis 15
3.2.2 Modal Analysis 15
3.3 Linear vs Nonlinear Analysis 18

3.4 Bolted Joints . . . 19
3.5 Response in Time and Frequency Domains . . . 19
3.5.1 Frequency Response Function . . . 20
3.5.2 H_1 Estimators . . . 22
3.5.3 Coherence Function . . . 22
3.5.4 Leakage and Windows . . . 23
3.6 Modal Testing . . . 25
3.6.1 Excitation Input . . . 25
3.6.2 Excitation Output and Sensor . . . 28
3.6.3 Free-free Condition . . . 29
3.6.4 Pre-test Planning . . . 29
3.6.5 Modal Fitting . . . 30
3.7 Correlation Metrics . . . 30
3.7.1 Modal Assurance Criterion . . . 31

4 Modelling and FE Analysis **32**
4.1 System Description . . . 32
4.1.1 Structure . . . 32
4.1.2 PCB Stack . . . 34
4.1.3 Solar Panels and Antennas . . . 35
4.2 CAD Modelling . . . 36
4.2.1 Idealization . . . 36
4.3 FEM Modelling . . . 40
4.3.1 Materials . . . 40
4.3.2 Elements . . . 41
4.3.3 Mesh and Convergence Study . . . 45
4.3.4 Loads and Boundary Conditions . . . 48
4.3.5 Errors . . . 50
4.4 FEA Results . . . 50
4.4.1 Linear Static Analysis . . . 51
4.4.2 Modal Analysis . . . 53

5 Modal Test **57**
5.1 Test Description and Procedure . . . 57
5.1.1 System Under Test . . . 57
5.1.2 Test Set Up . . . 58
5.1.3 Accelerometers Positions and Impact Locations . . . 60
5.1.4 Errors and Discrepancies . . . 61
5.2 Experimental Results . . . 62
5.2.1 Payload Subsystem . . . 62

5.2.2 +Y Solar Panel . . . 63
5.2.3 EPS Subsystem . . . 63
5.3 Modal Fitting . . . 64
5.3.1 Payload Subsystem . . . 65
5.3.2 +Y Solar Panel . . . 66
5.3.3 EPS Subsystem . . . 67

6 FE-Experimental Correlation **68**
6.1 Model Reduction and Expansion . . . 68
6.2 Frequency Comparison and MAC . . . 68
6.2.1 PL . . . 69
6.2.2 +Y Solar Panel . . . 71
6.2.3 EPS . . . 72
6.3 Discussion of Results . . . 72

7 Conclusions **74**
7.1 Achievements . . . 75
7.2 Future Work . . . 75

Bibliography **77**

A Hard mounted configuration modes **A.1**

List of Tables

4.1 ISTSat-1 materials' mechanical properties. 41
4.2 Convergence of stress near bolt hole - absolute values (MPa) and relative variations (%). 46
4.3 ISTSat-1 main modes in hard-mounted configuration. 54
4.4 PL modes in free-free condition. 56
4.5 EPS modes in free-free condition. 56
4.6 +Y SP modes in free-free condition. 56

5.1 PL extracted modes' frequencies and damping coefficients. 65
5.2 +Y SP extracted modes' frequencies and damping coefficients. 66
5.3 EPS extracted modes' frequencies and damping coefficients. 67

6.1 PL modes' frequencies comparison. 71
6.2 +Y SP modes' frequencies comparison. 72
6.3 EPS modes' frequencies comparison. 73

List of Figures

1.1 P-POD CAD model. 2
1.2 ISTSat-1. 4

2.1 Correlation and model updating procedure diagram. 10

3.1 Stress components representation. 13
3.2 Mass-spring-damper system. 14
3.3 Material behaviour: strain-stress curve. 19
3.4 Example function in time domain. 20
3.5 Example function in frequency domain. 20
3.6 FRF schematic. 21
3.7 Example FRF obtained experimentally in real-imaginary form. 21
3.8 Example FRF obtained experimentally in amplitude-phase form. 22
3.9 H_1 estimator - system schematic. 22
3.10 Example coherence function. 23
3.11 Impact force input in the time domain and use of square window. 24
3.12 Impact excitation response in time domain and use of exponential window. 25
3.13 Impact hammer. 26
3.14 Hammer impact in the time domain. 26
3.15 Hammer impact in the frequency domain. 26
3.16 Shaker at ESA ESEC facilites. 27
3.17 Accelerometer on vibrating beam. 28
3.18 Example MAC representation. 31

4.1 ISTSat-1 exploded view. 33
4.2 ISTSat-1 side frames. 33
4.3 ISTSat-1 arm links. 33
4.4 ISTSat-1 axes. 34
4.5 ISTSat-1 PCB stack. 34
4.6 ISTSat-1 EPS and battery atack. 35
4.7 ISTSat-1 PL board. 35
4.8 ISTSat-1 solar panel. 36

4.9 ISTSat-1 ADS-B antenna. 36
4.10 ISTSat-1 idealized side frames. 37
4.11 ISTSat-1 idealized arm links. 37
4.12 ISTSat-1 idealized TTC PCB. 39
4.13 ISTSat-1 idealized EPS PCB. 39
4.14 Idealized model. 40
4.15 Comparison of CHEXA and CTETRA elements on a hole (with identical conditions). . . . 42
4.16 Bolt connection between the solar panel and side frame. 44
4.17 Concentrated mass element and rigid connections to CubeSat structure. 44
4.18 Mesh evolution around bolt hole. 46
4.19 Convergence of stress near bolt hole. 47
4.20 Idealized model converged mesh. 47
4.21 Static analysis: Z axis. 51
4.22 Static analysis: Y axis. 52
4.23 Static analysis: X axis. 52

5.1 Test set-up. 58
5.2 Test set-up schematic. 58
5.3 Test set-up: fishing line SP testing configuration. 58
5.4 Test set-up: fishing line PL testing configuration. 58
5.5 Accelerometer positions in +Y SP. 60
5.6 +Y SP: auto-MAC matrix. 60
5.7 Accelerometer positions in PL. 61
5.8 Accelerometer position in EPS. 61
5.9 Coherence: PL. 62
5.10 FRF (Amplitude/Phase form): PL position 1. 62
5.11 FRF (Real/Imaginary form): PL position 1. 62
5.12 Coherence: +Y SP. 63
5.13 Hammer impact in the time domain: +Y SP position 1. 64
5.14 Hammer impact in the frequency domain: +Y SP position 1. 64
5.15 FRF: EPS position 1. 64
5.16 Coherence: EPS position 1. 64
5.17 Experimental and reconstructed FRFs: PL position 1. 65
5.18 Experimental and reconstructed FRFs: +Y SP position 8. 66
5.19 EPS experimental and reconstructed FRFs: position 1. 67

6.1 MAC of all PL modes. 69
6.2 FEA PL mode 8: 1280.8 Hz. 70
6.3 FEA PL mode 9: 1352.5 Hz. 70
6.4 FEA PL mode 1: 407.9 Hz. 70

6.5 FEA PL mode 2: 631.2 Hz. 70
6.6 MAC of selected PL modes. 70
6.7 MAC of all +Y SP modes. 71
6.8 MAC of selected +Y SP modes. 72

A.1 ISTSat-1 Mode 1: TTC (Hard mounted configuration). A.1
A.2 ISTSat-1 Mode 2: COM (Hard mounted configuration). A.1
A.3 ISTSat-1 Mode 6: PL (Hard mounted configuration). A.2
A.4 ISTSat-1 Mode 8: $\pm$X Solar Panels (Hard mounted configuration). A.2
A.5 ISTSat-1 Mode 9: $\pm$Y Solar Panels (Hard mounted configuration). A.2
A.6 ISTSat-1 Mode 11: -Z Patch Antenna (Hard mounted configuration). A.2
A.7 ISTSat-1 Mode 14: +Z Solar Panel (Hard mounted configuration). A.3
A.8 ISTSat-1 Mode 15: PCB Stack (Hard mounted configuration). A.3

Nomenclature

Greek symbols

γ	Coherence
ν	Poisson's ratio
ω	Angular frequency
Φ	Modal matrix
ϕ	Modal vector
ρ	Density
σ	Cauchy stress tensor
τ	Time constant
ε	Strain tensor

Roman symbols

A	Area
d	Diameter
F	Load
K	Coefficient
P	Pitch thread
T	Torque
$\mathfrak{F}$	Dissipative function
$\overline{L}$	Coefficient vector
$\overline{r}$	Influence vector
C	Damping matrix
c	Damping coefficient

f	Force
f	Frequency
K	Stiffness matrix
k	Stiffness
M	Mass matrix
m	Mass
T	Kinetic energy
t	Time
U	Elastic potential energy
W	Work
X	Amplitude
J	LSRF cost function
W	LSRF cost function weight
K	Safety factor
C	Elasticity tensor
E	Young's modulus
f	Body force
G	Shear modulus
u	Displacement
x	Position
H	Frequency Response Function
N	Noise
N	Samples
S	Spectra
X	Complex element of finite discrete sequence
x	Element of finite discrete sequence

Subscripts

0	Initial

eff Modal effective

EXP Experimental

f Final

FE Computational

PL Pre load

q Modal

r Estimated rational function

T Torque

t Tensile

VM Von Mises

x, y, z Cartesian components

XX Input

XY Cross

y Yield

YY Output

Superscripts

H Conjugate transpose

T Transpose

List of Abbreviations

1/2/3/6U	1/2/3/6 Unit CubeSat
ADCS	Attitude Determination and Control System
ADS-B	Automatic Dependent Surveillance - Broadcast
CAD	Computer Aided Design
CDS	CubeSat Design Specification
COM	Communications Processor and Data Storage
COTS	Component of the Shelf
DFT	Discrete Fourier Transform
DLL	Design Limit Loads
DoF	Degree of Freedom
ECSS	European Cooperation for Space Standardization
EPS	Electrical Power Supply
ESA	European Space Agency
FE	Finite Element
FEA	Finite Element Analysis
FEM	Finite Element Method
FFT	Fast Fourier Transform
FRF	Frequency Response Function
FT	Fourier Transform
FYS	Fly Your Satellite
IST	Instituto Superior Técnico
LSRF	Least Squares Rational Function
MAC	Modal Assurance Criterion
MDoF	Multiple Degree of Freedom
NCO	Normalized Cross-Orthogonality
OBC	On-Board Computer
OMA	Operational Modal Analysis
P-POD	Poly-Picosatellite Orbital Depolyer
PCB	Printed Circuit Board

PE	Polyethylene
PL	Payload
PPS	Polyphenylene Sulfide
PTFE	Polytetrafluoroethylene
RBF	Remove Before Flight
SDoF	Single Degree of Freedom
SP	Solar Panel
TTC	Telemetry, Tracking and Communications
V/UHF	Very/Ultra High Frequency

Chapter 1

Introduction

1.1 Motivation and Background

During their missions, but especially during launch, all satellites are submitted to extreme mechanical loading conditions (steady-state acceleration, low frequency vibration, random vibration, shock). As such, it is necessary to guarantee that both the structure and all other satellite subsystems can endure these loads, and do not break and put the mission at risk of failure. Considering this and the extremely high cost associated with each launch and satellite operation, despite recent reductions [1], very strict verification tests are performed before any launch, submitting the satellite to similar or even more aggressive conditions than the ones that will be experienced during its lifetime. By testing above the levels experienced during launch and having such a conservative approach, one can have confidence that the satellite will endure the launch and safely reach space. However, this may lead to overtesting of the satellite to be launched, resulting in damage, wasted resources, and loss of time, and is a relevant issue that is currently being looked into [2].

Alternatively, the Finite Elements Method (FEM) is a powerful tool that allows one to computationally perform structural analysis and obtain a high amount of results and data in a shorter time and with fewer resources than if one were to try to obtain the same results in a laboratory. However, FEM programs are just code that take the input provided by the designer, apply all the model equations and mathematical methods, and return outputs, as long as the user does not forget to input all necessary data or no mathematical error occurs. These programs cannot verify the approximations and simplifications done during modelling and whether the model represents faithfully what happens in reality. The results can only be verified by the designer himself.

As such, it is of utmost importance to validate the Finite Element (FE) model, to guarantee that the assumptions and decisions made during the analysis were good enough. This validation is done by performing experimental tests (using shakers, impact hammers, among others), comparing through various methods the experimental and computational results, and correcting and fine-tuning the FE model to better reflect the approximation to the real system. This raises confidence in all model's results, including results that cannot be obtained experimentally, and also on models that might be slightly different

but are based on the same assumptions.

That raise in confidence in the computational results allows for the implementation of less strict verification tests before launch with the advantage of reducing costs and lowering the risk of overtesting the satellite.

In this work, this combined methodology of FEM, testing, and validation is applied to a University CubeSat project.

1.1.1 CubeSats

Satellites can be divided into categories according to various criteria: the type of mission (science, communication, military, etc.), public or private, or as a function of their size and mass. Satellites that have between 1 and 10 kg are called nanosatellites [3].

CubeSats are nanosatellites that adhere to a standard size and form factor defined by the CubeSat Design Specification (CDS), developed by California Polytechnic State University (CalPoly) and Stanford in 1999 [4]. The unit size of a CubeSat is a 10 cm side cube, called 1U, with a mass of up to 2kg. The most common CubeSats sizes are 1U, 2U or 3U.

During the launch, the CubeSats are transported inside a deployer, which besides carrying the CubeSat, also protects and releases it into space when appropriate. The first deployer available was the Poly-Picosatellite Orbital Deployer (P-POD) (see Figure 1.1), with a rail design and space for 3U, developed by CalPoly. Inside the deployer are a total of four rails, where the CubeSat will fit. On one end of the P-POD there is a door through which the CubeSats will first be inserted, before launch, and will then be ejected during deployment. On the opposing end, the CubeSats rest on a plate connected to a spring. When the P-POD is closed, the spring is compressed, which provides the deployment force necessary to eject the CubeSats from the P-POD once the door is opened.

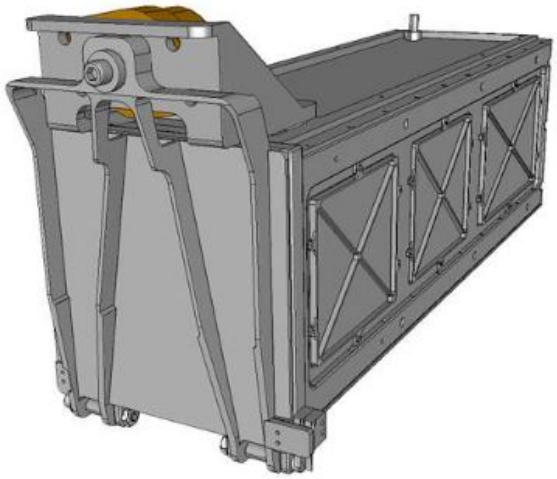

Figure 1.1: P-POD CAD model [4].

The intention of this standard is to simplify development, provide safe deployment and operation, reduce costs and time and make space more accessible. This type of satellite is rather popular among universities for its lower complexity and costs, but it has also been adopted by industry and government

organizations. The standardization of the design also makes possible the mass production of components and for companies to offer off-the-shelf components (COTS) which can easily be integrated on the CubeSats, making investments in the CubeSat market more attractive. By being cheaper, one can have a larger number of satellites for the same price as a large satellite, allowing for an easier set-up of a constellation, covering larger areas. Their small size also allows CubeSats to more easily fit and hitch rides as secondary loads on rockets transporting other cargo, eliminating the need for a special launch just for it and dramatically reducing costs. On the other hand, their small size also brings some restrictions and drawbacks. The reduced available space for systems puts a limit on the complexity and number of subsystems on board. By being mostly secondary cargo, the launch of CubeSats is highly dependent on the schedule of other missions [5].

The first CubeSat was launched in 2003, up to 2012 one hundred had been launched, and as of January 2021, 1357 CubeSats have been put in orbit showing the quick adoption and growth of the segment [6, 7]. A detailed and thorough State of the Art about CubeSats, other small spacecraft and their various subsystems, as of 2020 and compiled by NASA, can be seen in [8].

1.1.2 ISTSat Team

ISTSat is a team of students, professors, researchers and radio amateurs based at Instituto Superior Técnico (IST), University of Lisbon, that develops CubeSats. It was created in 2008 when a satellite tracking station was developed at IST's Taguspark campus, it operated nanosats for a couple of years and has since then begun to develop its first CubeSat, ISTSat-1 [9].

ISTSat-1 is not only the first CubeSat developed by the ISTSat team but also the first university CubeSat project developed in Portugal. It is a 1U CubeSat and contrary to the common practice of buying COTS that are already prepared to be integrated, reducing cost and development time, most ISTSat-1 subsystems have been designed and built in-house, maximizing the educational return.

ISTSat-1 is meant to demonstrate a compact Automatic Dependent Surveillance - Broadcast (ADS-B) receiver and antenna, used to track the position and status broadcast by commercial aircraft and extend aircraft surveillance beyond line-of-sight communications. ADS-B systems have many advantages, namely, not being encrypted and being available to everyone; continuous transmission; and providing information to the pilots in real-time. The use of space-based ADS-B has been discussed and demonstrated since the late 2000s, but the use of a 1U form factor has not been done. The use of this technology in CubeSats would allow the tracking of aircraft in the middle of the oceans, where it is not possible to have coverage by land stations, at a much lower cost [9]. Besides the innovations related to the ADS-B, ISTSat-1 also features the use of redundant communications mechanisms, software-based radiation mitigation strategies and an integrative testing process.

ISTSat-1 is compatible with a rail design deployer and is composed of multiple subsystems (see Figure 1.2). On the interior of the satellite, various subsystems form a PCB stack connected by four axes, that are kept in place by the structure. On five sides of the satellite, there are solar panels, attached to the structure and connected to the PCB stack. Finally, on the side without a solar panel

there is a patch antenna and below one of the solar panels, and opposite of the patch antenna, there is a V/UHF antenna. A more detailed view and description of the system is provided in chapter 4.

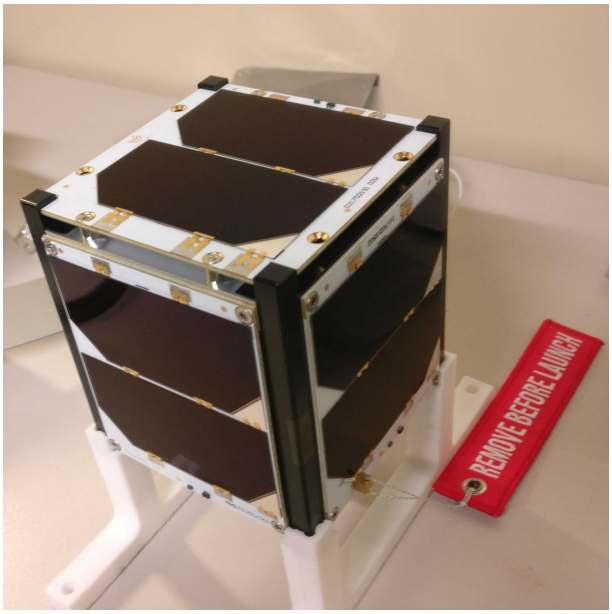

Figure 1.2: ISTSat-1.

In 2017 the ISTSat team was accepted and has, since then, been part of the European Space Agency's (ESA) "Fly your Satellite!" (FYS!) program, a program developed by ESA that supports the development of University-based CubeSats, providing technical guidance and support and arranging the launch of the CubeSats into orbit.

Throughout 2020 and 2021, there have been multiple test campaigns at system and subsystem level, including a vibration test in August 2020 at ESA's facilities, to qualify the satellite for launch. These tests could be alleviated if the ISTSat-1's FE model was validated.

ISTSat-1 is expected to be launched in 2022.

1.1.3 Standards

As part of an ESA programme, the ISTSat team follows the European Cooperation for Space Standardization (ECSS) standards. These were also loosely followed in this work.

The ECSS is a joint effort between ESA, national space agencies and the European industry for the creation of common standards for Europe, allowing easier cooperation between the various actors and gains of efficiency. The ECSS standards broach a wide range of topics.

ECSS-E-HB-32-26A [10] reviews spacecraft mechanical loads analysis and launcher/spacecraft couple loads analysis, presents a background on structural dynamics and discusses the specifics of the loads felt during launch, including static, sine and random vibration loads, and is fundamental for the set-up of both the FE model and the verification tests loads.

The general requirements of structural FE models for space components, the more common model checks and test-analysis correlation are mentioned in ECSS-E-ST-32-03C [11].

ECSS-E-ST-10-03C [12] details the general requirements for testing (mechanical, thermal, electrical, among others) in the space industry and more specific requirements for space segment equipment and space segment element tests; and ECSS-E-ST-32-11C [13] identifies the main objectives, requirements, procedures and pre-test analysis of modal survey tests in space programs, so that data is obtained allowing for the correct identification of the dynamic characteristics of the test item, which then might be used for the correlation with the FE model.

1.2 Objectives and Deliverables

The main goal of this thesis was to create and validate the ISTSat-1 FE model through experimental testing and increase confidence in the results obtained from it.

It is important to note that, at the time of writing of this document, the entire CubeSat was already completely designed and built. As such, the modelling and analysis process described in this work were not meant to study and compare different CubeSats designs nor to lead to any major design changes whatsoever. The real model was fixed and only the modelling assumptions could be changed.

Therefore, this thesis had the following objectives:

- create a new and updated FE model of the ISTSat-1 based on the modelling and structural analysis performed previously at the ISTsat team [14];
- obtain the FE results for the new and updated levels required by the launch authority;
- provide data for the verification campaign required by ESA and the launch authorities for the launch of ISTSat-1;
- deliver a validated satellite FEM model;
- provide a foundation for the structural modelling and analysis methods for future CubeSats developed by the ISTSat team, such as the ISTSat-Q, which is at the beginning of development. This would allow for a more usual design process, where a more complete structural analysis is obtained before manufacturing, leading to a structure optimization and where correlations procedures can be immediately conducted as prototypes are built;
- Demonstrate the feasibility of CubeSat modal testing through the use of impact hammers to extract modal parameters, reducing the need for tests with risk of overtesting.

1.3 Thesis Outline

This thesis is divided into 7 chapters.

In chapter 1, the current chapter, the motivation for this work and brief introductions to CubeSats and ISTSat are presented.

In chapter 2 the state of the art in the structural analysis, testing and validation of University-based CubeSats, and computational-test correlation in the industry is given.

In chapter 3 a brief theoretical background on structural analysis, FEM correlation and some experimental concepts are presented.

Chapter 4 focuses on the FE Analysis. The system is described in a more detailed manner, with a focus on each subsystem, all problem conditions, assumptions and approximations are stated and the main computational results are shown.

In chapter 5 the test procedure is detailed and the experimental results are presented. Furthermore, it is shown how and which modal parameters were extracted from this data.

In chapter 6, the correlation of FE and experimental results is made, the results are discussed and it is shown that the FE model represents reality accurately enough, despite not fully meeting the ECSS standards requirements.

Finally, in chapter 7 the conclusions and main achievements of this work are presented and some potential future developments and work ideas are suggested.

Chapter 2

State of the Art

This chapter provides a literature review of current approaches to structural analysis in University CubeSat projects as well a wider view on model testing and correlation in the space and other industries.

2.1 Finite Element Analysis

FEM is a numerical methodology used to solve differential equations in a continuous domain. In most cases, it is highly complex, inconvenient or even impossible to analytically solve these equations and obtain solutions, either due to complex geometries or boundary conditions. With FEM, a domain is discretized into a collection of subdomains and the differential equation is solved in each subdomain by some variational method. This discretization makes it easier to approximate a complex function by polynomials in each subdomain, which is called 'finite element' (FE). The combined set of FE is called 'mesh'. This way, a problem in a continuum with an infinite number of points is replaced by a mesh with a finite number of elements. Each element is composed of nodes, corresponding to the points where elements are connected and where compatibility between them is verified, so that the entire domain behaves as a single structure, despite being divided into various elements [15]. Each node has associated degrees of freedom (DoFs), i.e., a value that may vary and is independent of the other values. For a 3-dimensional problem, there are a total of six DoFs for each node, three of translation and three of rotation. The FEM can usually be divided into the following steps [16]

- Definition and modelling of the problem, resulting in a differential equation and some boundary conditions;
- Discretization of the domain into finite elements, also known as meshing;
- Derivation of the equations and choice of approximate functions for each element;
- Assembly of all the element equations, obtaining a system for the whole body;
- Imposition of the boundary conditions;
- Solution of the obtained system;

- Post processing of the results, obtaining gradients and other results derived from the main output, plots, videos, among others.

The study of a problem with FEM is called Finite Element Analysis (FEA). Typical uses of FEA include structural static/dynamic analysis, heat flow, aeroacoustics. It can also be used directly in discrete systems, such as a collection of springs.

FEM has many advantages that have made it a very popular and used tool in the industry: result estimates can be obtained before any physical model is built and money is spent; it allows for the quick variation of variables and the study of the impact of these variations (sensitivity analysis); the obtained data is not spatially restricted by the placement of sensors or other instruments; and it is possible to directly obtain data that experimentally can only be obtained indirectly.

However, caution should always be used with FEM. As the FEA programs are improved and become more user-friendly, a tendency for these to become a succession of button clicking without an understanding of the theory and processes happening in the background is becoming more prevalent. If incorrect input is provided to the program, as Adams and Askenazi [17] put it, ”no matter how sophisticated the program, garbage in will always equal garbage out”. Careful analysis of the results and common checks should always be performed and blindly accepting the output results should never happen. FEM models are based on mathematical models, which are used as an approximation of the real components. It is the responsibility of the designer to be aware of the differences. One has to always be aware of the errors existent in the analysis, which sometimes are impossible to eliminate completely, and that may result from the approximations done or might arise from computational limitations.

Due to the mentioned advantages and continued developments in accessible FEA software, FE structural analysis has become one of the main tools in University CubeSat projects.

In some projects, still in an initial phase, FEA was used for the study of individual components of the CubeSats, namely the structure [18, 19] and the PCB boards [20].

Other teams, at a more advanced stage, simulated the entire CubeSat, with all subsystems and connections included. The most typical analyses conducted by university teams are static and modal analyses [21], to verify that the CubeSats endure the static loads and that the frequency of the first mode is above the frequency required by launch authorities; random vibration analysis [22, 23] must be performed, to verify that the stresses developed during launch do not cause yielding or fracture of the material. In all these projects it was seen that, according to the FEA results, the components or CubeSat were able to meet all launch authority requirements and survive the launch, with, typically, significant margins in deformations, stresses and frequencies.

At the ISTsat team itself, all structural analyses performed until now, namely static, modal and random vibration analyses, have been with resort to FEA [14].

However, no actual testing of the components and CubeSats was performed in these teams. Due to the costs and time associated with experimental testing, the absence of access to facilities that would allow this type of testing or the development of the CubeSat still being in an early phase without an actual spacecraft to test, the execution of experimental tests is more uncommon.

2.2 Experimental Testing

In the space industry, experimental testing is of paramount importance and a fundamental part of the design process.

No satellite is launched to space without undergoing first an intensive test campaign regarding the structural and thermal behaviour, but also electronics, communications and software. While the FEA provides good estimates of many results, it is the experimental testing that additionally proofs the system's readiness for launch and operations.

There are multiple phases of testing, depending on the design phase. The levels and procedures done in each phase might vary and the test levels may be classified as qualification and verification levels.

Qualification testing is meant to prove that the systems are working as intended, that all requirements are being fulfilled and that the design is fail-safe. This type of testing is done in an earlier phase and might lead to design corrections [12]. Verification testing is done when the design has been frozen and no further changes are expected. The maximum and worst case scenario levels that might be found during the lifetime of the mission, from launch until decommission, plus a safety margin, are used in this type of testing. It verifies that the system was well manufactured and will sustain the entire mission's operating conditions [24].

Despite the constraints mentioned before that limit experimental testing by university CubeSat teams, some teams have performed vibration or similar tests to assess the structural integrity, showing that the CubeSats did not get damaged during tests [25–28]. However, in none of these teams, the results of the experimental tests were used to improve and validate FE models. The CubeSat was either only tested and verified that it withstood the required loads, or when a FE model was used, it served only for an initial guess of the response, to verify that was ready for the vibration tests.

2.3 Correlation and FE model Validation

The results obtained from the FEA and the experimental testing can be compared. This is known as correlation. Correlation can be used, on one hand, to quantify how closely related, how much of an error exists and study which criteria are best to correlate sets of experimental and computational results; and on the other hand, to use that quantification to update and correct the computational model and improve the correlation level [29]. In figure 2.1 a diagram representing the overall sequence followed during a correlation process can be seen.

From the FEM, various types of analysis (such as modal analysis) are performed and results are obtained. Most correlation criteria require both sets to be correlated to have the same size. Since the FEA model tends to have a greater number of DoFs, it becomes necessary to reduce it so that it has the same amount of data points and becomes possible to compare in a balanced form the two sets of results. Otherwise, the test set might be expanded, but it is less usual, as it would require using the FEA to expand the test results, biasing these.

During testing, sensors (such as accelerometers) are used to obtain experimental data. This data can be used directly or be manipulated and presented in alternative forms (e.g., frequency response functions), from which additional results can be obtained in post-testing procedures.

If the objective is only to quantify the correlation level, the procedure stops at 'Correlation criteria'. Otherwise, the 'FE model update' loop is performed as many times as necessary until a satisfactory level of correlation is attained.

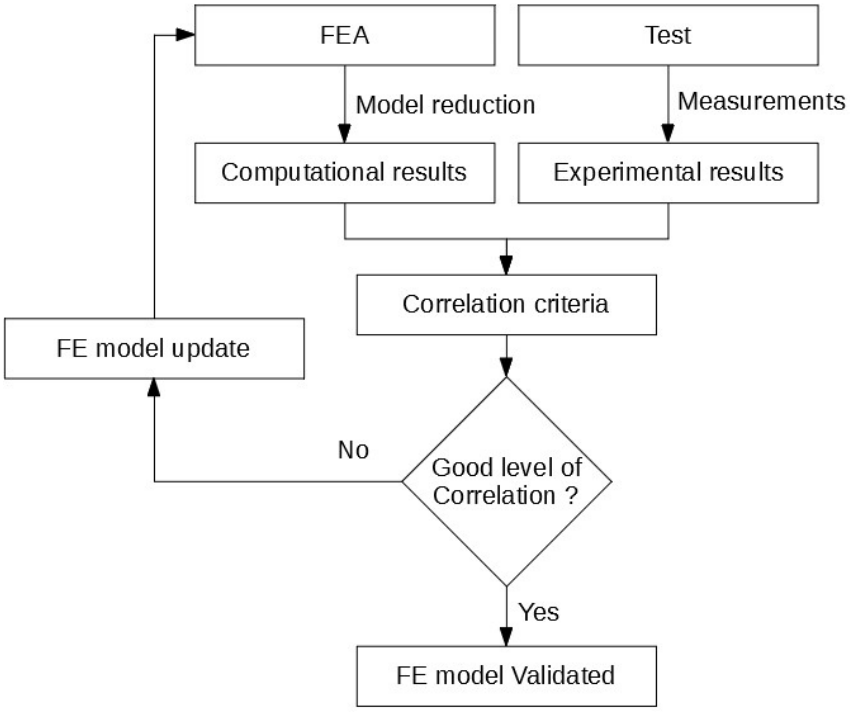

Figure 2.1: Correlation and model updating procedure diagram.

While various criteria can be used, the most common correlation criterion is the Modal Assurance Criterion (MAC, explained in chapter 3), that was first developed in 1980 [30].

To obtain good results with correlations criteria, care has to be taken in all steps of the methodology, both on the FE and test segments. To extract good quality measurements from an experimental test for correlation purposes, a strategy based on five criteria (sensor location, excitation type, measurement locations, sensor section and excitation location) was suggested, from which resulted a numerically efficient procedure for the selection of the sensor positions [31].

University wise, while it is rarer, some teams have correlated experimental and computational results through the use of correlation criteria, namely the MAC, validating the developed FE model [32].

FE validation has been done on various space missions, such as ESA's BepiColombo spacecraft, where besides the validation itself, the study of the quality of various reduction algorithms such as Guyan reduction [33] or the SEREP method [34] is made [35] and mode selection criteria, such as modal effective mass and modal kinetic energy fraction and modal strain energy fraction, are analysed [36, 37]; but it is not limited to the space industry, having also been applied to wind turbines [38] and bridges [39].

Chapter 3

Theoretical and Experimental Background

In this chapter, an overview of the theoretical and experimental background and concepts necessary for this thesis is provided. As necessary, references are provided for further reading of the topics here mentioned.

3.1 Solid Mechanics

Space is a continuum, since between any two points, no matter how close, exist an infinite number of points. Matter and bodies, however, are not, as they are constituted by a set of atoms, with empty space between them. Nevertheless, if one studies matter at a macroscopic level, with characteristic dimensions significantly above atomic distances, a material or a body can be considered to be a continuum and to be distributed uniformly across space. This allows matter to be divided into an infinite number of points and properties can be defined in all of them. The branch of mechanics that models a body as a continuum is called Continuum Mechanics, with the study of solid continuum bodies known as Solid Mechanics. For a deeper understanding of the topics of this section, see [40–42].

3.1.1 Displacement

When a body is in rest or in the undeformed position, each point of the body will have some initial position, x_0. Once forces are applied to the body, it will deform and each body point will have some new position, x_f. The difference between the initial and this new position is called displacement, u, which is a continuous function of space and time. The displacement of generic point a is given by

$$u(a,t) = x_f(a,t) - x_0(a,t)\,. \tag{3.1}$$

If displacement is constant across the body, then it corresponds to a rigid body movement, that is, there is no relative displacement between all body points.

3.1.2 Strain

Since the displacement itself does not characterize a material, strain, which is adimensional, is used instead and represents the ratio between displacement and some reference length.

If small displacements (compared to the body dimensions) are considered, the strain tensor, ε_{ij}, can be related to the displacements by the expression

$$\varepsilon_{ij} = \frac{1}{2}\left(\frac{\partial u_i}{\partial x_j} + \frac{\partial u_j}{\partial x_i}\right), \tag{3.2}$$

where $i, j = x, y, z$, the three Cartesian coordinate axes.

The strain is usually divided into two components, the normal and shear strain, which cause compression/extension and distortion, respectively.

The strain can be defined at any point of a body and may vary in space and time.

The relationship between the strain in the directions i and j is given by the Poisson's ratio, ν,

$$\nu_{ij} = \frac{\varepsilon_{ii}}{\varepsilon_{jj}}, \tag{3.3}$$

and indicates how much a material compresses in one direction when expanded in another. While some materials might have negative ratios, the most common is for this value to be in the 0-0.5 range (e.g, steel has ν equal to 0.3).

3.1.3 Stress

When a body is subjected to forces and deforms it develops stresses. The stress is a measure of force intensity and is defined as the force per unit area, which gives stress the same units as pressure, i.e., Pascal. Due to high values of stress, MPa is a more commonly used unit. Stress does not depend on the material nor the cause of the force.

The stress state is defined by the Cauchy stress tensor

$$\sigma = \begin{bmatrix} \sigma_{xx} & \sigma_{xy} & \sigma_{xz} \\ \sigma_{yx} & \sigma_{yy} & \sigma_{yz} \\ \sigma_{zx} & \sigma_{zy} & \sigma_{zz} \end{bmatrix}. \tag{3.4}$$

Stress can be defined at any point of a body and may vary in space and time.

As a point has no area, graphically, the components of stress are usually represented on an infinitesimal cube around said point, as can be seen in Figure 3.1.

The components normal to the surfaces are called normal stresses, while the ones parallel to the surfaces are denominated shear stresses, which cause normal and shear strains, respectively. For there to be equilibrium, it can be verified that the tensor needs to be symmetric, i.e., $\sigma_{zy} = \sigma_{yz}$.

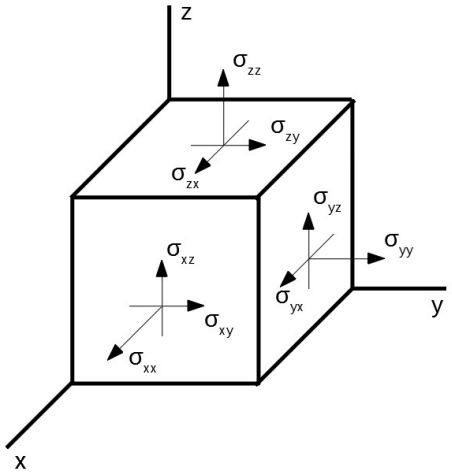

Figure 3.1: Stress components representation.

Von Mises Stress

When a body has a simple shape, like the typical specimens used in experimental tests with a circular or square cross-section, and there is only a unidirectional load, it is easy to compute the stress, compare it with the material yield stress and verify whether failure of the body occurs or not.

However, most systems tend to have more complex geometry and loading conditions, there are normal and shear stress in all directions and it becomes impossible to check for yielding with the stress in just one direction, as one would do in a tensile test. To solve this problem, von Mises [43] proposed a yield criterion, known as the von Mises Criterion.

The von Mises stress is defined as

$$\sigma_{\mathrm{VM}} = \sqrt{\sigma_{xx}^2 + \sigma_{yy}^2 + \sigma_{zz}^2 - \sigma_{xx}\sigma_{yy} - \sigma_{yy}\sigma_{zz} - \sigma_{zz}\sigma_{xx} + 3(\sigma_{xy}^2 + \sigma_{yz}^2 + \sigma_{zx}^2)}\,. \tag{3.5}$$

The usefulness of this criterion is that it reduces the 3D stress state at any point to a scalar. The von Misses stress distribution is a scalar function of space and time. It is considered that the material yields when the von Mises stress is larger than the material yield stress.

While the von Mises stress was proposed for isotropic and ductile metals, it can also be used in other materials to gain an idea of how it will behave, although it will induce some deviations.

3.1.4 Constitutive Equation

The relation between stress and strain is given by the constitutive equation, known as Hooke's Law

$$\sigma_{ij} = C_{ijkl}\varepsilon_{kl}\,, \tag{3.6}$$

where C is the elasticity tensor.

3.1.5 Equilibrium Equation

For a body to be in static equilibrium, the resultant of all applied forces has to be zero. These can be divided into surface forces, which are applied on the surface and can be described in terms of stresses; and body forces, f_j, that are applied on the body volume, such as gravity. This equilibrium can be described by the expression

$$\frac{\partial \sigma_{ij}}{\partial x_j} + f_j = 0. \tag{3.7}$$

Equations 3.2, 3.6 and 3.7 are important as these will be the equations that will be used by FEA programs in the third step of the FEM process mentioned in chapter 2, and that will originate the stiffness and mass matrices that will be discussed in the following section.

3.2 Equation of Motion

The easiest way to obtain and understand the equation that describes the motion of any dynamic system is to start by analysing the simplest example, the mass-spring-damper system, seen in Figure 3.2. This system is composed of one spring with stiffness k, one mass m and one damper with damping coefficient c. The mass can only move in one direction and so it has just one DoF, x, with x being a function of time, $x(t)$, but for simplicity of language, the (t) will be dropped. This system is called a Single DoF (SDoF) system.

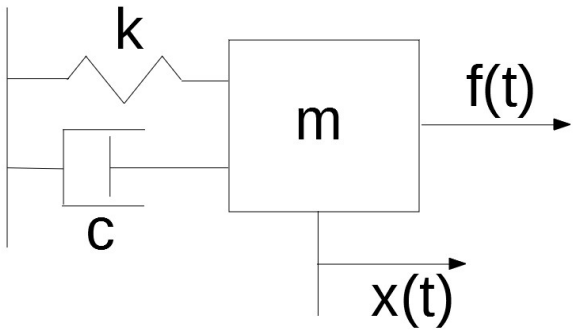

Figure 3.2: Mass-spring-damper system.

The mass, the spring and the damper have kinetic energy T, elastic potential energy U and dissipative function $\mathfrak{F}$, respectively,

$$T = \frac{1}{2} m \dot{x}^2, \tag{3.8}$$

$$U = \frac{1}{2} k x^2, \tag{3.9}$$

$$\mathfrak{F} = \frac{1}{2} c \dot{x}^2, \tag{3.10}$$

where $\dot{x}$ represents the derivative of x with respect to time, i.e., the velocity.

Applying the Lagrange equation

$$\frac{d}{dt}\left(\frac{\partial T}{\partial \dot{x}}\right) - \frac{\partial T}{\partial x} + \frac{\partial \mathfrak{F}}{\partial \dot{x}} + \frac{\partial U}{\partial x} = \frac{\partial(\delta W)}{\partial(\delta x)}\,, \tag{3.11}$$

where W is the work done by force $f(t)$, to equations 3.8, 3.9 and 3.10, the equation of motion of the system is obtained

$$m\ddot{x} + c\dot{x} + kx = f(t). \tag{3.12}$$

The general solution for this equation and its deduction can be seen in [44]. Equation 3.12 can be easily scaled for multiple DoFs (MDoF), retaining the same form

$$[M]\{\ddot{x}\} + [C]\{\dot{x}\} + [K]\{x\} = \{f(t)\}\,, \tag{3.13}$$

where $[M]$, $[C]$ and $[K]$ are the mass, damping and stiffness matrices, respectively; and $\{x\}$ and $\{f(t)\}$ are the generalized coordinates and force column vectors, respectively.

A more detailed derivation of and other methods to obtain equation 3.13 can be seen in [15, 45].

3.2.1 Static Analysis

In a static analysis, there is no variation in time. Therefore the terms related to velocity and acceleration are null and neither displacement nor the force vector can vary with time, and equation 3.13 is reduced to

$$[K]\{x\} = \{f\}. \tag{3.14}$$

Even though any application of force to a system will always have associated a transient period, it is assumed that the application is slow enough to not induce any vibration and that enough time has passed since its application for the response of the system to have stabilized and to not vary afterwards.

Solving this system yields the displacement of every DoF.

3.2.2 Modal Analysis

The natural frequencies of a system are the frequencies at which the system will naturally oscillate if subjected to a disturbance and no damping or external forces exist. Each natural frequency has a normal mode associated, that is, the system motion that happens when it vibrates at that frequency. The natural frequencies, damping coefficients and mode shapes are called modal parameters and are a function of the structural and material properties and the boundary conditions. The study and determination of the modal parameters is called modal analysis.

It is important to know the natural frequencies of a system because if an oscillating force is applied and it has the same frequency or is close to one of the system's natural frequencies, the system will

experience a phenomenon called resonance, where the response of the system will grow continuously, if no damping is present or if it is significantly low, until failure occurs.

To obtain the natural frequencies of the structure, the undamped free vibration of the system is analysed. The matrix $[C]$ is neglected, the force $\{f\}$ is considered zero and equation 3.13 is reduced to

$$[M]\{\ddot{x}\} + [K]\{x\} = \{0\}. \tag{3.15}$$

Assuming a solution of the form

$$x = X\sin(\omega t)\,, \tag{3.16}$$

where X is the amplitude and ω the angular frequency. All DoF move at the same frequency.

Introducing solution 3.16 into expression 3.15 yields

$$\left[[K] - \omega^2[M]\right]\{X\} = \{0\}\,, \tag{3.17}$$

which is a time independent expression.

This expression has a trivial solution, $\{X\} = \{0\}$, corresponding to no motion, but that is of no interest; for $\{X\}$ to be non-trivial, the matrix $\left[[K] - \omega^2[M]\right]$ has to be singular, that is,

$$\det\left[[K] - \omega^2[M]\right] = 0\,. \tag{3.18}$$

This equation yields the square of the natural frequencies of the system, ω_j^2, also called eigenfrequencies. The first natural frequency is also called fundamental frequency. There are as many natural frequencies as there are DoFs. By inputting a natural frequency in equation 3.17, the corresponding mode (or eigenmode), ϕ_j, is obtained.

The modes do not provide any value of the absolute displacement of the system during vibration, only the motion shape and the displacement of a node relative to the others. The actual displacement will depend on the amplitude of the excitation applied to the system. As long as the excitation force has the same mode frequency, the shape and relative motion will always be the same, no matter how small or big the amplitude (without taking into account possible fractures, plasticity and other material effects).

If one of the frequencies is zero or very close to zero (usually associated with round-off errors), it means that there is a rigid-body mode and usually implies that the structure is ill constrained, as in most cases, this is not intended.

As it is more common and intuitive to express frequency in Hz, this can be obtained by applying the know expression

$$f = \frac{\omega}{2\pi}. \tag{3.19}$$

The matrix formed by all eigenvectors is called Modal Matrix, $[\Phi] = [\{\phi_1\}\{\phi_2\}...\{\phi_N\}]$.

The modal mass and modal stiffness matrices are defined as

$$[M_q] = [\Phi]^T [M][\Phi] \tag{3.20}$$

and

$$[K_q] = [\Phi]^T [K][\Phi]\,. \tag{3.21}$$

It may be shown [15] that the modes shapes show orthogonality with respect to both the mass and the stiffness matrices

$$\begin{aligned} [\Phi_i]^T [M][\Phi_j] &= m_j \quad if\ i = j \\ [\Phi_i]^T [M][\Phi_j] &= 0 \quad if\ i \neq j \end{aligned} \tag{3.22}$$

$$\begin{aligned} [\Phi_i]^T [K][\Phi_j] &= k_j \quad if\ i = j \\ [\Phi_i]^T [K][\Phi_j] &= 0 \quad if\ i \neq j \end{aligned} \tag{3.23}$$

where m_j and k_j are the j^{th} generalized modal mass and modal stiffness, respectively.

From equations 3.22 and 3.23 the Rayleigh's equation may be obtained

$$\omega_j^2 = \frac{[\Phi_i]^T [K][\Phi_j]}{[\Phi_i]^T [M][\Phi_j]}\,. \tag{3.24}$$

This equation shows that when the system becomes overall stiffer, the natural frequencies will rise and that, on the other hand, will become lower if the system gains more mass.

Effective modal mass

Not all modes are equally important. Some modes are more easily excited, others may reach higher amplitudes with the same excitation input level, while certain modes might only be excited if the excitation force is applied in a certain direction. To better evaluate the importance of a specific mode in the overall response, instead of modal mass, the effective modal mass, m_{eff}, is used [46].

In the same way that each mode has an associated modal mass, it also has an associated effective modal mass. Usually, these values are not the same.

Whenever an excitation is applied to the structure, the modes with higher m_{eff} will be more easily excited and will have a bigger impact on the overall response. Those with lower m_{eff}, have less of an impact on the structure response, and in some cases may even be neglected in the response computation to save time and resources.

Since FE models tend to have thousands or even millions of DoFs, they will also have millions of modes. Computationally it is impractical to compute them all. However, it is not necessary to do this. The first modes tend to have a bigger effective mass and the response of the structure can be considered to be close enough to the real response if the computed modes have a total cumulative effective mass high enough. Usually, 80% to 90% of the total mass is the used threshold, although this number can

vary depending on the required accuracy.

Let $\overline{L}$ be a coefficient vector defined by

$$\overline{L} = [\Phi]^T M \overline{r}\,, \tag{3.25}$$

where $\overline{r}$ is a influence vector representing the displacements of the masses that result from static application of a unit ground displacement.

The effective modal mass for mode j is given by

$$m_{\text{eff}_j} = \frac{\overline{L}_j^2}{m_j}\,. \tag{3.26}$$

For each direction, there is an associated m_{eff}, in a total of six per mode, 3 in translation (axis X, Y and Z) and 3 in rotation (around axis X, Y, Z). This property is most useful to compare the importance of response in the same direction between modes. Comparing values of m_{eff} in different directions for the same mode can be misleading and induce mistakes.

The sum of all mode's m_{eff} is equal to the total system mass, m.

As having the m_{eff} in kilograms might not be the most intuitive way to grasp the influence of each mode, it is common to present the effective mass in a fraction

$$\hat{m}_{\text{eff}_j} = \frac{m_{\text{eff}_j}}{m} \tag{3.27}$$

known as effective modal mass fraction, $\hat{m}_{\text{eff}}$. The sum of all fractions is equal to 1, or 100 % if percentages are used instead.

3.3 Linear vs Nonlinear Analysis

When analysing structures it is common to admit that all displacements are small. This allows for the equilibrium equations to be considered only on the non-deformed structure, as the deformed structure is basically the same, and for the response to be linear, i.e., the response of the body is directly proportional to the excitation that is applied to it. If, on the other hand, the change in the structure is not neglectable, the analysis is no longer linear and it becomes necessary to perform various iterations, applying the equilibrium equations to a new shape as the structure deforms.

Another type of non-linearity is related to materials. Material behaviour has an initial elastic linear behaviour, represented by the Hooke Law. However, when the material reaches the yield stress, plastic deformation begins to happen and strain is no longer proportional to stress. The generic strain-stress curve for materials can be seen in Figure 3.3.

If a structure has small displacements, the plastic regime might be neglected for most typical materials.

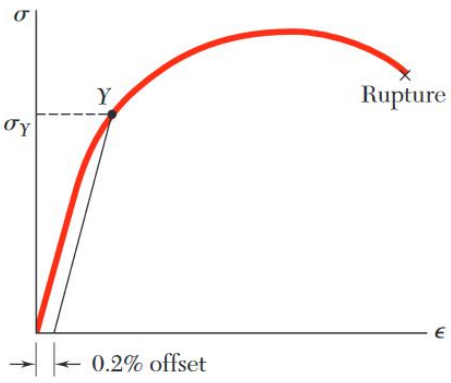

Figure 3.3: Material behaviour: strain-stress curve [47].

3.4 Bolted Joints

When a system has more than one component, it becomes necessary to join them and guarantee that the components remain joined throughout the life cycle. One of the most common types of joining methods is the bolted joint, where a fastener is threaded into a nut or into threads tapped on the components to be joined. An initial preload is applied so that the clamped parts remain in compression and in contact and that no gaps are formed, as these could lead to unwanted impact and stresses between the components.

For permanent joints, the preload, F_{PL}, is given by

$$F_{\mathrm{PL}} = 0.77 * \sigma_y * A_t \,, \tag{3.28}$$

where, σ_y is the yield strength of the joint's material and A_t is the tensile stress area and 0.77 is a recommended and empirically tested value for permanent joints [48].

According to standard [49], the tensile stress area A_t is given by

$$A_t = \frac{\pi}{4}(d_{\mathrm{nom}} - 0.9382P)^2, \tag{3.29}$$

where d_{nom} is the bolt nominal diameter and P is the thread pitch.

The screwing of bolts to the correct level of preload force is usually measured not by the force itself, but through the correspondent torque. The relation between torque, T, and the preload is given by

$$T = K_T * d_{\mathrm{nom}} * F_{\mathrm{PL}} \,, \tag{3.30}$$

where K_T is the torque coefficient. A typical value for this coefficient is 0.2 [48].

3.5 Response in Time and Frequency Domains

When using exciters, accelerometers or other sensors and transducers, the input and response are measured in the time domain. But in many cases, the time domain is not easily understandable and

it is not possible to quickly assess the meaning of the measured data. When converted from the time domain to the frequency domain, the results tend to become more intuitive, as can easily be seen from the example in Figures 3.4 and 3.5. While it is obvious in the frequency domain that this example function is a sum of six sinusoidal and what the frequency of each is, in the time domain that is not clear and might almost seem a random function.

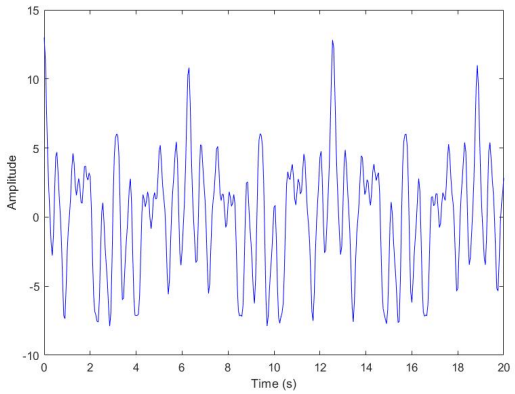

Figure 3.4: Example function in time domain.

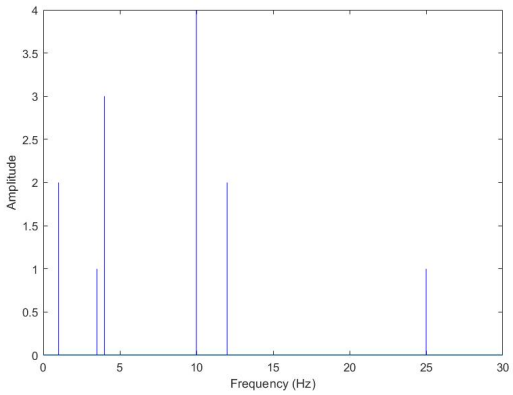

Figure 3.5: Example function in frequency domain.

The Fourier Transform (FT) allows the transformation of a function from the time to the frequency domain [50]. However, when measuring results, the data is not measured continuously, but at discrete points in time. So, in place of using the FT, which is applied to continuous functions, the Discrete Fourier Transform (DFT) is used instead.

The DFT is given by

$$X_n = \sum_{n=0}^{N-1} x_n \, e^{-\frac{i2\pi}{N} kn} \,, \tag{3.31}$$

where x_n is the n^{th} element of a finite discrete sequence of N samples that will be transformed into the n^{th} element of a same-sized sequence of samples, X, which is a complex-valued function of frequency.

Being a discrete and finite sequence of values, it can be easily implemented and done by computer algorithms, named Fast Fourier Transform (FFT). This allows for the quick computation of high amounts of data.

3.5.1 Frequency Response Function

After applying the FFT to the measured data, linear spectra of both the input excitation and output response are obtained. From these, the input, S_{XX}, and output power spectra, S_{YY}, can be computed, representing the power distribution of the input and output over the spectrum; and also the cross-spectrum, S_{XY}, that indicates the cross-correlation between signals.

From these, the Frequency Response Function (FRF), typically represented as H, is obtained

$$H = \frac{S_{XY}}{S_{XX}} \,. \tag{3.32}$$

The FRF is the function that describes the ratio between the input excitation force and output response motion of a system in the frequency domain. The general representation can be seen in Figure 3.6.

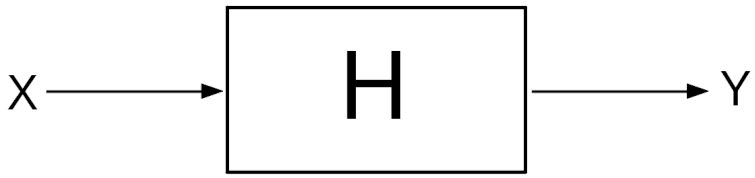

Figure 3.6: FRF schematic.

The FRF is a complex function and therefore it has both real and imaginary parts, with both varying as a function of frequency (see Figure 3.7). As a 3D graph is not easy to interpret, it is common to divide the response into two graphs, both as a function of frequency.

It is seen that when the real part is equal to zero, the corresponding frequency is a resonant frequency of the structure. For the imaginary part, peaks will be seen at these frequencies, either positive or negative.

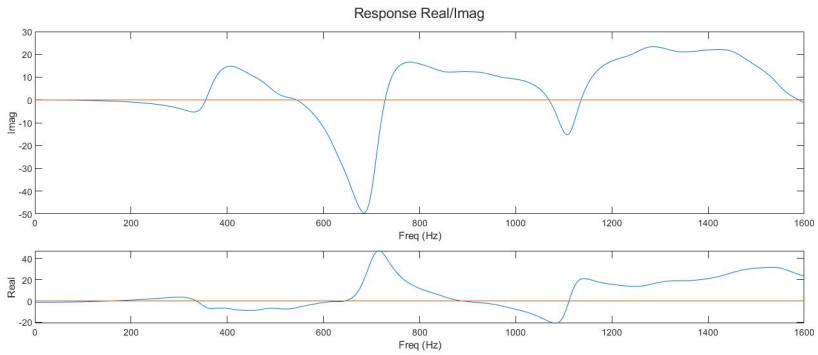

Figure 3.7: Example FRF obtained experimentally in real-imaginary form.

Usually, it is more convenient and more intuitive to present this function in terms of amplitude and phase (see Figure 3.8). This is known as the Bode diagram. In the amplitude plot, the peaks are found at the resonance frequencies, while in the phase diagram, at resonance the phase loses 180º, while at anti-resonances the phase gains 180º instead.

A FRF can be presented in multiple forms. When the output is given in acceleration units, the FRF corresponds to the ratio between acceleration and force and is called accelerance, with units $(\mathrm{m/s^2})/\mathrm{N}$. While accelerance is the most common presentation, the FRF can be presented with the input of velocity (mobility - (m/s)/N) or displacement (compliance - m/N), although the behaviour being represented is always the same.

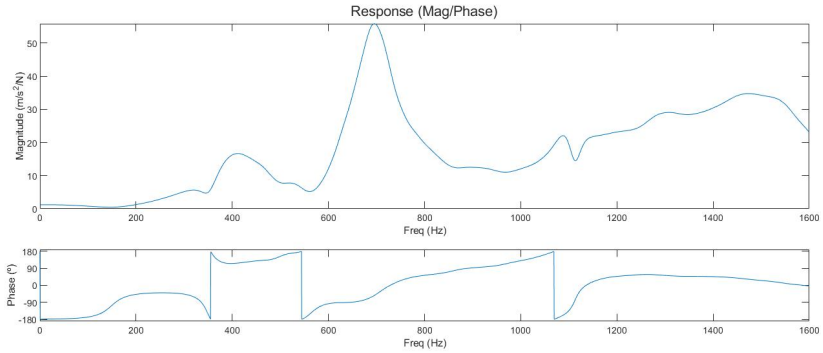

Figure 3.8: Example FRF obtained experimentally in amplitude-phase form.

3.5.2 H_1 Estimators

As no structure, data acquisition and excitation system is truly perfect, there are always differences between measurements and each time a different FRF is obtained, associated with random noise. Since it is not possible to know which measurement is the correct one, multiple measurements are performed and the results are averaged with the use of an estimator, so that random variations between measurements, related to noise and other sources, cancel each other.

One of the more commonly used estimators is the H_1 estimator. This estimator assumes that only the output has noise, while the input is completely accurate with no error associated. The system schematic can be seen in Figure 3.9.

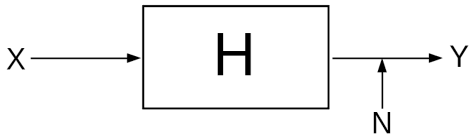

Figure 3.9: H_1 estimator - system schematic.

This can be written as

$$Y = H \times X + N\,, \tag{3.33}$$

where N is the noise.

This estimator tends to underestimate the FRF if the input does have noise, contrary to what was assumed.

Additionally, other estimators assume noise only on the input (H_2) and noise on both input and output (H_V), with further details present in [51].

3.5.3 Coherence Function

The coherence function is a function in frequency typically used to assess the quality of the measured data and is given by

$$\gamma_{xy}^2(f) = \frac{|S_{xy}(f)|^2}{S_{xx}(f) \cdot S_{yy}(f)} \,. \tag{3.34}$$

It correlates the input spectrum to the output spectrum and defines how much the second is due to the first, indicating how repeatable the measurement of the FRF is. As such, it is necessary to have at least two measurements for the coherence function to have any relevant meaning. Each time a measurement is done, the new power spectra are computed and are averaged with the previous spectra, and new values of coherence are obtained.

It can vary between 0 and 1, where 1 indicates that the FRF measurements are very repeatable, and 0 indicates the opposite. Should there be only one measurement, the coherence will be 1 for the entire frequency range, but it does not allow to conclude anything about that measurement.

Ideally, the coherence should be 1 or as close to 1 for the entire measured frequency range. At anti-resonance frequencies, the output data tends to be so low that the instruments' noise becomes of the same order of the output and inconsistency between measurements is expected, and values closer to zero are not problematic. On the other hand, for resonances, as the measured values tend to be high, the noise is various orders of magnitude lower and barely affects the signal, and a value of one is expected.

Therefore, values consistently closer to 0 than to 1 across the spectrum are a strong indicator that some error is being committed, e.g, the excitation is not strong enough to properly excite the structure.

In Figure 3.10, it is possible to see a typical coherence function.

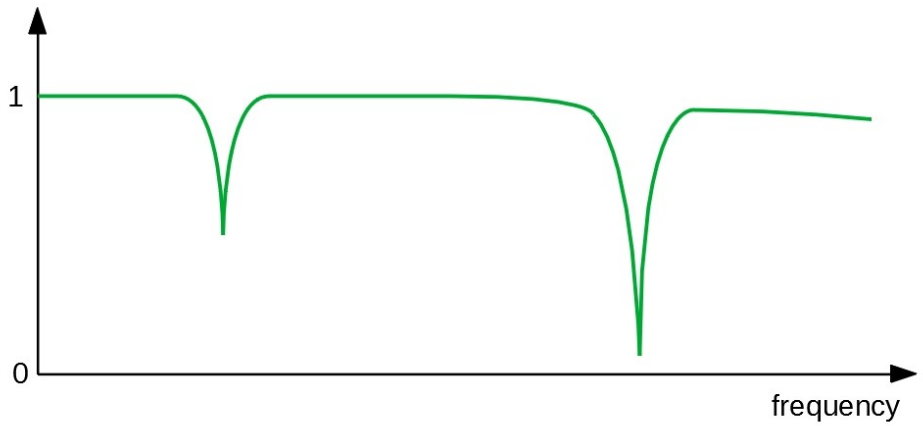

Figure 3.10: Example coherence function.

3.5.4 Leakage and Windows

When a signal is not periodic in time, which is required to have an accurate FT, leakage of the energy distribution across the spectrum occurs and the FRF is wrongly estimated. Especially for lightly damped structures, whose response will be significantly longer in time and typically goes beyond the measured time interval, resulting in a non periodic signal, leakage is a frequent issue.

To counter this, one can either increase the frequency resolution or the time interval and guarantee that a periodic function is measured. But if it is only possible to have a non periodic function, then a window may be used. A window function is a weighting function that is applied to the measured data and forces it to become a periodic signal. And while the window changes the measured signal, which can also impact results, it is usually preferable to having leakage.

Transient Window

The transient window, also known as Dirichlet or square window, is the simplest type of window function. It is a unity function, defined as

$$\text{Window} = \begin{cases} 1 & \text{if shift} < t < \text{shift} + T \\ 0 & \text{if} t < \text{shift or} t > \text{shift} + T \end{cases} \tag{3.35}$$

where shift is the period of time after which the data is acquired and T is the interval of time during which data is acquired. An example of the application of this window can be seen in Figure 3.11.

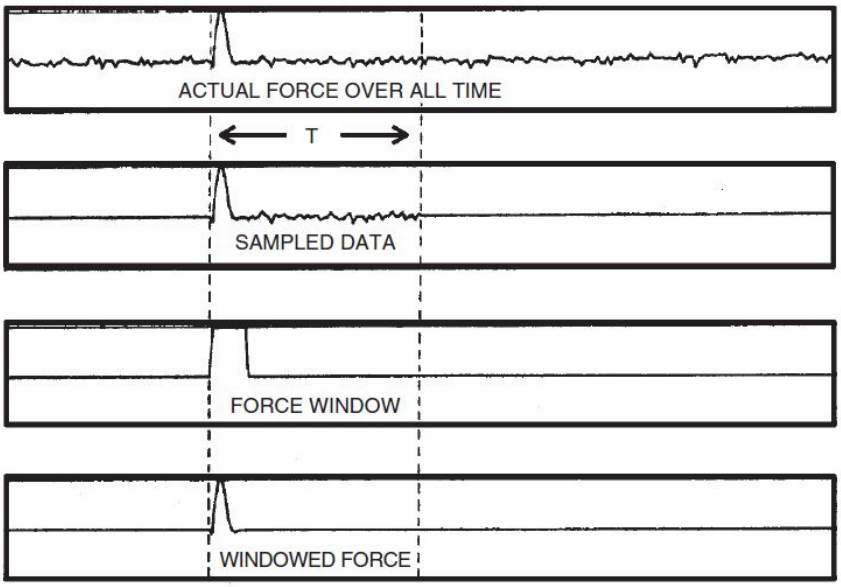

Figure 3.11: Impact force input in the time domain and use of square window [51].

This type of window is used for impact testing when all data can be fully acquired during time interval T. This is the case of the input, which is an excitation force pulse, and quickly goes to zero. Leading and trailing cosine tapers might be added to the window if necessary.

Exponential Window

The exponential window, also known as the Poisson window, is a typical window used for impact excitations on lightly damped systems, where the signal is the sum of damped sine waves. And while these signals decrease exponentially to zero, usually they do not decrease quickly enough in the measured time block, making these signals non periodic and thus forcing the use of this type of window. This

window is also common when burst random excitation is used.

It is defined by the time constant τ and a shift specifying the starting point. In Figure 3.12 the time response from an example impact excitation and the resulting signal from the use of an exponential window can be seen. One should be careful with the use of exponential windows, as these types of windows can mask the presence of close modes.

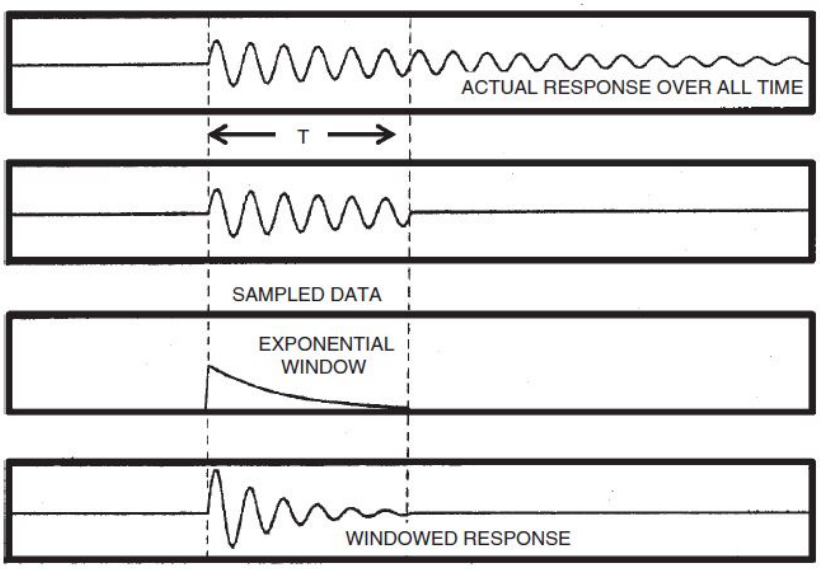

Figure 3.12: Impact excitation response in time domain and use of exponential window [51].

Additionally, other types of windows may be used, including Hanning, flat top, among others, which can be seen at [51].

3.6 Modal Testing

To be able to use the correlation criteria mentioned previously, it is necessary to conduct modal testing, so that the experimental mode frequencies, damping and shapes can be extracted.

3.6.1 Excitation Input

For the modes shapes to be extracted, the system under study needs to vibrate. This can be done by exciting it through artificial sources or by having the system undergo operation and run under operational conditions in-situ. This last method is called Operational Modal Analysis (OMA), but since for a satellite these experimental tests are meant to guarantee that the system can withstand the actual launch and operation, it is not possible to perform OMA and it will not be the object of analysis in the present work.

For the artificial sources of vibration, there are two types of excitation inputs.

Impact Hammer

The first is impact excitation. A (typically small) hammer (Figure 3.13) is used and the structure under study is hit with successive impacts. As the response in time is ideally of the impulse type, in the frequency domain it will be nearly constant in a broad range (see Figures 3.14 and 3.15). This interval range depends on the tip that is used, as the softness of the tip will determine how long or short the impact is, since an instant impact is experimentally impossible. Soft tips, like rubber, will produce excitation in lower frequency ranges, around the hundreds of Hz, while harder tips, like steel, might produce excitation up to many thousand Hz. The tip should always be chosen depending on the application and the intended frequency range. Applying a tip too soft or too hard might lead to noise at higher or lower frequencies, respectively.

Figure 3.13: Impact hammer.

To avoid damage and a localized non linear response of the system around the impact location, the system to be excited should be hit lightly. However, if the response is not high enough to be measured, a mass should be added to the hammer to increase the energy transferred by the hammer to the structure. While increasing the velocity would achieve the same result, when impacting by hand, it is impossible to have a precise velocity across impacts.

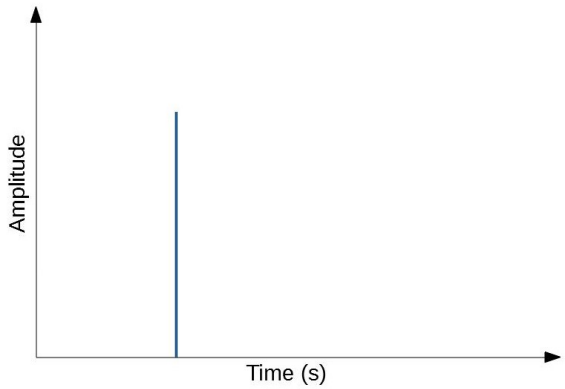

Figure 3.14: Hammer impact in the time domain.

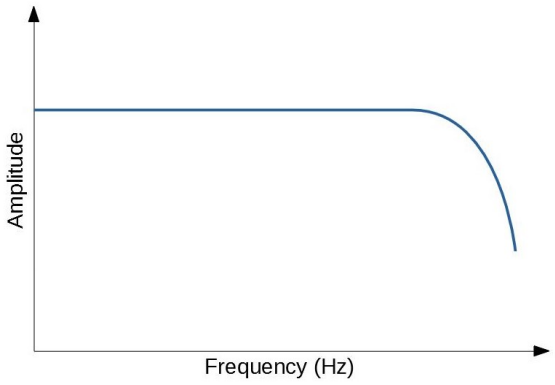

Figure 3.15: Hammer impact in the frequency domain.

This type of excitation is ideal for smaller and simple structures, as for bigger systems, the effect of the hammer will be very localized and the vibrations will damp out before reaching the opposite side of the system.

The biggest advantage of impact excitation is the simplicity of the excitation set up. It is only necessary to connect the hammer to the data acquisition system and decide where to excite the system. If one wishes to impact the system at various points, there are no extra set-up steps and is as simple as hitting the hammer at the new location.

On the other hand, as the hammer is controlled by hand it is not possible to use specific force levels, and it can become relatively easy to add human-based errors to the results, as a hand is less precise than a computer system. Care should always be taken for the same amount of force to be used, for the correct point to be hit and to avoid double impacts. This makes it harder for the measurement to be repeatable and depends greatly on the skill of the user. There is also a limitation related to the direction of the excitation, as it might only be possible to hit and apply force in a direction normal to the surface, especially for thin plates.

Shaker

The second type of exciter is a shaker (Figure 3.16). Typically used for larger systems, it can be applied to smaller systems as well. The set-up of the shaker is more difficult as it is necessary to connect it to the system to be tested and the positioning of the shaker has to be precise. If multiple excitation points are used, each time it will be necessary to do the same set-up for each point. These connections of the shaker to the system under test might add additional stiffness and constraints to the system, altering its behaviour and response, which is not desired.

Figure 3.16: Shaker at ESA ESEC facilites.

Nevertheless, this type of exciter allows for broader and easily controlled frequency ranges. Moreover, the possibility to define precise force levels and perform additional tests, like random vibration tests with the same set-up, is an advantage of this type of exciter. This also tends to result in better FRFs.

If the system is large enough, multiple shakers might have to be used, instead of just using higher force levels, as it could induce local non-linearities near the excitation point. However, this increases the cost and time of set-up even more, the biggest disadvantages of this excitation method.

3.6.2 Excitation Output and Sensor

Once the system is excited in some form, it vibrates and the response has to be measured. This can be done through accelerometers, which measure the acceleration at the point where they are installed. While the sensor measures the acceleration in function of time, after the measurement it can be converted to acceleration in function of frequency, with most current data acquisition systems performing this conversion automatically.

Care should be taken when installing and adding accelerometers to the system. As the accelerometer is physically connected to the system under test, it will vibrate with it and the accelerometer will measure the response of the system + accelerometer, and not just the system's response. If the accelerometer has a small percentage of the system total mass, the effect will tend to be negligible. On the other hand, if the system has low mass and multiple accelerometers are used, the response can start to be significantly affected.

The installation of an accelerometer can also add additional boundary conditions if, for example, no slack is given to the cable connecting the sensor to the data acquisition system, restricting the movement of the system under test. Additionally, as any accelerometer has physical limitations, e.g. has no infinite range, care should be taken to not overload the sensors, i.e, guarantee that the measured accelerations do not exceed the accelerometers' maximum.

If the system or component being measured has symmetry, centre points and centre lines will tend to be nodal points/lines and, therefore, have zero displacement on those modes. For this reason, accelerometers should not be placed directly on top of these points/lines, but slightly off-centre, to make sure that all modes are measured by each accelerometer. In Figure 3.17 one can see that if the accelerometer is placed on the centre position of a vibrating beam, many modes will not be captured, as that point does not move on most modes, but can be easily corrected by off-centring the sensor slightly.

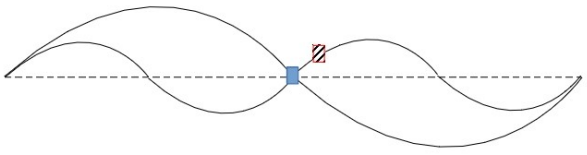

Figure 3.17: Accelerometer on vibrating beam: dash line - beam resting position; full lines - example of mode shapes.

There are other types of sensors, like strain gauges, that measure directly variables that could also be computed from the measured acceleration.

Besides attaching sensors directly to the system, one can also measure displacements and accelerations through imaging or laser systems, with the advantage of not restricting or affecting the system under test. Still, these measuring systems tend to be more complex, expensive, and only measure exterior surfaces.

3.6.3 Free-free Condition

The modal analysis can be done with some type of boundary conditions or in free-free conditions,i.e. with no boundary conditions, which are the easiest to obtain in an experimental setup . In this case, if it is a 3D problem, six rigid body modes will appear (three translational and three rotational). And while it is simple to simulate free-free conditions in a computer simulation, experimentally it is impossible to do a real free-free condition, as this corresponds to having the system floating with no type of support.

However, one can have a set-up that emulates free-free conditions as closely as possible. This is done by supporting the system using highly damped connections, like hydraulic systems (for bigger systems) or being suspended with elastic string. These damped connections allow for the maximum possible freedom of vibration with minimum effect.

3.6.4 Pre-test Planning

Besides providing numerical results, the FEA can also serve as an excellent tool to help set up an experimental test and ensure that it yields the best results possible. Current FEA programs have incorporated algorithms, that based on the FEA results, suggest the positions of the system where the excitations and sensors should be placed to obtain the necessary experimental data to successfully correlate the experimental with the computational data. Nevertheless, one has to have in mind, that should the FEA have errors, these pre-test procedures will have mistakes themselves. As such, care should always be taken and these suggestions should be taken just like that, suggestions.

Measurement Point Selection

When selecting points in the structure to measure, it has to be guaranteed that enough points are measured, so that the mode shapes are clearly identified. Otherwise, different mode shapes might look identical and some might even not be found. On the other hand, the more points one wishes to analyse, the more measurements are necessary, which take a longer time.

Therefore, the objective is to have the minimum measurement points that allow for a clear enough identification of the most relevant modes.

NX Siemens uses the Min-MAC algorithm to find the optimal positions from which one can obtain the maximum data from the minimum number of points. This is done by minimizing the off-diagonal terms of the MAC matrix. Since the mode set (with reduced points) will be compared to itself, the diagonal terms will be always one (see section 3.7) and are of no interest for this algorithm.

For the algorithm to start, the user has to select a minimum of two points, called required DoFs, that will serve as the initial base of comparison for the points selected afterwards by the algorithm. These required points will be sensor positions and, therefore, should correspond to DoFs that one has confidence that will be relevant in mode correlation.

Afterwards, the user has to select several candidate positions, that might be as many as there are DoFs in the FEM. The algorithm will add one candidate DoF at a time, computes the MAC with that additional DoF for all of them, and choose the DoF that minimizes the off-diagonal terms, before repeating

the same procedure. In each iteration, when computing the MAC, it will do so with the required DoFs and the DoFs that were chosen in previous iterations. The algorithm will keep choosing and adding DoFs to the sensor set until that set has the number of DoFs defined by the user. Usually, this number will correspond to the number of available sensors in the laboratory or take into account the time that will be spent in setting up each additional sensor.

While on the FE model it is possible to select any point and have a point-sized sensor in that position, in reality, the sensors have a certain dimension, many interior subsystems might be unreachable or too fragile to be adequate to attach a sensor to it. All of these add serious limitations to potential sensor locations, make it impossible to simply add all DoFs as candidate positions and require some engineering intuition by the user.

The full algorithm description and an example of its application can be seen at [31].

3.6.5 Modal Fitting

From the response of the system at various points, it is possible to extract the modal parameters. Currently, there exist multiple algorithms, that can be divided into various categories. Regarding the number of DoFs, these algorithms can be divided into SDoF and MDoF, with the latter category being of greater interest for the present work. Regarding the domain on which the algorithm is applied, they can be divided into time and frequency-domain algorithms.

The Least-Squares Rational Function (LSRF), which is the algorithm that was used in this work, is an MDoF, frequency domain estimation method. The goal of this algorithm is to estimate FRFs based on the measured FRFs by minimizing the cost function

$$J = \sum_{i=1}^{l} ||W(j\omega_i)(H_r(j\omega_i) - H_i)||_F^2 \,, \tag{3.36}$$

where H_i are the measured FRFs at frequency points $j\omega_i$, $i = 1, ..., l$, H_r are the estimated rational FRFs and W are optional weights.

The algorithm estimates different H_r, by using monomial basis, Sanathanan and Koerner iterations [52], and frequency-domain instrumental variable iterations [53]. The best solution which minimizes the cost function is chosen. A detailed explanation, analysis and example application of the LSRF algorithm can be seen in [54].

A comprehensive and detailed list of many other algorithms that are currently used can be seen in [44, 51, 55].

3.7 Correlation Metrics

To verify if two mode shapes obtained from modal analysis (analytical, computational or experimental) correspond to the same vector or to see how similar they are to each other, correlation metrics are used. Currently, the most used metric is the Modal Assurance Criterion (MAC).

A correlation analysis can be used to compare FEA-Test, validating a FEA with test results; FEA-FEA, studying the impact of altering variables and the optimization of sensor position; Test-Test, highlighting issues on the measurements in one of the tests, and so on.

3.7.1 Modal Assurance Criterion

The MAC gives a scalar value indicating the amount of consistency or correlation between two vectors and is defined as

$$\mathrm{MAC} = \frac{|\phi_i^H \phi_j|^2}{(\phi_i^H \phi_i)(\phi_j^H \phi_j)}\,, \tag{3.37}$$

where Φ_i and Φ_j are the two modal vectors being correlated.

The MAC can have any value between 0 and 1. When the MAC is 1 or close to 1, then both eigenvectors are consistent or have a high degree of consistency. When a vector is compared to itself, the MAC is exactly 1. When the MAC is close to 0, then the modes are not consistent. This is expected when the vectors being compared correspond to different modal modes.

The MAC is not an orthogonality check, as the modal vectors are orthogonal in respect to the mass and stiffness matrices, which are not used in the MAC expression.

When two sets of modes are compared a matrix of MAC values is obtained. It is typical for the MAC matrix to be represented either in a table, a 2D or a 3D graphic, with an example presented in Figure 3.18. Should the sets being compared not have the same number of modes, then the matrix will not be square. Many times only the modes that can be paired are compared and inputted into the MAC, and in this case, the expected is for the diagonal to have values closest to 1 as possible, and for the remaining matrix to be composed of near-0 entries. Should a set of modes be compared to itself, the resulting MAC matrix is symmetric (as MAC(*i*,*j*) is the same as MAC(*j*,*i*)).

Modes	1	2	3	4	5
1	1	0.1	0.03	0.06	0
2	0.1	0.98	0.03	0.2	0.1
3	0.03	0.03	0.9	0.14	0.01
4	0.06	0.2	0.14	1	0.08
5	0	.1	0.01	0.08	0.93

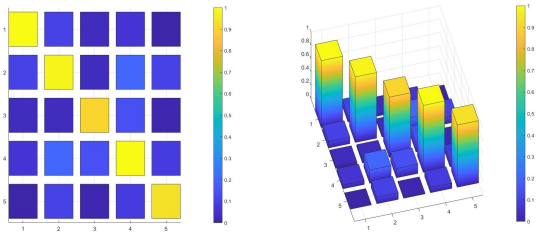

Figure 3.18: Example MAC representation (table, 2D graph and 3D graph).

For space applications and as suggested by the ECSS Standard [13], there is a good correlation between the computational model and the test model if for the fundamental mode the MAC is greater than 0.9 (and frequency difference lower than 3%); for modes with $m_{\mathrm{eff}} > 10\%$ the MAC is greater than 0.85 (and frequency difference lower than 5%); and MAC greater than 0.8 (and frequency difference lower than 10%) for the remaining modes in the relevant frequency range. Nevertheless, these values are only suggestions and in most cases, it will be the customer of a space system that will define which levels are required.

Chapter 4

Modelling and FE Analysis

This chapter focuses on the computational segment of this thesis. A more detailed description of the ISTSat-1 and each of its subsystems is presented, divided into four groups (section 4.1). Afterwards, the CAD (Computer Aided Design) modelling and idealization (section 4.2) and the FEM modelling (section 4.3), with the definition of the materials, contact regions, elements, convergence study, loads, boundary conditions and errors, are explained. Finally, the results of static and modal analyses are given (section 4.4).

4.1 System Description

As mentioned in chapter 1, the ISTSat-1 spacecraft is a 1U CubeSat composed of multiple subsystems. These can be divided into four major groups, the structure, the Printed Circuit Boards (PCB) stack, the solar panels (SPs) and other components. A more detailed description of each subsystem and connections between them will now be given. In Figure 4.1, an exploded view of the satellite is presented, where all subsystems are identified. The same cartesian positive coordinate system is always used for the system as a whole and is defined as follows: with the origin in the centre of the CubeSat, the +Z axis is normal to the V/UHF Antenna and the +X axis points to the side frame with the Remove Before Flight (RBF) pin gap.

4.1.1 Structure

The entire body structure, composed of four arm links and two side frames, is made of aluminium 7075-T6 and all parts were machined from a solid aluminium block.

The side frames contain the rails and rail stand-offs that are in contact with the deployer. Each side frame contains sixteen M3 holes to secure the SPs, eight of which also serve to attach the link arms to the side frames. Both side frames are located in planes normal to the X axis. On the +X side frame, there is also a small opening for the RBF pin. As can be seen in Figure 4.2, the side frames are mostly symmetric except for the mentioned RBF pin gap.

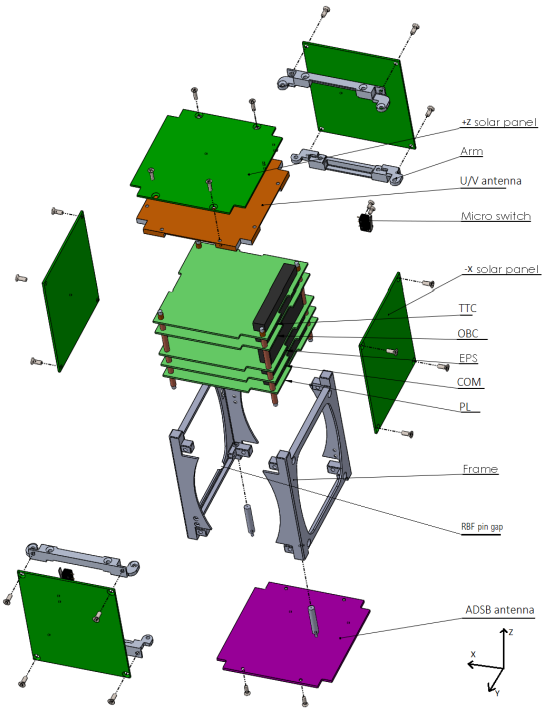

Figure 4.1: ISTSat-1 exploded view.

The arm links, besides connecting the side frames to one another and making the assemblage of all subsystems possible, also provide the connection for the remaining subsystems (axes, PCB stack and antennas) to the structure. Each arm link has six M3 holes, two for the SPs, two for the antennas and two for the axes. In Figure 4.3, the orientation and position ($\pm$ Y, $\pm$ Z) of the arm links can be seen.

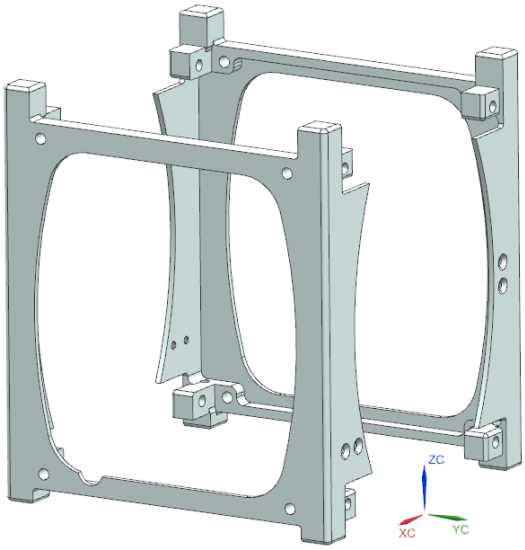

Figure 4.2: ISTSat-1 side frames.

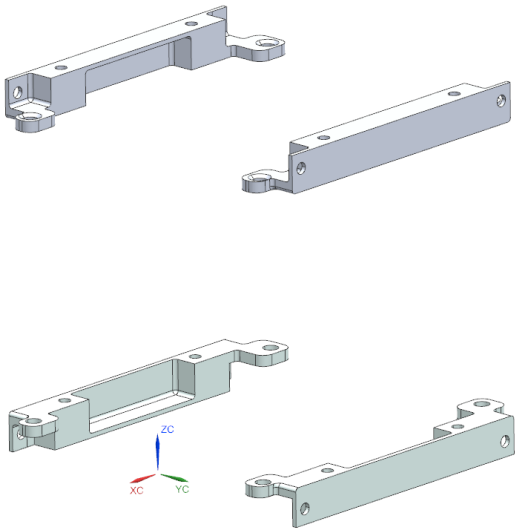

Figure 4.3: ISTSat-1 arm links.

4.1.2 PCB Stack

The four axes (Figure 4.4), made of stainless steel, are located on each corner of the PCBs and support the entire PCB stack. The spacers, that slide onto the axis and are located between each PCB, guarantee that the PCBs remain at a defined distance between each other.

On the PCB stack (Figure 4.5) there are a total of five PCBs, all with approximately the same size and shape (about 95 x 90 x 1.6 mm). These boards are made of composite FR4 and copper, with a M3 hole on each corner for the axis. A PC/104 connector on each PCB connects them all electrically. The components on each PCB depend on the PCB specific task.

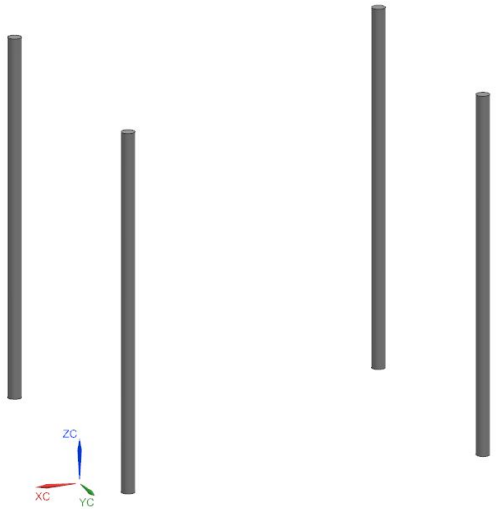

Figure 4.4: ISTSat-1 axes.

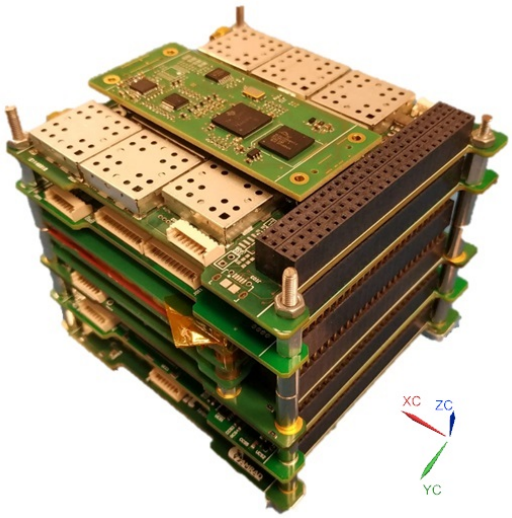

Figure 4.5: ISTSat-1 PCB stack.

Starting from the top PCB (+Z), the TTC (Telemetry, Tracking and Communications) is the subsystem responsible for maintaining the radio link with the ground station. It performs modulation and demodulation through a modem and has an additional independent beacon module that adds redundancy to the CubeSat tracking. The TTC board weighs 70 grams.

The OBC (OnBoard Computer) is the subsystem responsible for the housekeeping tasks of the whole CubeSat. It performs regular diagnostics of the other subsystems, besides detecting and reporting failures. It is capable of storing data and maintains the CubeSat time reference. The Attitude Determination and Control System (ADCS), incorporated on the OBC board, is the module responsible for ensuring that the S/C is not rotating and is pointing to nadir. It uses magnetometers, gyroscopes and sun sensors to determine the attitude and three perpendicular magnetic coils as main actuators to control it. The OBC board, including both subsystems, has a total mass of 45 grams.

The EPS (Energy Power System; Figure 4.6) is responsible for providing the power to the satellite, by harvesting energy through SPs, storing it in batteries and supplying it to the other subsystems as necessary. Attached to the EPS PCB is a battery pack, composed of four Lithium-Ion polymer cells that remain at a constant position and distance by the use of bolts and spacers. The EPS board and battery pack (including spacers and bolts) weigh 63 grams and 164 grams respectively.

The COM (Communication Processor and Data Storage) subsystem is the subsystem that implements the communications protocol and handles communication with the ground station when the satellite is operating in ”Normal Mode” and can take over all communication should the OBC go non-operational. The COM board weighs 48 grams.

Finally, the PL (Payload; Figure 4.7), at the bottom of the PCB stack ($-Z$), corresponds to the ADS-B receiver, necessary for completion for the CubeSat's mission. This subsystem is responsible for receiving the signals broadcast by commercial aircraft and translating them into messages. The PL board has a mass of 39 grams.

Figure 4.6: ISTSat-1 EPS and battery stack.

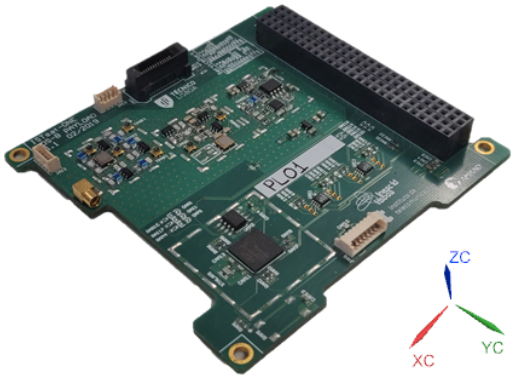

Figure 4.7: ISTSat-1 PL board.

4.1.3 Solar Panels and Antennas

On all faces of the satellite, with exception of the $-Z$ face, SPs are fastened to the structure. On the +Z face, beneath the SP a Very/Ultra High Frequency (V/UHF) antenna was mounted, while on the $-Z$ face is located the ADS-B antenna.

The SPs (Figure 4.8) are triple junction photovoltaic cells, with two cells connected in series in each panel. The board where the photovoltaic cells are attached corresponds to a normal PCB.

The ADS-B antenna (Figure 4.9) uses a single substrate layer and is based on classical probe-fed square patch configuration. The substrate is made of Rogers RT/duroid 6010, which is a ceramic-PTFE laminate composite.

The V/UHF antenna is a dipole antenna. During launch, to fit inside the P-POD, the antenna is retracted, only deploying in orbit thanks to a spring mechanism. This mechanism, the antenna and additional support electronic components are supported by an aluminium structure. There are M3 holes in the structure to attach it to the CubeSat structure and the SP on top.

Connecting all the components there are multiple bolts and nuts. The various component, including SPs, deployment switches, antennas are electrically connected to the PCBs through cables. Additionally, Kapton tape is used to attach the cables to the SPs and reduce their movement inside the CubeSat.

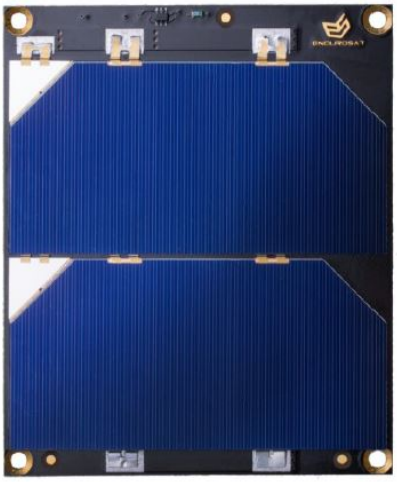

Figure 4.8: ISTSat-1 solar panel.

Figure 4.9: ISTSat-1 ADS-B antenna.

4.2 CAD Modelling

The initial CAD model of the ISTSat-1 was performed in *SOLIDWORKS*, where all subsystems were modelled in full detail. The structure included all fillets, as manufactured, the solar panels included the photovoltaic cells and the connecting ports, the PCBs and the antennas had all electronic components modelled. This model will be referred to as the 'initial model'. The initial model was then ported to SIEMENS NX (version 1851), where a process of idealization was conducted.

4.2.1 Idealization

As the initial model is quite complex, it is not convenient to use it for the FEM with all of its details, considering the extra and unnecessary cost that it might entail. As such, a process of simplification, reduction or even complete elimination of certain parts or CAD features that are not significant or necessary for the analysis is conducted. The model that results from this process will be henceforth be referred to as the 'idealized model'. This model is still a geometric model, as it has no elements or boundary conditions applied to it.

This process of idealization is a process of compromises and equilibrium between having a model that represents faithfully the CubeSat and the computational and time constraints imposed by the level of detail. As seen in the following sections, this reasoning also applies to other parts of FEA, such as the size of elements, the materials, among others. Sometimes, depending on the results of the simulations and the validation procedures, it can become apparent that some idealizations are not acceptable and need to be corrected.

Structure idealization

Both the side frame and the link arms have fillets. Fillets correspond to the rounding of a corner, either interior or exterior, in a part design. Physically, as corners tend to be stress concentrators, that is, they are points where the stress tends to be considerably higher due to the corner itself, fillets are added to smooth the corner and better distribute the stress across the volume near to the corner. The addition of a fillet can also have computational gains, as the abrupt change of direction might lead to the values of stress going to infinity, no matter how much one refines the mesh, with these points being known as singularities. The fillet can make the values tend to a finite value, effectively eliminating the singularity.

However, the fillet makes the geometry more complex, when compared to a perfectly squared corner, and the smaller the radius of the fillet is, the smaller the finite elements need to be to accurately represent the curvature. Considering the overall CubeSat structure and specific loads applied to it, it was verified that most corners were not stress concentrators and so almost all fillets were removed without impact on the final results. Only some fillets in the arm links were left due to their bigger relative size and therefore their increased relevance in the results.

All bolt holes were left in the idealized model, even those corresponding to components that were completely removed, as seen in a posterior section. Still, the chamfers that were modelled to allow space for the bolt heads were removed for the same reason applied to the fillets.

In Figures 4.10 and 4.11 the idealized parts can be seen. When comparing with Figures 4.2 and 4.3 (initial model), it is possible to notice that the idealized models have sharper edges and seem less smooth overall.

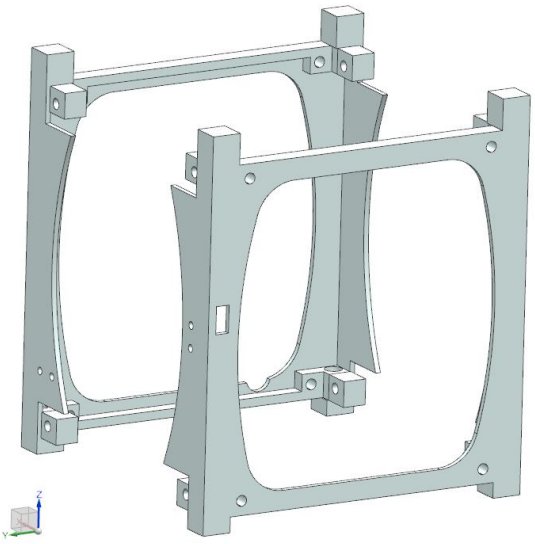

Figure 4.10: ISTSat-1 idealized side frames.

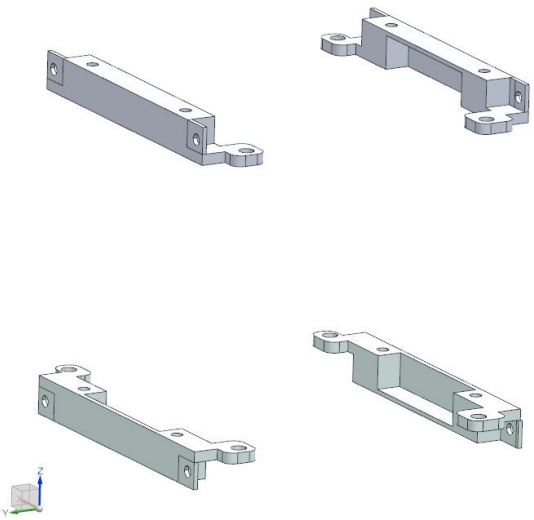

Figure 4.11: ISTSat-1 idealized arm links.

PCB Stack and Solar Panels Idealization

The PCB subsystems, besides the board itself, have integrated multiple electronic components from RAMs to capacitors and transistors. On the one hand, these components have small dimensions (smaller than a millimetre in some cases) which makes them impossible to represent with FE without having elements so small, that it takes unacceptable computational resources to solve the simulation. On the other hand, for the pretended analysis, that is, for the overall system response, the most relevant factor is the overall mass and stiffness of the PCB system. Therefore, it is not necessary to model each PCB component but just the board itself, without forgetting to include the components' mass into the board's mass.

There are just a couple of exceptions to this simplification:

- the PC/104 connectors have a dimension that is more significant when compared with the board dimensions. Besides, as the PC/104 connect one board to the other, they affect the stiffness of the PCB Stack and each board response by adding an additional constraint besides the 4 axes. However, they were considered to be uniform, and neither the pins nor the holes were modelled;

- The Battery Pack is the other component that cannot be disregarded, both dimension wise and with respect to the mass. On the system PCB + battery, the battery has 72% of the mass. But the battery cells themselves can still be idealized and approximated by parallelepipeds with the outer dimensions of the battery cells, without the need to reproduce all internal details. So, the system EPS+Battery is reduced to the EPS PCB, the cells, the PCB boards between the cells and the spacers.

In the PCBs, only the holes through which the axes pass were left in the idealized model. The remaining holes were removed due to their small dimension, which could lead to distorted elements near that area and due to their small influence on the overall response.

The SPs, and especially the photovoltaic cells, are quite fragile components, where an accidental light hit can damage the cells and render the solar panels useless. For this reason, during tests, the SPs were replaced by same sized PCBs without cells. Therefore, the photovoltaic cells were also removed in the idealized model to better represent the test model. This shows that the assumed approximations are not only based on computational grounds, but also on testing limitations.

Both the PCBs and the SPs are characterized by the difference in order of magnitude between the height and the remaining two dimensions. With the PCBs being just two millimetres high, the height is about forty five times smaller than both width and length. As such these components can be considered bidimensional, that is, the results are considered to be constant throughout the height, with relevant changes only occurring along the width and length.

This idealization has the advantage of simplifying part of the model from 3D to 2D and consequently reducing the required computational resources. Besides, if one were to work with the board 3D model, as it is very thin, the elements could end up quite elongated and distorted, the opposite of what is desired with a mesh, resulting in higher result values with a purely computational and not physical origin.

In Figures 4.12 and 4.13 the idealized TTC and EPS PCBs can be seen. The remaining PCBs are similar to the TTC PCB.

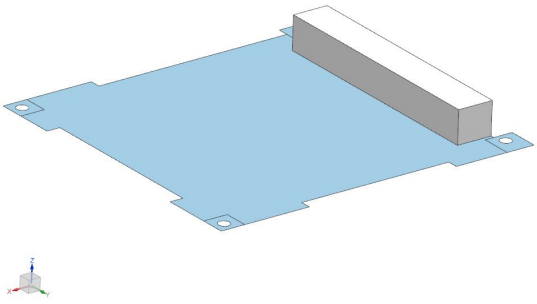

Figure 4.12: ISTSat-1 idealized TTC PCB.

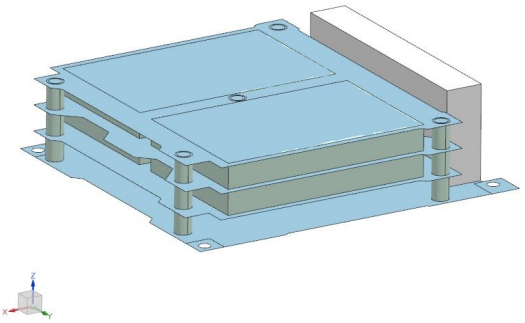

Figure 4.13: ISTSat-1 idealized EPS PCB.

The same reasoning applies to the ADS-B antenna, on the $-Z$ face, which was also approximated by a 2D plane. In the VHF/UHF antenna, only the structure was considered. All sub components were removed, including the antenna itself, as it has no impact on the structure stiffness.

Other components idealization

The following components were deleted from the initial model and were not a part of the idealized model:

- miscellaneous components, necessary for the CubeSat to function, but with an insignificant mass and small to non-existent structural significance. Besides, as rather small components, they would require a very fine mesh to accurately describe their geometry, increasing the computational cost;
- the bolts and the nuts, as the FEA program has specific features for simulating bolt connections, without the need of the bolt geometry CAD;
- all cables, since the cables' movements during launch are random and complex to model and there would be no plausible way to verify during tests if the FEM model was accurately representing the cables' behaviour. But one has to be aware that the cables can have a significant impact during launch if they were to repeatedly hit some solar panel or some PCB component, although this effect can be reduced by the use of Kapton and securely attaching the cables, allowing for this simplification of the model.

The idealized model can be seen in Figure 4.14.

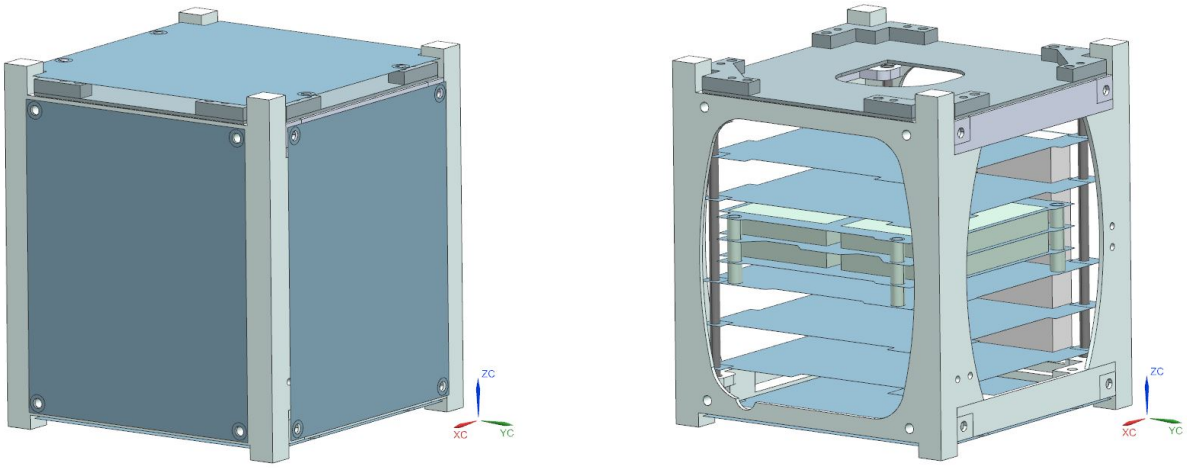

(a) With solar panels

(b) Without solar panels

Figure 4.14: Idealized model.

4.3 FEM Modelling

Once the idealization process is complete, the next step involves the creation of the FEM model. The CAD (idealized) model is fixed (without taking aside the possibility to correct any of the idealizations if necessary in function of the obtained results) and the FE process truly begins. Before any computation can be performed, it is necessary to create the mesh, assign materials and define boundary conditions. This was also performed on SIEMENS NX, as for the idealization process.

4.3.1 Materials

The materials that are used in the physical CubeSat have imperfections and a complex internal structure (especially for composite materials) that is next to impossible to model in all detail, requiring, as done before, additional simplifications. In this work the materials were considered to be only linear and that all deformations occurred in the elastic regime. During the analysis, it will be then verified that no component reached its respective material yield stress.

The side frames, the link arms, the V/UHF antenna structure and the battery spacers are made of Aluminium 7075-T6, which is an isotropic material.

All modelled bolts and axes are made of stainless steel.

The PCBs are considered to be uniform across their entire area and are made of FR4 composite, which is a glass fibre reinforced polymer. This is a common material for PCBs, due to it being flame resistant and having good strength to weight ratio [56]. This material is orthotropic. The same mechanical properties are considered equal for all PCBs. However, since the total mass of each system is different, different densities were assigned to each PCB, so that each PCB has the total weight of the respective subsystem, including all electronic components.

The PC/104 connectors are made of Polyphenylene sulfide (PPS), while the contact parts have metals, such as bronze, nickel or gold. However, since the pins were not modelled, only PPS material will be considered.

A battery is a complex component with various materials, but as structurally the most relevant material is the casing material, and since the geometry of the battery cells was idealized to a group of parallelepipeds, the batteries were considered to be made only of polyethylene (PE) [57], which is an isotropic material. The density considered was not that of PE, but the one necessary to give the actual battery mass.

For the SPs it was considered that these components were also uniform, and since the panel board is a normal PCB it had the same properties as the PCBs on the PCB stack, with density being that of usual FR4, contrary to others where the density was corrected for each board. As the photovoltaic cells were removed during idealization there is no need for the cells material properties.

The ADS-B antenna is considered to be uniform across the area and is made of Rogers RT/duroid 6010. However, since during the tests the patch antenna was substituted by a PCB similar to that of a solar panel, the material assigned to the antenna was the same as for the SP.

All materials' mechanical properties can be seen in Table 4.1.

Table 4.1: ISTSat-1 materials' mechanical properties.

	ρ ($\mathrm{kg/m^3}$)	E (GPa)	ν	G (GPa)	σ_y (MPa)
Aluminium 7075-T6	2810	72	0.33	26.9	503
FR4	6093 (TTC) 3913 (OBC) 5401 (EPS) 4174 (COM) 3431 (PL) 1840 (Solar Panel) 1883 (Battery)	24 (x) 21 (y) 21 (z)	0.12 (xy) 0.12 (xz) 0.13 (yz)	10.71 (xy) 10.71 (xz) 9.29 (yz)	276
PPS	1550	11.5	0.3	4.4	70
PE	1883.69	1	0.4	0.36	28
Stainless Steel	7872	200	0.25	76.92	490

Electric and thermal properties were not necessary for the analysis presented in this work.

With all materials assigned, it was verified that the total FE model mass was 861 grams, which compared with the measured mass, 872 grams, represents a difference of just 1.3%. This was to be expected considering some components were not included in the idealized model.

4.3.2 Elements

As previously mentioned, the basis of the FEM is the division of the model into smaller segments called elements, with a group of elements being called a mesh. However, this division can be done in different ways, with FEA programs nowadays providing dozens of different types of elements. The wrong or less adequate choice of element type can lead to errors in the obtained results. As such, it is important to understand the applications and limitations of each type of element. All data regarding

elements was taken from [58].

For the solid bodies (e.g., the side frames) CTETRA and CHEXA elements were used, the first one for more irregular and complex parts and the second for parts allowing a swept and more uniform mesh.

The CHEXA is a six-sided solid element that is the most commonly used element for solid bodies and should be employed where one wishes accurate stress results since it has a more regular shape. The CHEXA8 has eight corner points and its accuracy degrades as the element becomes more skewed and distorted, calling for the use of other more versatile elements.

The CTETRA is an isoparametric tetrahedron element. In complex components, especially with round-shaped parts, CTETRA meshes are much better shaped than CHEXA resulting in more accurate results. THE CTETRA4 element, with just four corner nodes, is overly stiff for all structural simulations and the CTETRA10, which has 6 additional nodes on the edges, should be used instead. Obviously, the higher number of nodes will require more computational power.

In Figure 4.15 it is possible to see the comparison of the Von-Misses stress results by changing the elements from CTETRA to CHEXA near a bolt hole connecting a solar panel to the side frame for the same type of analysis with the same load. The only difference between both simulations was the mesh around that hole. With the CTETRA mesh, an interior element was so skewed that its stress result was 300 MPa, ten times higher than adjacent elements. This abrupt variation in value (visible with the yellow and orange elements) between elements reveal that the stress problem was on the choice of element and mesh and not on the component design. This could be corrected with a more uniform mesh, either by refining it or changing the type of element. Once a more uniform mesh was obtained, the maximum stress value became around 3MPa, one hundred times lower than the value obtained with the CTETRA elements.

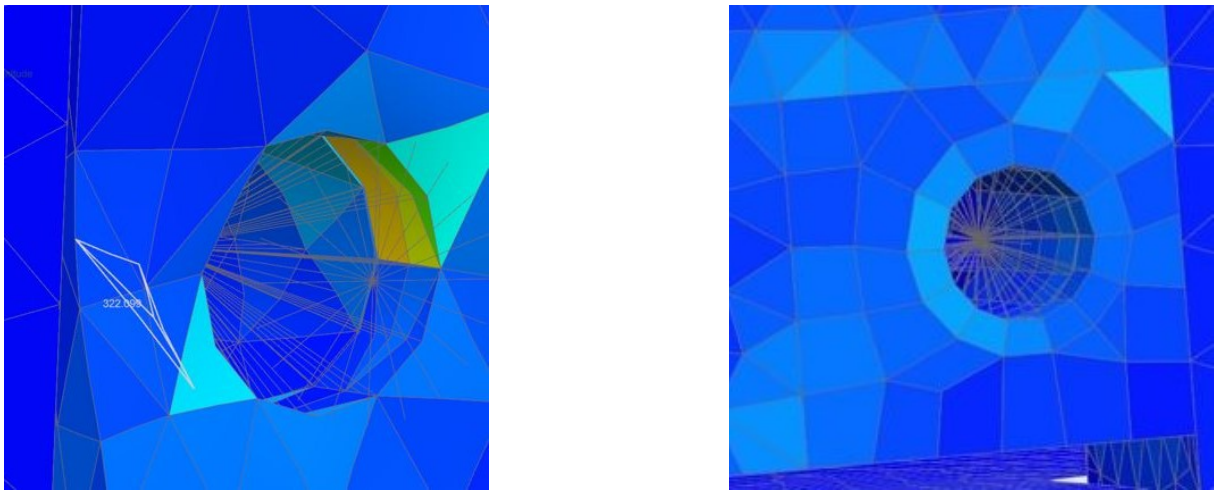

(a) CTETRA elements near hole

(b) CHEXA elements near hole

Figure 4.15: Comparison of CHEXA and CTETRA elements on a hole (with identical conditions).

Similar analyses were made throughout the model to verify which type of elements were most adequate for each part.

Since the PCBs and other components are considered bi-dimensional (see section 4.2.1) 2D elements were used. For linear analysis, the use of this type of elements assumes that, besides the

thickness being much smaller than the remaining dimensions, the deflection of the surface is small compared with its thickness and the normal to the surface remains normal during the bending.

For cases where the applied loads are bending or membrane forces, plate or shell elements should be used. For this work, CTRIA3 and CQUAD4 elements were used.

The CQUAD4 is the most common element for plates, corresponding to a plane connecting four nodes. It is most appropriate when the geometry is mostly plane, which is the case for the PCBs and solar panels. It should be verified that the elements are the most square possible, as the more distorted they are, the less accurate the final results.

The CTRIA3 is the triangular version, corresponding to a plane connecting three nodes. It is usually used in transition between meshes, irregular boundaries and round geometries, where the CQUAD4 becomes too skewed. However, this element can show excessive rigidity and should only be used when truly necessary, as it will show less precision than its quadrilateral counterpart for the same element size in most geometries. As the PCBs and solar panels have slightly irregular shapes and also present holes, these elements were necessary for transition between other elements.

Bolts

3D elements were not used to model the CAD model of the bolts, as it would not be practical, considering the size of the element that would be necessary to represent the component accurately with 3D elements. Besides, considering the type of load that the bolts are subjected to and their behaviour, these can be represented with enough precision by a linear 1D element along the bolt of the length, called the shank, and connected to the components where the bolt is screwed by other 1D elements, denominated as spider connection.

For the shank, CBAR elements were used. The CBAR formulation is derived from classical beam theory and this type of element supports tension, compression, torsion, bending and shear in two perpendicular planes. Each element has two nodes, one corresponding to the bolt's head and another for the thread.

The spider was made of RBE2 elements. R-type elements impose fixed constraints between the nodes to which they are connected. This means that the nodes of the components in which the bolt is screwed become dependent on the node the CBAR. Using RB2 elements adds stiffness to the simulated structure.

The characteristics of these elements were based on the characteristics of the bolt. E.g., the size of the CBAR was the same as the length of the bolt. The bolt connection between the solar panel and side frame can be seen in Figure 4.16.

Other elements

For the connection between the axes and the link arms, RBE2 elements were also used, as the axes are screwed into barrel nuts that fit into the link arms holes.

To simulate the connection between each PCB connector and between the batteries and the PCBs in

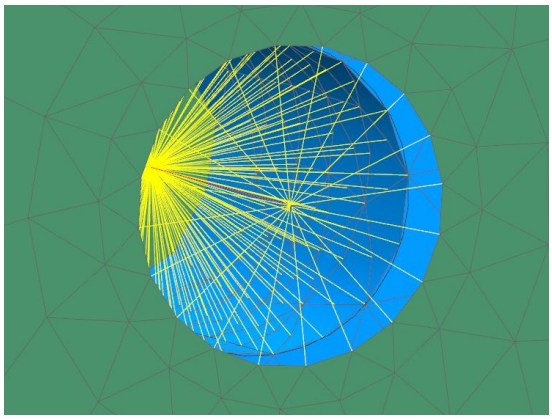

Figure 4.16: Bolt connection between the solar panel and side frame (green - solar panel, blue - side frame, red - shank, yellow - spider connection).

the Battery Stack, RBE3 elements were used. RBE3 belong to the same family of the RBE2 elements, but unlike these, RBE3 elements do not add additional stiffness. It was also guaranteed that the nodes of each body were coincident with each other to obtain more accurate results.

A concentrated mass point, which is a 0D element, was added to the model and connected by RBE2 elements to the $-$Z faces of the side frames stand-offs and to the CubeSat's side frames edges, as shown in Figure 4.17. The reason for the use of these elements in some of the simulations is further detailed in section 4.3.4 while explaining the model boundary conditions.

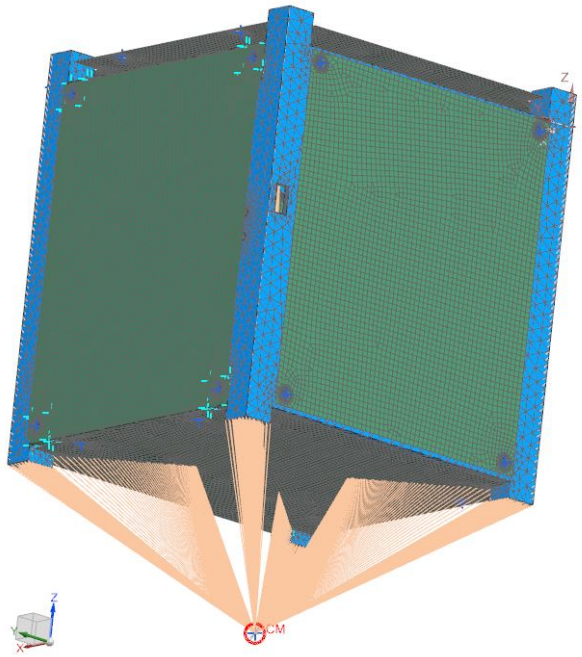

Figure 4.17: Concentrated mass element and rigid connections to CubeSat structure (Green - solar panels, blue - side frames, red - concentrated mass, salmon pink - RBE2 elements).

Finally, additional concentrated mass points were added, emulating the accelerometers masses (2.4 and 4.8 grams) when performing the simulations used for comparison with experimental results, as the attached accelerometer can lead to mode changes, as was explained in chapter 3. The positions

of these elements corresponded to the accelerometers' positions, according to the tests detailed in chapter 5.

4.3.3 Mesh and Convergence Study

Besides choosing the type of element, it is also fundamental to choose the size of each element. In fact, both these choices are related, as changes to one has impact on the other, e.g., an element with more nodes will have to be bigger if the computation time is to remain the same.

When one is dividing the model into elements, there will always be a discretization error associated. After all, a problem that physically happens in a continuum is transformed into a problem happening in a finite number of points. The more elements there are the closer to a continuum the FE model becomes and the smaller the error to the theory model value would be (without taking into account other sources of errors). If one had an infinite number of FE, one would be able to represent the exact behaviour of the structure. However, this would take an infinite amount of time to solve. But it is only necessary to have a number of FE high enough for the value to be as close as intended and for the error to be acceptable. So, a mesh with a reasonable initial size is created and afterwards, it is refined in several iterations, with the values across the system tending to the refined values until it is seen that these do not change significantly between iterations (for example, a difference smaller than 2% between two consecutive iterations), that what is obtained is accurate enough and that increasing the number of FE will bring no further advantage and gain. This process is called convergence study.

Since it is impractical to verify if convergence occurs in every single node of the entire model, alternatively it is usual to only focus on a more restricted set of points that

- are known to be stress concentrators, such as corners;
- belong to a part of special interest to the analysis, such as connections between components, or important components (in this case, the PCBs).

When applicable, this convergence study was made considering all three major directions, with each critical area being individually considered.

When a singularity point is being analysed, whenever the mesh is refined the computed value becomes higher and it never converges, always increasing its value until infinity. These points should always be held into account whenever one performs a convergence study since it may lead to a mesh that is too refined and consumes too much time, without ever reaching convergence at that point and leading to values that are significantly higher than the values on the real component. In these cases, one studies convergence in a point close to the singularity and the singularity's value itself is ignored.

The convergence study for the elements around the hole of the link arms connecting this component to the SP is now presented. It was done by performing a static analysis with the loads mentioned in section 4.3.4. For being bolted joints and due to the preload applied to these joints, it was noticed that these were some of the areas where greater stresses occurred. A stress example was presented since it usually requires a bigger refinement than displacements to converge, and if the stress distribution has converged one can have confidence that so has the displacement distribution.

An initial element size of 3 mm (corresponding to 8 elements in the surrounding area) was taken. This value was consecutively refined until a size of 0.5 mm per element (corresponding to 180 elements in the surrounding area) was reached.

The final mesh can be seen in Figure 4.18, while in Table 4.2 and Figure 4.19, the iterations values are presented.

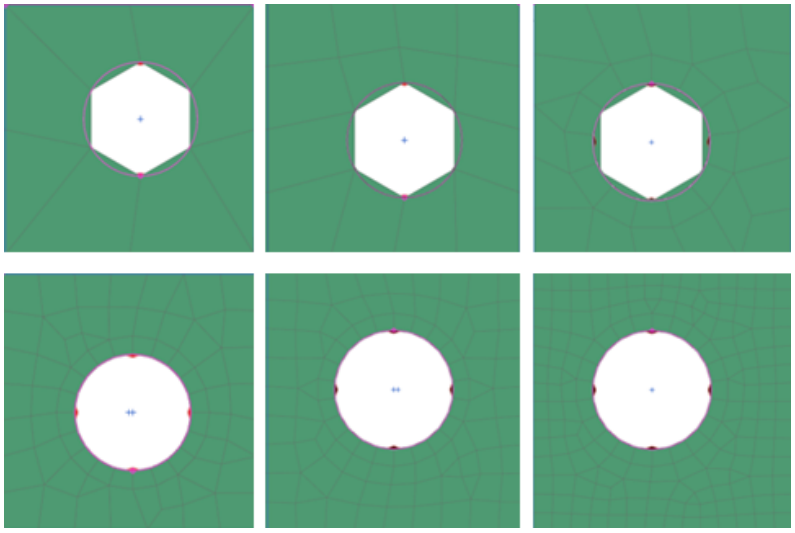

Figure 4.18: Mesh evolution around bolt hole (from left to right, top to bottom: 3, 2, 1.5, 1, 0.75 and 0.5 mm).

Table 4.2: Convergence of stress near bolt hole - absolute values (MPa) and relative variations (%).

Element size (mm)	Stress (MPa)	Difference to previous iteration (%)	Difference to 0.05 mm value (%)
3	15.50		89.5
2	12.43	19.8	52.0
1.5	9.02	27.4	10.2
1	8.52	5.5	4.1
0.75	8.34	2.1	1.9
0.5	8.18	1.9	

As the mesh was refined, the value of the Von-Misses Stress reduced until a final value of 8.18 MPa was reached. While in the first iterations there were differences of 20% between steps, for the last two iterations the difference between stress values was smaller than 2%, and it can be considered that the value had converged. However, since the difference between the 1 mm mesh value and the final value is relatively low (around 4%), it can be considered that in this 1 mm mesh the stress is close enough to the converged value, and so, this was the mesh size (1 mm) that was used in the proximity of the bolt holes in the SPs, saving some computational time.

The same procedure was followed for other points, such as the connections between the EPS PCB and the axis, the middle of the TTC, among others, but also for the frequency of the first modes, and despite not being presented here due to the repetitive nature of the process, satisfactory convergence

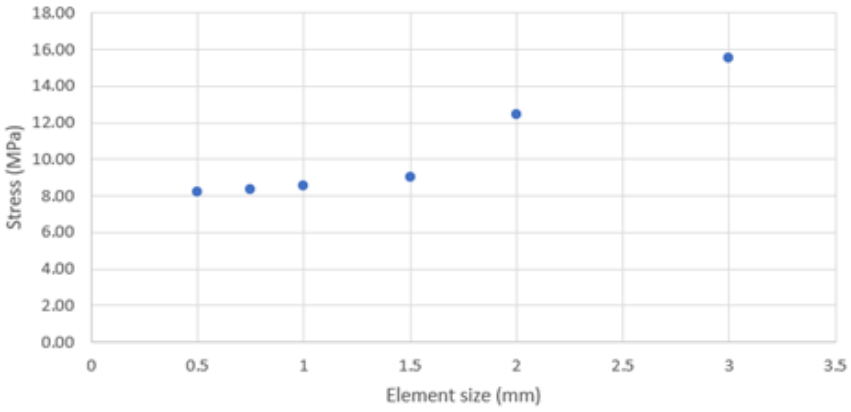

Figure 4.19: Convergence of stress near bolt hole: Stress (MPa) vs Element size (mm).

was verified in all of them.

For the 0D and 1D elements (RBE2 and RB3 connectors), no convergence study is conducted as these elements have a size depending on geometric factors and is not possible to refine them, with their values depending more on the type and convergence of the elements to which they are connected.

All results presented in the following sections were obtained with the refined mesh derived from the convergence process, with a total of 353451 elements and 500749 nodes, which can be seen in Figure 4.20.

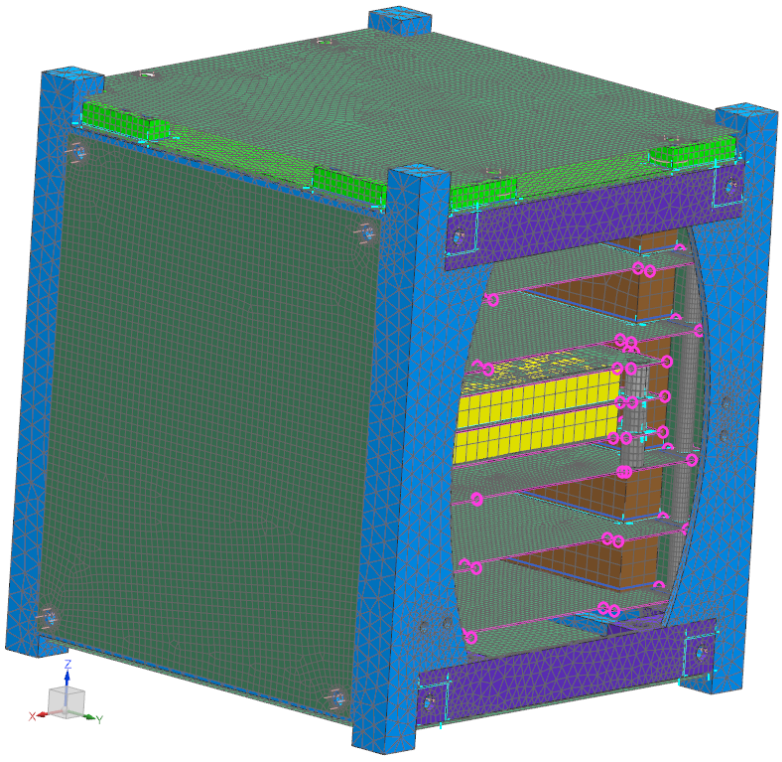

Figure 4.20: Idealized model converged mesh (dark green - solar panels and PCBs, light green - antenna, blue - side frames, purple - link arms, brown - PC/104 connectors, yellow - battery cells, grey - axes and battery spacers).

4.3.4 Loads and Boundary Conditions

Other fundamental parts of the construction of the FEM model are the applied loads and boundary conditions.

Contrary to the mesh that is the same for all analyses (except for the concentrated mass points), the boundary conditions might vary from one to the other. The common aspects will be presented in this section, while the differences will be presented in each respective analysis.

As mentioned in chapter 1, the CubeSat will be transported inside a deployer. This has some implications in terms of modelling and simulating the CubeSat.

During the launch, the loads that the launcher experiences are applied directly to the deployer and not the CubeSat. The loads suffered by the CubeSat itself will be different for the following reasons:

- Between the deployer rails and the side frames there is a slight gap, necessary for the CubeSat to be able to slide in and out of the deployer without issue and also as a result of potential manufacturing flaws or tolerances;
- The spring system, even though it is under tension, it is still able to contract and extend due to vibration;
- The CubeSats are not fixed or glued to each other, which means two adjacent CubeSats can become separated, a gap to be formed and then collide with each other repeatedly during launch. This also applies to the CubeSat adjacent to the spring plate.

For these reasons, the CubeSat will shake inside the deployer and the suffered loads will be the combined results of the launcher loads and the interaction effects between the deployer and the CubeSats, which are not known and are heavily randomized.

Due to the inherent complexity, it is not possible to easily replicate the exact launch boundary conditions in the FEM simulations.

In all FEA simulating launch conditions, the deployer and associated coupling effects will be neglected. This can be seen as the CubeSat being attached directly to the launch vehicle or as there being no gaps and no relative movement inside the deployer. And so, the loads provided by the launch authority can be applied directly to the CubeSat itself, without the need to model the deployer. However, while simplifying the analysis, this will also induce errors in the results.

When assembling the CubeSat, various bolts are used. The bolts are meant to attach and maintain connected the various components. To ensure that the bolt does not fail, pre-loads are applied to the bolts. This pre-load guarantees that the components remain clamped against each other and allows for the bolt to better distribute the load among the components and itself, instead of bearing the entire load, which would lead to the bolt failing.

This pre-load was applied to all simulations since in all of them the CubeSat is always assembled and the screws are screwed to the required torque. Applying equations 3.28, 3.29 and 3.30, where d_{nom} is 3 mm, σ_y is 490 MPa and a K_T of 0.2, a pre-load force and torque of approximately 2000 N and 1.2 Nm, respectively, are obtained.

During the launch, the loads can be divided into three groups. A static component related to the acceleration of the launcher, a dynamic one that results from the random vibration and acoustic noise of the rocket, and shock loads, associated with the separation of stages. The loads for the simulations all result from the design limit loads (DLL) imposed by the launch authority. Due to the aggressive environment of launch, all these loads are conservative and include significant safety factors, making them relatively bigger than what is most likely to be felt during launch. Safety factors (K_Q) are applied to the loads 'to guarantee adequate level of mechanical reliability for space flight hardware', as specified in ECSS documents [59]. The maximum value of K_Q is 2 and this is the value that will be used for the simulations.

Static Analysis

During the launch, the maximum static acceleration will be around 11 g. Due to the K_Q of 2, in the simulations, a total load of 22 g (215.82 $\mathrm{m/s^2}$) was applied. As the orientation of the deployer and therefore of the ISTSat-1 is not known beforehand, this analysis was made in all three directions (X, Y and Z). In each axis, the acceleration could have two orientations, but considering the near symmetrical structure the results would also be mostly symmetrical and there was no need to run these additional simulations.

For the static analysis, the direct attachment was modelled by fixing all nodes of the $-$Z side frame standoff faces and applying a slider constraint to all four side frame edges, meaning that the edges may only move in the Z direction.

Modal Analysis (Free Vibration Analysis)

As seen in chapter 3, in a modal analysis there are no external loads applied. The only exceptions were the bolt pre-loads, as those are forces that are always applied whenever the CubeSat is assembled.

As for the boundary conditions, these depended on the type of analysis that was intended. On the analysis simulating the launch, and as mentioned in section 4.3.2, rigid elements connected the side frames edges and stand-off bases to an external node. These four edges and four faces were chosen as they will be the CubeSat parts that will be in contact with the deployer during launch and to avoid over constraining the model. As these parts are connected by rigid elements to the external node, any DoF constraints applied to this node will be equally applied to all these parts. This way the side frames are still able to deform and both the PCBs and solar panels have no constraints besides the connections to other components. This configuration is known as 'hard-mounted configuration'. The external node was fixed in all six DoF.

For the correlation purposed analyses, free-free conditions were used instead and no DoFs had additional restrictions. In these simulations, the external node and rigid elements were not used.

As there are no forces applied in a modal analysis, there is no need to run a simulation for each axis, as was made in the static analysis.

4.3.5 Errors

Whenever one is working with the FEM, as important as the results themselves are the potential sources of errors that could contaminate the obtained results. If one is not aware of the potential errors, one can have no confidence in the results. Besides, only by being aware of where there can be errors, is it possible to take strategies to reduce these as much as possible, since in many cases, it is impossible to completely eliminate them.

These errors are related to the previous sections and the modelling decisions that were taken and are consolidated and resumed in the following list.

- Idealization errors: the FEM model has been subjected to a multitude of simplifications and approximations, meaning it is not an exact replica of the real ISTSat-1, both in the CAD, material choice and boundary conditions;
- Discretization errors: the continuum problem has been transformed into a discrete one, and the elements do not represent perfectly the CAD domain, due to complex geometry;
- Convergence errors: due to computational and time constraints, the mesh could only be refined until a certain point;
- Truncation errors: with more recent computers with higher precision, this error tends to be less significant.
- Human errors: incorrect data input, errors in the model, arising from data parameters, loads and boundary conditions patterns and results' misinterpretation.

These errors are all interconnected and if care is not taken, they can inflate each other, with the final result ending up being a completely wrong representation of reality.

On the other hand, there is not much point in trying to completely eliminate certain types of error, such as discretization errors, since there will still be other sources of errors, the obtained results will never be perfect and this elimination might come at a too high computational cost. Human errors are the only type of errors that are possible to eliminate in full, as long as attention is given to every step and through careful and thorough checks and rechecks of every step of the FEA.

This high number of sources of errors is also why it is so important to validate the FE results, to know if, after all, the errors are in a range that is acceptable by the user, and why safety factors are used. Finally, it is worth mentioning that this range of acceptability will always depend on the pretended level of accuracy, and the space sector tends to be highly demanding and any error has to be small enough.

4.4 FEA Results

Once the system has been modelled, properly defined and all assumptions, implications and shortcomings are well understood, the various simulations can be run.

Linear static analyses are usually the most simple analyses to run and, therefore, tend to be the first type of analysis that is run for any model, even when the intended results are obtained from some other type of analysis. With a static analysis, it is easier to verify that the entire model has been correctly set up, and will have associated shorter times of computation, allowing to have quicker convergence processes. If one starts immediately with a more complex type of simulation, simple errors might become hidden among other errors associated with the increase in complexity and become less apparent. A static analysis can also be used to determine if a non linear analysis is necessary.

For this specific case, the static analysis will not be done just for set up reasons, as it is also necessary for the actual results, due to the nature of loads experienced during launch, so that one can have confidence that the CubeSat will not fail during launch.

With a modal analysis, one can obtain the system's modal parameters, which can then be compared with the experimental modal parameters, as will be shown in chapter 6.

The computational results for both types of analysis are presented in the following sections.

4.4.1 Linear Static Analysis

The results for the displacement magnitude and Von-Misses stresses in the three loads conditions can be seen in Figures 4.21, 4.22 and 4.23. For the displacement, a linear scale is used. For the stress distribution, since the values are close to zero in most of the system, which would make the majority of the colour distribution uniform if a linear scale were to be used, a logarithmic scale is used instead.

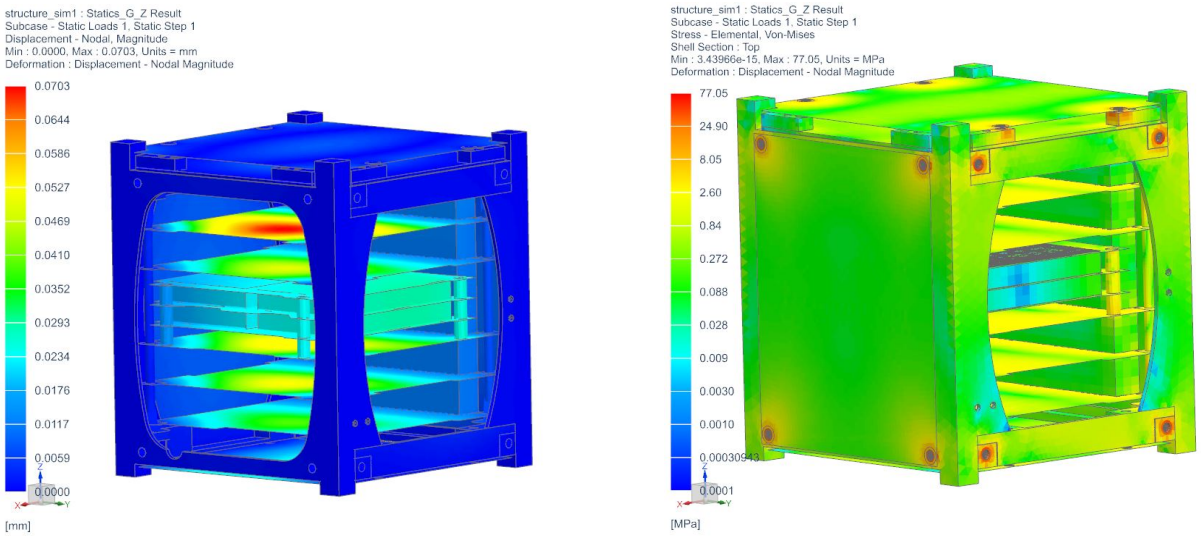

(a) Displacement magnitude (mm)

(b) Von-Mises stress (MPa)

Figure 4.21: Static analysis: Z axis.

The biggest displacement, of approximately 0.07 mm, occurs when the static load is applied in the Z direction of the CubeSat.

The aluminium structure is barely deformed, with the most relevant displacements occurring in the PCBs and the solar panels.

When the acceleration is aligned with Z, the PCB that deforms the most corresponds to the TTC, as

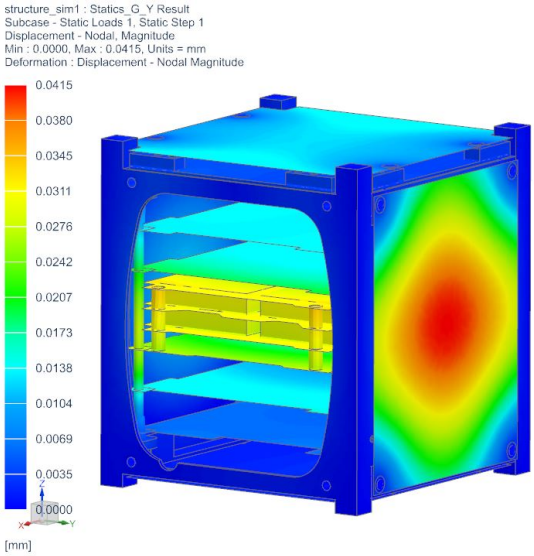

(a) Displacement magnitude (mm)

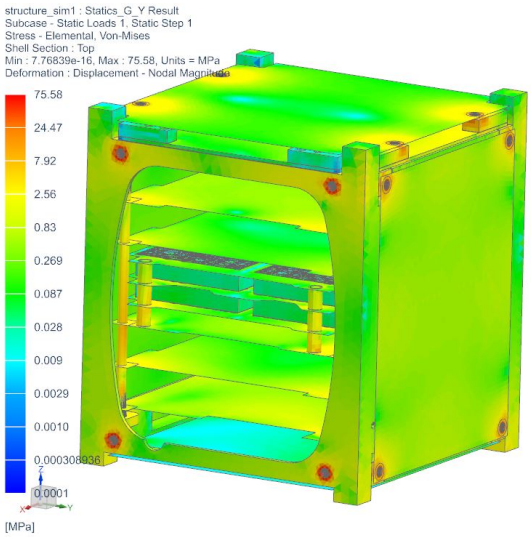

(b) Von-Mises stress (MPa)

Figure 4.22: Static analysis: Y axis.

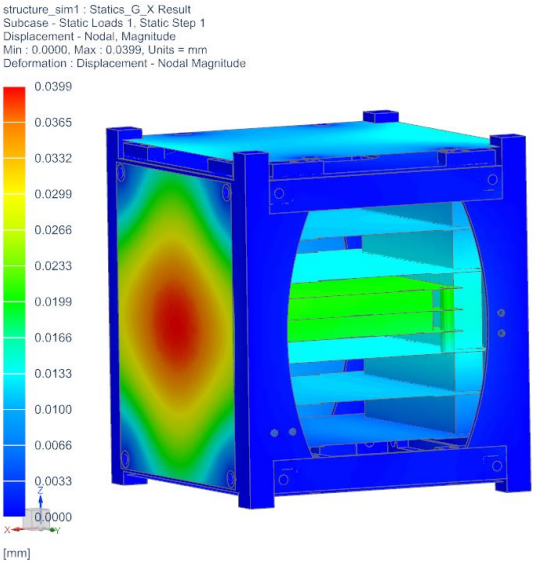

(a) Displacement magnitude (mm)

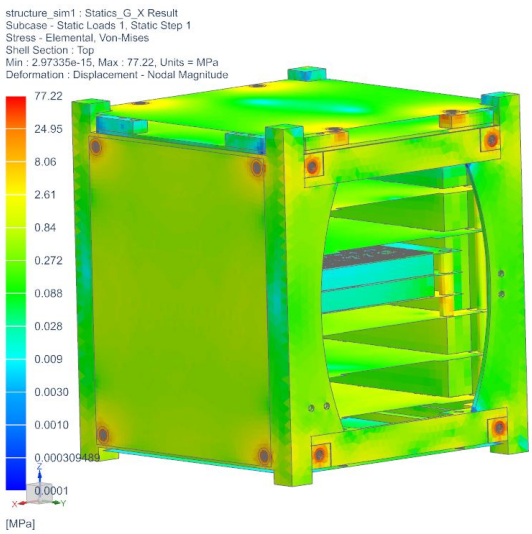

(b) Von-Mises stress (MPa)

Figure 4.23: Static analysis: X axis.

this is the PCB board with the most mass. As for the EPS, despite having more mass, when considering the entire board + battery subsystem, as the battery pack was modelled separately and has a significant volume and structure, the EPS board ends up being more rigid than the remaining PCBs and deforms less. It is also noticeable that the various PC104 connectors add a significant amount of rigidity to the PCB stack, as that part of the system barely deforms.

When the acceleration was in one of the horizontal directions (X and Y), the PCB Stack deformed as a whole, with mostly uniform deformation in each PCB and the Battery Pack having a slightly bigger displacement, but still smaller than the one registered for the vertical acceleration.

The SPs are most deformed when the acceleration is normal to them. For example, in the Y load case, the +Y SP deforms the most and away from the structure as the acceleration is normal to it. As

for the $-$Y SP, the acceleration would push it against the structure, constraining the displacement. It is possible to see that, regarding the SPs, there is a certain symmetry for the X and Y SPs, as they suffer similar deformations (in shape and magnitude) when aligned with the respective acceleration direction.

As all values of displacements are significantly below one millimetre, that is, below the average dimensions of the various components, it is shown that the small displacement assumption, used in linear analysis, was appropriate and can be used.

As for the stress distribution, the elements of greater stress, peaking at 77 MPa, are located around the bolt holes connecting the solar panels to the link arms, on both components. The similar distribution and magnitude across load orientations show that the main cause for these values of stress is not the static load itself, but the bolt pre-loads.

Despite the increased stress on the aforementioned locations, none of the obtained values are above the yield stress of the respective materials, with a large enough safety margin in most cases. This proves that the assumption of elastic behaviour was appropriate and that the risk of the structure yielding or failing is extremely low, even accounting for parts that were not modelled and might induce localized higher stresses than the ones computed.

4.4.2 Modal Analysis

As alluded to in section 4.3.4, when describing the boundary conditions, the modal analysis was divided into two situations.

The first is the situation where the launch itself, with the CubeSat inside a deployer, is simulated. This analysis, and the modes that are derived from it, are essential and serve as the foundation for all dynamic analyses, such as response in frequency and random vibration. And since those analyses are simulated with the CubeSat in the deployer, the modal analysis has to as well. Nevertheless, those simulations, namely the random vibration analysis, despite being simulations required by the launch authorities and necessary for the ISTSat project, will not be presented here, only the modal analysis that will serve as the foundation base to them.

The second is the situation where free-free conditions are simulated as if the CubeSat was floating in the air, as these were the conditions closest to those used experimentally, despite some details and limitations that are further explained in chapter 5.

During a modal analysis, the FEA program provides both the frequencies, the modes shapes and the effective modal mass.

Hard mounted configuration

During the launch, the frequencies induced by the launcher will be concentrated on the range from 20 Hz to 2000 Hz. As such, the modal analysis was focused on this range, despite some issues related to the amount of the total effective modal mass, as seen next.

For the specified range of frequencies, there were a total of 77 modes, with 52 of these having more than 0.1% of modal effective mass fraction. The total effective mass of the system contained in these

modes corresponds to 64.5% (X), 76.8% (Y) and 68.9% (Z) of the CubeSat's total mass, which is below the typical threshold of 80 or 90%. This might have an impact on future analyses that are based on the modes and this should be held into account when analysing results. Further modes besides the 20-2000 Hz range could be requested from the program, but this would come at a higher cost. As the system is extremely complex the number of modes is significantly high and as such each mode tends to have less m_{eff}, with this being especially true the higher the frequency of a mode is.

In table 4.3 the modes considered more important are presented. The frequency, the modal effective mass fraction in the three translation axis and a brief description of the mode are given.

Table 4.3: ISTSat-1 main modes in hard-mounted configuration.

Mode	Frequency (Hz)	Effective modal mass fraction			Mode description
		X	Y	Z	
1	346.4	8.9E-08	3.4E-06	0.096	TTC
2	413.8	0.0018	0.0010	0.17	COM
3	428.5	2.8E-05	0.0038	0.076	OBC & COM
4	437.7	0.0070	0.026	0.057	OBC & EPS
5	485.9	6.4E-04	0.31	0.025	PL & EPS
6	493.1	0.0013	0.074	0.0049	PL
8	498.5	0.049	6.1E-06	3.7E-05	$\pm$X SP
9	503.7	0.0012	3.9E-04	7.5E-04	$\pm$Y SP
11	572.2	0.15	0.010	0.027	ADS-B Antenna
12	574.4	0.0050	0.010	0.0020	TTC
14	586.6	6.4E-04	2.5E-06	0.029	+Z SP
15	611.7	0.024	0.0039	0.053	PCB Stack

The first modes are all related to the PCBs Boards. As all boards are made from the same material, and so have similar stiffness, since the TTC is the board with the most mass, by equation 3.24, it is the one with the lowest frequency, 346.44 Hz, also known as the fundamental frequency. This value is significantly above the one required by the launch authority, 130 Hz [60].

The EPS + Battery system has overall more mass than the TTC and so one could expect the frequency to be lower. However, as already explained for the static analysis, the separate modelling of the battery also increased that subsystem's stiffness, increasing its respective frequency. At a high enough frequency, 611.68 Hz, the entire PCB Stack starts to have associated modes as a whole.

Due to the relative symmetry of the system, the $\pm$X solar panels modes have the same frequency. Moreover, this mode has a similar, but not equal, frequency to the $\pm$Y pair. As for the $-$Z ADS-b Antenna and +Z SP, the existence of an antenna between the solar panel and the main structure leads to a difference of frequency and lack of symmetry between these two subsystems, contrary to the X and Y pairs.

As for the distribution of $\hat{m}_{\text{eff}_j}$, which indicates the relevance of a mode when the system is excited in a certain direction

- In the Z direction, it is more concentrated in the response of the PCB boards, mostly the COM, which concentrates almost one fifth of the effective modal mass. The solar panel in +Z has a smaller but still relevant response, while the solar panels parallel to Z have an insignificant response when the CubeSat is excited in the Z direction even if in the respective resonance frequency;

- In the X direction, it is mostly concentrated in the modes of the ADS-B antenna, the $\pm$X solar panels and PCB Stack as a whole. The relevance of the ADS-B antenna can be justified with the position of the bolts on the $\pm$Y sides of the structure, restraining the mode more in the Y direction and less in the X direction (see Figure A.6);

- Finally, in the Y direction, the most relevant response to an excitation in this direction is obtained in the mode related to the Battery, revealing the possibility of significant motion of this component during excitation.

While not presented here, it was seen that, in all directions, the higher the frequency of the mode the smaller the $\hat{m}_{\text{eff}_j}$ became, showing that the initial modes are more relevant, although the higher frequency ones cannot be completely disregarded.

Due to the difference in stiffness, for the analysed range no mode associated with the main structure was identified.

For illustrative purposes, some figures of the obtained modes are presented in Appendix A.

Free-free condition

For the free-free condition, the same range as the one used previously (20-2000 Hz) was used. However, due to experimental limitations (further detailed in chapter 5), in this section, only modes up to 1300 Hz will be shown. As will be seen in chapter 5, each component set-up and measurement was made sequentially and individually. This means a simulation was run for each component and that the addition of mass corresponding to the accelerometers was made separately across simulations (e.g., in the PL analysis the concentrated masses were only added to the PL, with no masses on the remaining components, identical to the experimental case).

In Tables 4.4, 4.5 and 4.6, are the modes frequencies for the free-free conditions analysis of the PL, EPS and +Y components, respectively. For simplicity of notation, and since each component was analysed separately, the numbering for the modes of each component will be done independently. This number does not correspond to the global identification when all modes of all components are considered. For example, the PL mode 1 is not the first global mode of the system (which is a TTC mode), but the first PL mode that was obtained on the simulation where the accelerometers' mass was added to the PL. The same logic applies to the numbering of the remaining components.

Table 4.4: PL modes in free-free condition.

Mode	Frequency (Hz)
1	407.9
2	631.2
3	748.2
4	762.3
5	1168.8
6	1195.4
7	1206.3
8	1280.8
9	1352.5

Table 4.5: EPS modes in free-free condition.

Mode	Frequency (Hz)
1	483.2
2	515.3
3	607.9
4	703.0
5	753.8
6	875.6
7	1008.8
8	1069.7

Table 4.6: +Y SP modes in free-free condition.

Mode	Frequency (Hz)
1	347.3
2	636.8
3	693.5
4	710.1
5	843.3
6	1352.8

Looking at the first mode frequency of each component and comparing with table 4.3, it can be seen that all these frequencies had a downwards shift when compared with the respective component and frequency. Since additional mass was added in these free-free simulations, from equation 3.24, one can see that this shift is expected and serves as a further check that the mass addition was defined correctly.

Chapter 5

Modal Test

In this chapter, the experimental results obtained from the modal testing of the ISTSat-1 will be presented. First, a detailed description of the ISTSat-1 model that was tested, the set-up, including all used equipment, software definitions and accelerometers positions, and the main sources of possible errors will be given in section 5.1. Then, in section 5.2, the experimental results will be presented. Due to the substantial amount of data that was collected, it is not possible to show all accelerometers' responses. Finally, in section 5.3, the modal fitting algorithm is applied to the data presented previously, and the modes that were extracted from the PL, EPS and +Y SP are presented.

5.1 Test Description and Procedure

5.1.1 System Under Test

As it was for the computational analysis, while the purpose is to analyse the ISTSat-1, the system under test will not be a replica of the satellite that will be launched.

The system under test was a non-functional replica of the ISTSat-1, including the entirety of the structure, the PCB Stack and all fasteners connecting the aforementioned components. It is referred to henceforth as the test model.

All bolts in the test model were torqued to the value defined previously (see section 4.3.4).

The differences between the test model and the CubeSat to be launched were as follow

- the solar panels were replaced by dummy solar panels, without photovoltaic cells;
- the ADS-B antenna was replaced by a dummy ADS-B antenna, made of FR4 instead of ceramic subtract;
- all wiring connecting the various subsystems, the ADS-B antenna and the SPs were not installed;

The dummy components were dimensionally equal to the real subsystems and had similar properties, only being substituted for precaution, considering the cost and fragility of some of the real components, namely the SPs. The total mass was 872 grams, with inertial properties identical to the real CubeSat.

5.1.2 Test Set Up

All experimental tests were performed at IST's Mechanical Engineering Department Vibrations Laboratory. The test set-up can be seen at Figure 5.1, with the corresponding schematic shown in Figure 5.2. Accelerometers were attached to the CubeSat and an impact hammer was used to excite the structure. Both the accelerometers and the impact hammer were connected to the same data acquisition system, which in turn was connected to a computer, where the measured data could be seen and analysed.

Figure 5.1: Test set-up.

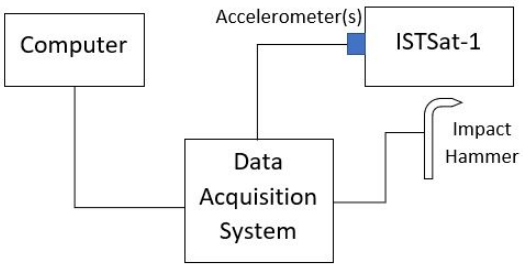

Figure 5.2: Test set-up schematic.

To emulate free-free conditions, the CubeSat was suspended from above with nylon line. The fishing line was passed in loops so that no knots were necessary, the line could slide with no restrictions and the CubeSat was as free-free as possible. When exciting the +Y solar panel the fishing line was passed through the gaps between the +Z solar panel and the dummy antenna (see Figure 5.3). When exciting the PL and EPS PCB boards, the fishing line was passed through the $-$Z bolt holes in the side frames (see Figure 5.4).

Figure 5.3: Test set-up: fishing line SP testing configuration.

Figure 5.4: Test set-up: fishing line PL testing configuration.

A Brüel & Kjær impact hammer Type 8202 was used to test the CubeSat, with the force transducer belonging to a PCB 208C01 model. The hammer was chosen over the shaker due to the simplicity of set up and testing and for the other advantages mentioned previously in section 3.6.1. The biggest consequence of this choice was the reduced precision of the excitation force, adding a (possibly significant)

source of error, as the excitation varied from run to run. A plastic tip, corresponding to the intermediate hardness (the others being rubber and steel), was used, with a nominal frequency range from 0 to 2000 Hz. However, these spectra (provided by the manufacturer) are usually obtained from tests on a solid steel cube and will not be the same for every structure. The hammer hit was always normal to the surface being impacted.

The accelerometers used were Brüel & Kjær DeltaTron Accelerometer Type 4397 and Type 4508. Both types of accelerometers were unidimensional, i.e., they only measure the acceleration in one direction. These accelerometers were used due to availability at the laboratory and due to their simplicity compared to other data measurement systems. The accelerometers were attached to the CubeSat by the use of bee wax as glue, allowing at the same time a strong fixture, but also an easy removal without damaging the components; and the measurement direction was always normal to the surface where they were attached.

The data acquisition system was composed of two modules of Brüel & Kjær Type 3050-A-060 (one with 6 input connections, the other with 4 input and 2 output connections). It is a six channel system with an input module of 50 kHz. The computer software used for visualization and processing of the measured data was Brüel & Kjær - Pulse LabShop Version 22.2.0.98.

For each measurement position, the CubeSat was hit five times, with the resulting FRFs being averages of the response on the five hits, allowing for the computation of the coherence function.

An exponential window with a shift of 500 μs and a τ of 10 ms was applied to all accelerometer measurements and a transient window with a shift of $1ms$ and a length of $3ms$ was applied to the impact hammer measurement.

As both the accelerometers and the impact hammer measure accelerations and force in the time domain, it is necessary to apply a FFT to transfer the data from the time to the frequency domain. The software was defined to compute the results with a frequency resolution of 0.5 Hz.

Considering the relative independence between components and the reduced number of available accelerometers, it was decided to analyse the various components results independently. This also simplified the analysis, by looking at the results by component. It was also tested and seen that when hitting on a certain solar panel, no good response was obtained on accelerometers attached at the opposing face. Due to the number of intermediate components between opposing faces and the high number of connections, as the vibration was propagated through the entire structure, the response was highly damped and full of noise. As such, when analysing the +Y face, it was the +Y that had to be hit with the impact hammer.

As the main structure (side frames and link arms) has no significant modes in the analysed frequency range (0 - 2000 Hz), no accelerometers were attached to these components.

For the PCB stack, ideally, the response of all PCB subsystems would have been measured. However, it was not possible due to lack of space. As the distance between PCBs is 10 mm, the same size as the height of the available accelerometers, there was not enough height to fit the accelerometers. Removing one of the boards to allow for more space was not feasible as the removal of a PCB and the corresponding PC/104 would affect the boundary conditions of the adjacent PCBs and change the

overall stiffness of the entire stack.

Therefore, the only PCBs that could be measured were the PL and EPS PCBs. The PL was located at the bottom of the stack ($-$Z), without other PCB nor electronic components at the bottom side. However, to be possible to excite the PCB with the impact hammer and also due to the reduced space between the PL and the ADS-B antenna, the payload antenna was removed, while the rest of the CubeSat remained as detailed in section 5.1.1.

As for the EPS, while most of the subsystem was inaccessible, due to the battery pack, there was a single small space near the axes ($-$X,$-$Y) where an accelerometer could be attached.

For the remaining PCBs, since it was not possible to obtain the response, it was assumed that the conclusions extracted from the analysis of the PL and EPS results can be extended to PCBs not measured.

5.1.3 Accelerometers Positions and Impact Locations

The accelerometers positions were obtained from the application of the Min-MAC algorithm (see section 3.6.4) to the following components: the +Y SP and the PL.

For the positions indicated in Figure 5.5, suggested by the algorithm, the auto-MAC matrix presented in Figure 5.6 was obtained, where only the +Y SP modes are compared. This matrix, resulting from the comparison of the computational modes to themselves, shows that the selected points of measurement are in sufficient number to be possible to identify clearly enough almost all relevant modes. Since the modes are being compared to themselves, the diagonal terms will be exactly 1 and are of no interest. Most off-diagonal terms are close to zero, showing that the shapes with the selected number of DoFs are distinct from each other. The only exceptions are modes 3 and 4, which have MAC close to 1, which shows that in the selected DoFs, the mode shapes are almost identical. However, due to the limitations mentioned beforehand and considering that this algorithm is only meant to provide suggestions and does guarantee that good correlation might still be achieved, these positions were nevertheless chosen.

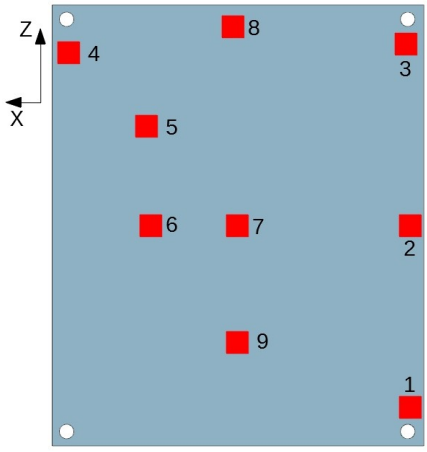

Figure 5.5: Accelerometer positions in +Y SP.

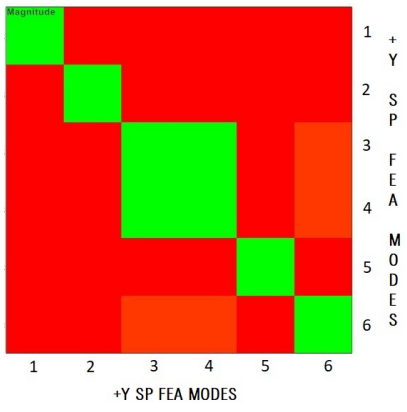

Figure 5.6: +Y SP: auto-MAC matrix - green = 1; yellow = 0.5; red = 0.

For the PL, the Min-MAC algorithm was applied in the same way. The final measurement positions for

the PL can be seen in figure5.7. For the EPS, as there was only one feasible position for an accelerometer due to the battery placement, there was no need nor possibility to apply the Min-MAC algorithm, and the final placement can be seen in Figure 5.8.

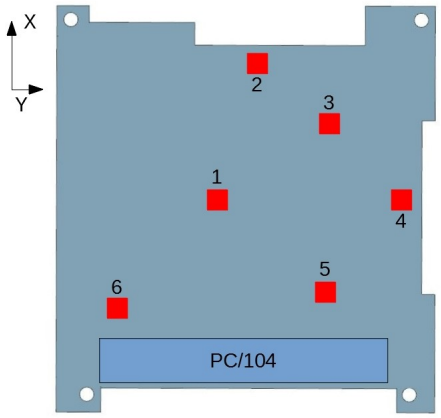

Figure 5.7: Accelerometer positions in PL.

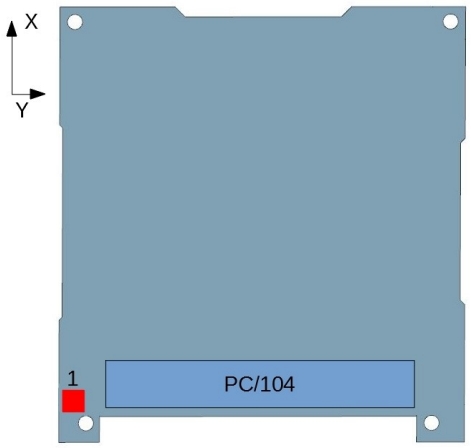

Figure 5.8: Accelerometer position in EPS.

To excite the components, the +Y SP was hit as close as possible to position 7 without hitting the accelerometer at that location, the PL was hit as close as possible to position 1 and the for the EPS, the link arm was hit as there was no possible location on the EPS itself.

5.1.4 Errors and Discrepancies

When performing experimental tests, it is of utmost importance to think and be aware of all potential sources of errors that can affect results. In an experimental test, there are many variables over which there is less control, contrary to theoretical or computational analysis, where many simplifications can be made to the model, which might more easily induce unexpected errors.

If no attention is given to potential errors, the results can easily give unexpected and completely different results from those obtained computationally. Besides, it is only possible to mitigate these errors if one is aware of where there can be sources of errors and discrepancies.

- Imperfection errors: while for the computational analysis, all materials and components were assumed to be perfect, any test model will have imperfections (e.g., material cracks) that are not known;
- Idealization errors: some assumptions, like the free-free condition, are only approximations;
- Human errors: the imprecision of the human hand adds some randomness to the entire procedure and results, mainly the impacting of the structure with the hammer;
- Instrumentation error: there will always be some noise associated with any measurement.

The high number of sources of errors is the reason why great care has to be taken on the treatment and interpretation performed after the test and presented in the following sections.

5.2 Experimental Results

5.2.1 Payload Subsystem

For the PL, the coherence of accelerometers all positions (Figure 5.9) and FRFs in both amplitude/phase and real/imaginary forms for PL position 1 (Figures 5.10 and 5.11) are presented.

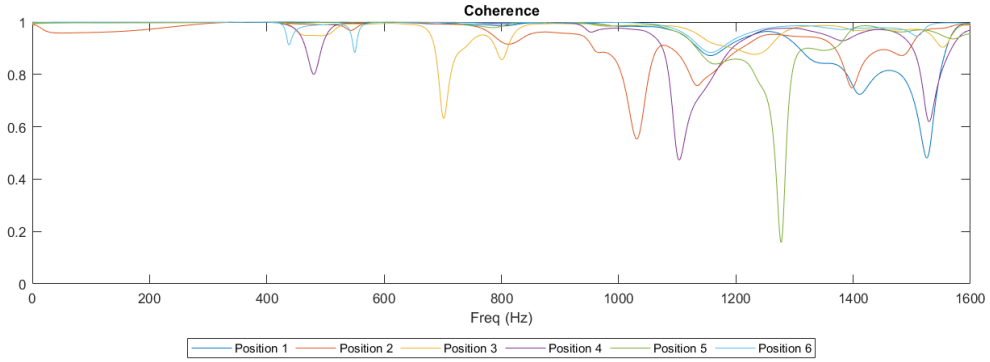

Figure 5.9: Coherence: PL.

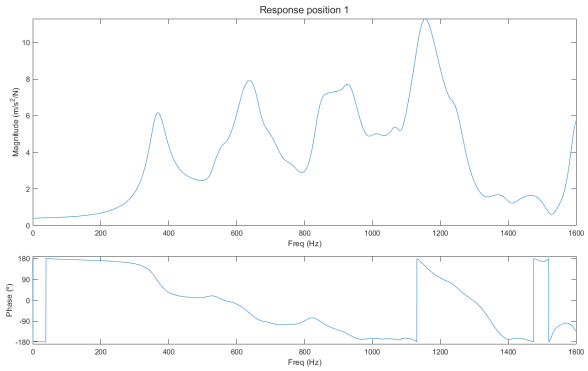

Figure 5.10: FRF (Amplitude/Phase form): PL position 1.

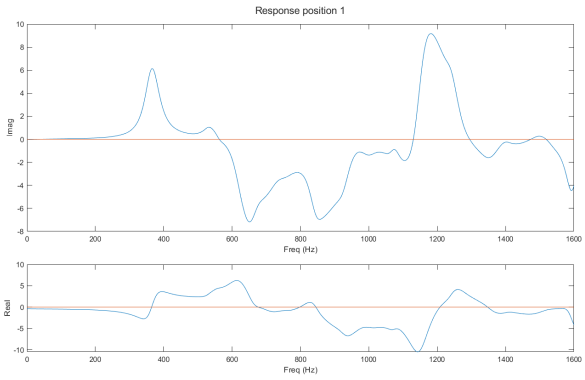

Figure 5.11: FRF (Real/Imaginary form): PL position 1.

In the coherence plot, it can be seen that the function is close to one across most of the spectrum up to 1000 Hz for all positions. While there are some dips in coherence before 1000 Hz, these become more frequent and accentuated above this frequency. This can be seen as evidence that the tip that was used for excitation did not excite the frequencies above 1000 Hz with the same quality as for those below 1000 Hz. Besides, as the PL was a subsystem with more difficult access than the SPs, there is a higher chance that the hammer impact was less regular among averaged hits, leading to these dips. As such, when extracting the modal parameters from these FRFs, it is to be expected lower quality modes from frequencies above 1000 Hz.

For the FRFs, plots with clear and noticeable peaks associated with the PL modes were obtained. A more detailed analysis of each natural frequency, damping coefficient and mode shape is made in the

next section. While not shown here, similar FRFs were obtained for each accelerometer position in the PL that was measured.

5.2.2 +Y Solar Panel

The coherence of all positions of the +Y solar panel (Figure 5.12) is shown. As for the PL, FRFs were obtained in each measurement location.

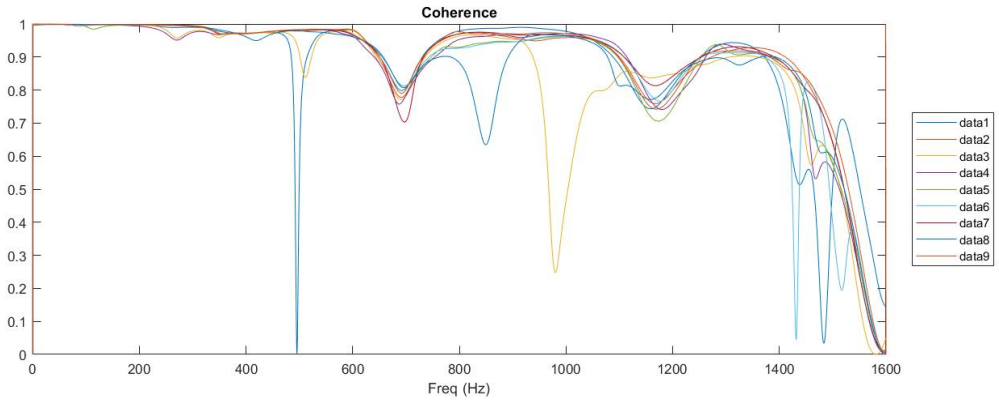

Figure 5.12: Coherence: +Y SP.

In the coherence for all accelerometers, it can be seen that most of the function is close to one across the spectrum, with some individual dips in one or another accelerometer that can be associated with a slightly worse impact. It is noticeable that from 1400 Hz, there is a generalized decrease of coherence in all accelerometers. This degradation showed that the quality of the response was not good enough beyond that frequency and therefore, when modal fitting, the response of these higher frequencies should be disregarded and greater focus was given to the lower frequencies modes.

In Figures 5.13 and 5.14 the hammer impact in both the time and frequency domain measured in one of the impacts is presented. These measurements were made to verify that no double impacts occurred and that the force was relatively continuous across the spectrum, to obtain plots similar to the examples seen in Figures 3.14 and 3.15. These checks were made for all measurements. The frequency domain plot is presented in dB and it can be seen that at 1000 Hz there was a drop of 10 dB of the force level.

5.2.3 EPS Subsystem

While measuring a single point does not allow to extract any modal shapes, it can still give some insight into the EPS behaviour and some of its mode frequencies. The FRF and the coherence for the measurement at EPS position 1 can be seen at Figure 5.15 and 5.16, respectively.

While coherence was low up to 400 Hz, as the first peak was only encountered above this frequency, this reduced coherence is not of much concern. As for the remaining spectrum, the coherence stays close to one, except for three frequencies where antiresonance occurs, including a significant dip around 1300 Hz.

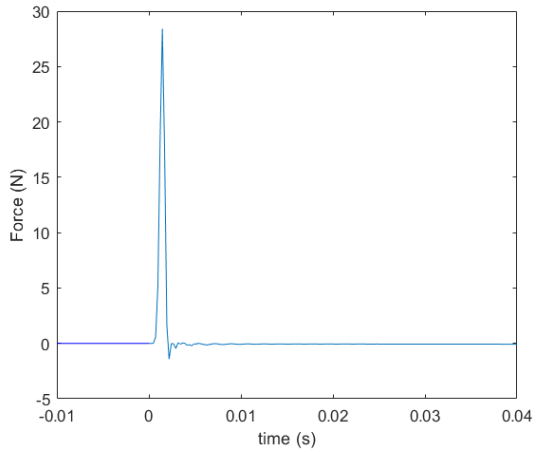

Figure 5.13: Impact response in time domain: +Y SP position 1.

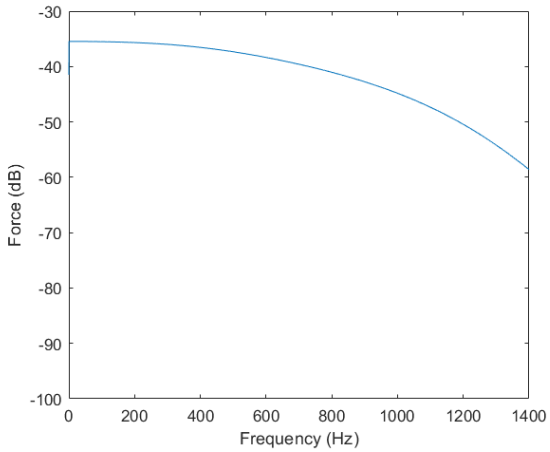

Figure 5.14: Impact response in frequency domain: +Y SP position 1.

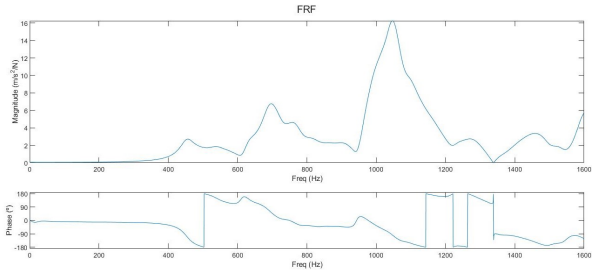

Figure 5.15: FRF: EPS position 1.

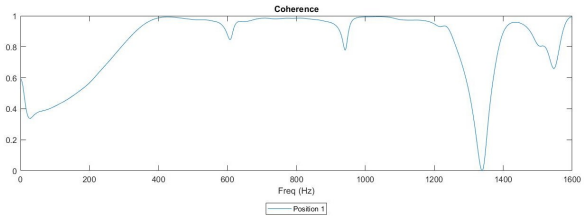

Figure 5.16: Coherence: EPS position 1.

5.3 Modal Fitting

Once the FRFs have been obtained, it is possible to extract the modal parameters through the application of a curve fitting algorithm. The LSRF method, which is implemented in MATLAB [61], was used for all extractions.

Once again, each component of the CubeSat was analysed independently and the LRSF method was applied to each component individually.

For this algorithm to work, it is necessary to provide the measured FRFs, the corresponding frequencies, the sample rate and an estimate of the number of modes to be found. Additionally, a frequency range might be defined, if only a specific part of the full measured range is of interest.

The output of this algorithm corresponds to the natural frequencies, the damping coefficients for each mode, the mode shape vectors and reconstructed FRFs based on the previous output.

To verify if the estimated number of modes was appropriate in the defined frequency range the reconstructed FRF is compared to the experimental FRF. If too many modes were estimated, the reconstructed FRF will tend to overshoot the experimental FRF, in some cases, by various orders of magnitude. If, on the other hand, too few modes were estimated, some peaks will be missing from the reconstructed FRF. In either case, the experimental and reconstructed FRFs will not have a good match, indicating some

error. In chapter 6, another method will be shown that further shows whether the estimated number of modes provided to the algorithm were adequate or not.

5.3.1 Payload Subsystem

For the PL, ten modes were extracted. The frequencies and mode damping coefficients can be seen in Table 5.1. The frequency range defined was [100,1400] Hz, as the reconstructed FRFs had worse quality if the range was extended to the entire measured range. The experimental and reconstructed FRFs for position 1 (the same position shown in section 5.2) can be seen at Figure 5.17, which show a relatively good fit on both the magnitude and phase, with no missing peaks in the reconstructed FRF.

Table 5.1: PL extracted modes' frequencies and damping coefficients.

Mode	Frequency (Hz)	Mode damping coefficient
1	365.8	0.072
2	517.6	0.046
3	651.8	0.071
4	686.5	0.050
5	831.6	0.044
6	948.6	0.052
7	1062.2	0.032
8	1155.0	0.033
9	1258.7	0.027
10	1356.0	0.023

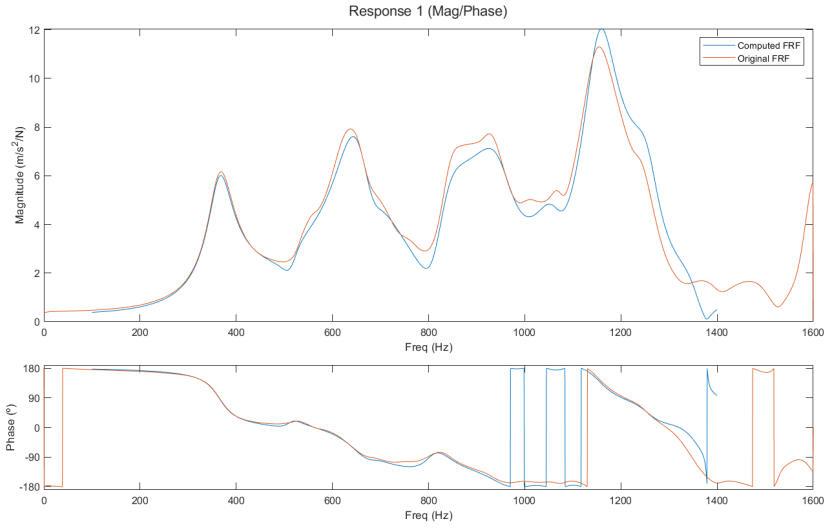

Figure 5.17: Experimental and reconstructed FRFs: PL position 1.

The first experimental mode of the PL is at 365.8 Hz. All modes have a damping coefficient of around

0.05 (5%), which is a typical value. Ten mode shapes, with 6 DoFs (corresponding to the six measured locations), were also obtained. While not shown here, reconstructed FRFs were obtained and compared with the originals for all six positions in the PL, showing a good fit.

5.3.2 +Y Solar Panel

For the +Y SP, seven modes were extracted. The frequencies and mode damping coefficients can be seen in Table 5.2. The frequency range defined was [100,1300], as the reconstructed FRFs had worse quality if the range was extended to the entire measured range. As it was for the PL, experimental and reconstructed FRFs for each position of the +Y SP were compared. The experimental and reconstructed FRFs for position 8 can be seen at Figure 5.18. While the match does not have the same quality as the ones obtained for the PL subsystem, it can still be seen that most modes were extracted correctly, with the most relevant peaks present.

Table 5.2: +Y SP extracted modes' frequencies and damping coefficients.

Mode	Frequency (Hz)	Mode damping coefficient
1	361.3	0.086
2	503.5	0.174
3	641.7	0.229
4	730.7	0.051
5	921.6	0.035
6	1071.9	0.035
7	1152.8	0.050

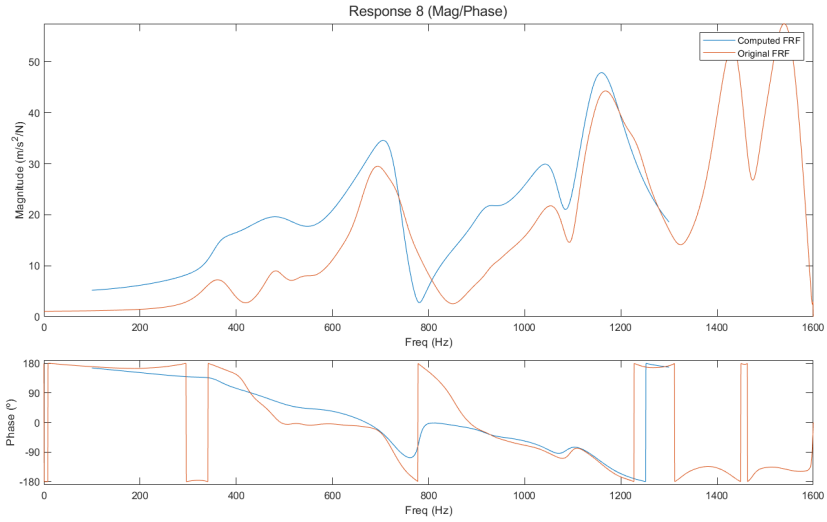

Figure 5.18: Experimental and reconstructed FRFs: +Y SP position 8.

The first experimental mode of the +Y SP is at 361.3 Hz. Seven mode shapes, with 9 DoFs (corre-

sponding to the nine measured locations), were also obtained.

5.3.3 EPS Subsystem

For the EPS, eight modes were extracted. The frequencies and mode damping coefficients can be seen in Table 5.3. The experimental and reconstructed FRFs can be seen in Figure 5.19. The frequency range defined was [100,1200], due to the dip in 1300 Hz that interfered with the quality of the reconstructed FRF when this frequency was included.

Table 5.3: EPS extracted modes' frequencies and damping coefficients.

Mode	Frequency (Hz)	Mode damping coefficient
1	452.2	0.044
2	550.3	0.082
3	624.8	0.028
4	694.5	0.036
5	764.2	0.023
6	971.9	0.028
7	1055.1	0.028
8	1091.7	0.033

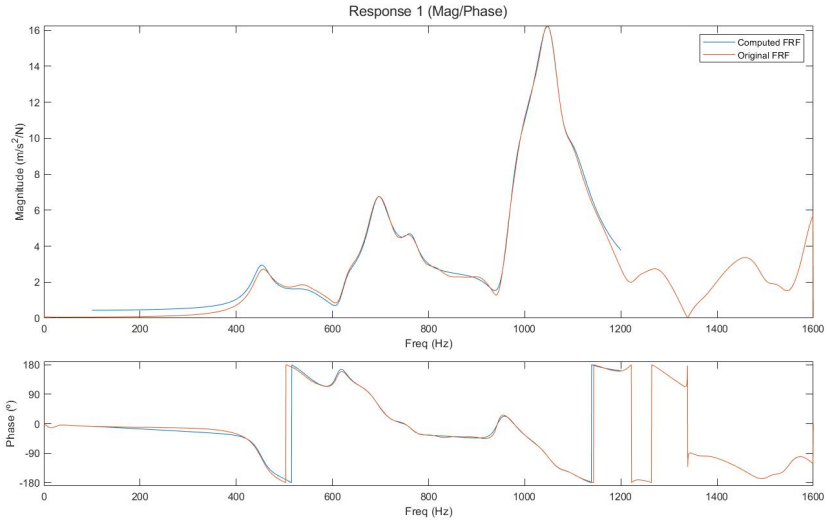

Figure 5.19: EPS experimental and reconstructed FRFs: position 1.

For the EPS the match between the experimental and reconstructed FRFs was almost perfect, as there was only one FRF to curve fit to. Nevertheless, this almost-perfect match does not guarantee that all modes of the EPS were extracted, as modes where the measured point corresponds to a nodal point do not appear and therefore cannot be extracted.

Chapter 6

FE-Experimental Correlation

Finally, with both the computational and the experimental results it becomes possible to compare both sets of results and validate the FE model. In this chapter, the comparison of the FE model presented in chapter 4 with the results obtained experimentally and presented in chapter 5 is done. In section 6.1, the distinction between model reduction and expansion is briefly presented. In section 6.2, the mode frequencies comparison and MAC matrix for each individual tested component are presented.

6.1 Model Reduction and Expansion

As mentioned in chapter 2 and further derived from analysis of the MAC expression (equation 3.37), to correlate the FEA mode shapes with the experimental mode shapes, both vectors have to have the same size.

Since the FE model has hundreds of thousands of DoFs more than the experimental results (25 DoFs, when all measured subsystems are considered), the two mode sets cannot be immediately compared with one another. So it becomes necessary to either reduce the FE model or expand the experimental set. As the expansion of the experimental would have to rely on the FE results, the experimental expanded vectors could be contaminated with FE errors. Therefore is simpler to reduce the FE model instead. And since the used correlation metric is the MAC, which does not take into account the mass matrix (as other correlation metrics do, like the Normalized Cross-Orthogonality - NCO), to reduce the FE model it is only necessary to compute the mode shapes and choose the DoFs that are located at the accelerometers' positions.

6.2 Frequency Comparison and MAC

The difference between the computational (f_{FE}) and experimental (f_{EXP}) mode frequencies, in percentage, is given by

$$\mathrm{dif} = \frac{f_{\mathrm{FE}} - f_{\mathrm{EXP}}}{f_{\mathrm{FE}}} \times 100\,. \tag{6.1}$$

6.2.1 PL

When comparing the 10 experimental modes in Table 5.1 to the 9 FEA modes in Table 4.4, the MAC matrix in Figure 6.1 is obtained. It can be seen that the three first modes of each set seem to be strongly correlated with diagonal terms close to 1 and off-diagonal terms close to zero. For the upper modes, the correlation between modes becomes less clear.

	FEM	1	2	3	4	5	6	7	8	9
EXP	Frequency	407.9	631.2	748.2	762.3	1168.8	1195.4	1206.3	1280.8	1352.5
1	365.8	0.954	0.042	0.005	0.001	0.027	0.006	0.009	0.017	0.022
2	517.6	0.004	0.898	0.079	0.079	0.009	0.012	0.010	0.007	0.004
3	651.8	0.010	0.042	0.915	0.830	0.015	0.079	0.092	0.021	0.013
4	686.5	0.031	0.116	0.024	0.043	0.594	0.029	0.023	0.686	0.633
5	831.6	0.025	0.004	0.430	0.336	0.125	0.504	0.511	0.177	0.134
6	948.6	0.049	0.057	0.201	0.164	0.058	0.599	0.617	0.062	0.061
7	1062.2	0.087	0.163	0.068	0.077	0.501	0.100	0.107	0.471	0.504
8	1155.0	0.084	0.076	0.231	0.225	0.233	0.199	0.182	0.603	0.544
9	1258.7	0.052	0.006	0.009	0.015	0.563	0.043	0.023	0.814	0.710
10	1356.0	0.047	0.096	0.017	0.057	0.810	0.160	0.183	0.585	0.646

Figure 6.1: MAC of all PL modes: green = 1; yellow = 0.5; red = 0.

Some experimental modes, like modes 5 or 7, do not have a good enough correlation to any FEA mode, which can indicate that these modes were not correctly estimated by the modal fitting algorithm.

Some FEA modes, like modes 8 or 9, have higher MAC for various experimental modes. However, by looking at the shapes of mode 8 and 9 (Figures 6.2 and 6.3, respectively), it can be seen that these modes are related to various subsystems and that in the PL, both modes have very similar shapes, and what distinguishes them are the shapes at the other components, like the TTC. This means that it is not possible to accurately correlate higher frequency modes while only measuring one PCB. This issue did not arise at lower frequencies (modes 1, 2 and 3) as in these modes only the PL was excited (see Figures 6.4 and 6.5) and so measuring just the PL was enough to obtain good correlation.

In the end, 6 modes can be more clearly correlated. The new MAC matrix with only these 6 modes can be seen in Figure 6.6. Most of the off-diagonal terms are close to zero, while in the diagonal, with exception of FEA mode 7, all modes are above 0.8. It is also relevant to notice that the frequency order changed, with FEA mode 6 correlating to a mode with higher frequency than the modes to which FEA modes 7 and 8 correlate. The frequency difference can be seen in Table 6.1. With exception of FEA mode 7, all correlated modes have frequency differences less than 20%. In most cases, except for FEA mode 6, which had a frequency ”switch”, the FEA modes had higher frequencies.

Comparing the MAC and the frequency shifts with the levels indicated in the ECSS Standard [13], it can be seen that for the PL ’fundamental’ mode the MAC was greater than 0.9 but the frequency shift was also greater than 3%. For the remaining modes, with exception of FEA mode 7, all met the requirement of MAC greater than 0.8; for the frequency deviation, which was to be below 10%, all failed, except for FEA mode 8.

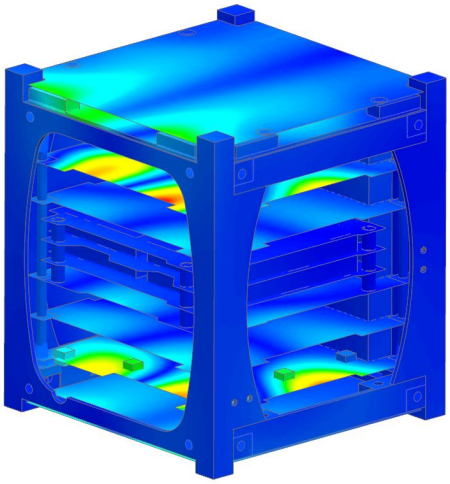

Figure 6.2: FEA PL mode 8: 1280.8 Hz.

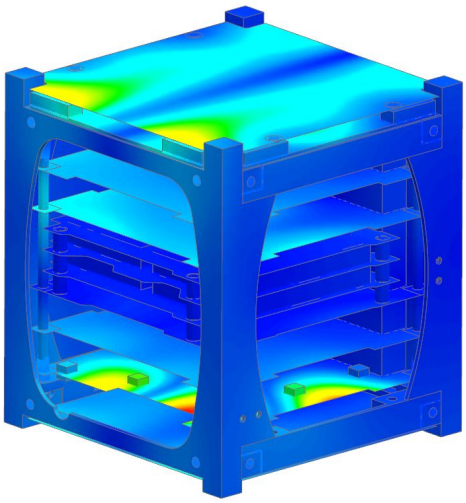

Figure 6.3: FEA PL mode 9: 1352.5 Hz.

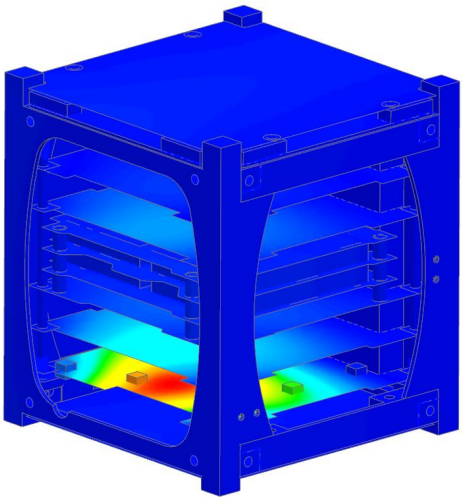

Figure 6.4: FEA PL mode 1: 407.9 Hz.

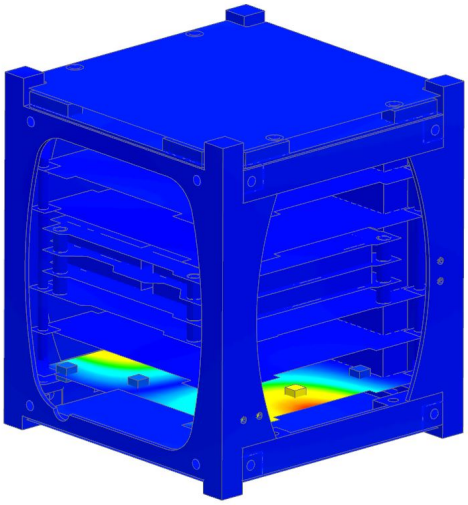

Figure 6.5: FEA PL mode 2: 631.2 Hz.

	FEM	1	2	3	7	8	6
EXP	Frequency	407.9	631.2	748.2	1206.3	1280.8	1168.8
1	365.84	0.954	0.042	0.005	0.009	0.017	0.027
2	517.61	0.004	0.898	0.079	0.010	0.007	0.009
3	651.81	0.010	0.042	0.915	0.092	0.021	0.015
6	948.62	0.049	0.057	0.201	0.617	0.062	0.061
9	1258.7	0.052	0.006	0.009	0.023	0.814	0.563
10	1356	0.047	0.096	0.017	0.183	0.585	0.810

Figure 6.6: MAC of selected PL modes: green = 1; yellow = 0.5; red = 0.

Table 6.1: PL modes' frequencies comparison.

FEA Mode	FEA frequency (Hz)	Experimental Mode	Experimental frequency (Hz)	Difference between frequencies (%)
1	407.9	1	365.8	10.31
3	631.2	2	517.6	18.00
4	748.2	3	651.8	12.88
7	1206.3	6	948.6	21.36
8	1280.8	9	1258.7	1.73
6	1168.8	10	1356.0	-16.02

6.2.2 +Y Solar Panel

When comparing the 7 experimental modes in Table 5.2 to the 6 FEA modes in Table 4.6, the MAC matrix in Figure 6.7 is obtained.

	FEM	1	2	3	4	5	6
EXP	Frequency	347.3	636.8	693.5	710.1	843.3	1352.8
1	361.3	0.913	0.024	0.054	0.065	0.029	0.010
2	503.5	0.295	0.081	0.605	0.657	0.025	0.137
3	641.7	0.338	0.119	0.532	0.579	0.061	0.103
4	730.7	0.043	0.777	0.051	0.139	0.163	0.020
5	921.6	0.345	0.170	0.389	0.406	0.017	0.021
6	1071.9	0.194	0.207	0.417	0.325	0.022	0.010
7	1152.8	0.137	0.298	0.201	0.218	0.175	0.040

Figure 6.7: MAC of all +Y SP modes: green = 1; yellow = 0.5; red = 0.

It can be noticed that for the +Y SP the correlations levels were not as good as they were for the PL. While the correlation is clear for the first modes of both the FEA and experimental results, for the higher frequency modes (FEA modes 5 and 6, experimental modes 5, 6 and 7) there was no correlation at all. For the intermediate frequencies, there was some level of correlation, although not as high as wished for.

Looking at just the modes with correlation and reordering them, the new MAC matrix with only 4 modes can be seen in Figure 6.8. It can be noticed that mode order in the FEA differs from the experimental one, with FEA mode 2 correlating to experimental mode 4. It can also be seen that FEA modes 3 and 4 are similar to each other, having similar MAC values for diagonal and non-diagonal MAC values, indicating the possible need for a greater number of accelerometers so that they can be clearly distinguished.

The frequency difference between the correlated modes can be seen in Table 6.2.

With exception of the first mode, all correlated modes have significant frequency shifts, above 10%,

	FEM	1	3	4	2
EXP	Frequency	347.3	693.5	710.1	636.8
1	361.3	0.913	0.054	0.065	0.024
2	503.5	0.295	0.605	0.657	0.081
3	641.7	0.338	0.532	0.579	0.119
4	730.7	0.043	0.051	0.139	0.777

Figure 6.8: MAC of selected +Y SP modes: green = 1; yellow = 0.5; red = 0.

Table 6.2: +Y SP modes' frequencies comparison.

FEA Mode	FEA frequency (Hz)	Experimental Mode	Experimental frequency (Hz)	Difference between frequencies (%)
1	347.3	1	361.3	3.87
3	693.5	2	503.5	-37.74
4	710.1	3	641.7	-10.66
2	636.8	4	730.7	12.85

showing the poorer quality results for the +Y SP.

Comparing the MAC and the frequency shifts with the levels indicated in the ECSS Standard [13], it can be seen that for the +Y SP 'fundamental' mode the MAC was greater than 0.9 and it almost met the frequency shift requirement of 3%, showing good correlation. For the remaining modes, neither the MAC levels nor the frequency shifts met the proposed levels. This shows that there is a poor correlation between the +Y SP FEA and experimental modes, indicating flaws either in the FEA model or in the experimental data measurements.

6.2.3 EPS

In Table 6.3 the comparison between the FEA and experimental modes is shown. As no mode shapes were available to apply the MAC to, the identification of corresponding modes was done by visual inspection of the FEA graphical plot, to see which modes had shapes with significant displacement in the accelerometer position.

Assuming that all experimental modes had correspondence to the FEA modes in the same order, all modes, except for one, had frequency differences less than 10%.

6.3 Discussion of Results

For the PL, a good correlation was verified for most modes (experimental and computational), especially those below 1000 Hz. But while the MAC level fulfilled the suggested requirements in the ECSS standards [13], showing that the FEA mode shapes are similar to the real ones, the discrepancies in

Table 6.3: EPS modes' frequencies comparison.

FEA Mode	FEA frequency (Hz)	Experimental Mode	Experimental frequency (Hz)	Difference between frequencies (%)
1	483.2	1	452.2	6.42
2	515.3	2	550.3	-6.79
3	607.9	3	624.8	-2.78
4	703.0	4	694.5	1.21
5	753.8	5	764.2	-1.38
6	875.6	6	971.9	-11.0
7	1008.8	7	1055.1	-4.59
8	1069.7	8	1091.7	-2.05

the frequency shifts were more significant and for most modes did not meet the standard requirements, indicating the need to adjust the material stiffness in the FEA, as changing the stiffness would impact the frequency of the modes, while the shapes would remain similar. Since for most modes the FEA frequency was higher, it can be concluded that the PL is overstiff in the FE model and the stiffness has to be reduced.

For the +Y SP, there were poorer correlation levels, except for the first mode. And while the first mode tends to be the one with greater effective mass and usually the most important, the lack of greater quality correlation for the remaining modes, does not allow to have full confidence in the FEA results as they currently are, requiring further study and testing. This lower correlation quality might result from: issues with the FE model, possibly in the way the connection between the solar panels and the structure was modelled or in the assumption of the solar panels as uniform boards; the way the CubeSat was suspended during +Y SP testing, that induced a lateral oscillation of the CubeSat of some magnitude, making it harder to hit consistently.

As for the EPS, despite having lower frequency shifts, the lack of MAC did not allow to take more meaningful conclusions about mode correlation. However, for most modes, it can be seen that FEA frequency was lower than the experimental one, meaning that in the FEA, the EPS was less stiff than the real one.

Chapter 7

Conclusions

This chapter presents the main conclusions of this work. In section 7.1 the major achievements obtained during this work are listed, which can be divided into three groups, as achievements related to the FEM component of this work, the experimental part and the validation segment. Finally, in section 7.2, some ideas for future work are presented.

While creating the FE model of the ISTSat-1, it became clear that despite the simplicity of the CubeSat compared to a more 'traditional' satellite, many simplifications and approximations were still necessary for the FE model to be of an approachable size and for the simulations to run in a timely fashion. All these simplifications introduced errors in the final computational results.

Nevertheless, the results for the static analysis showed that all stresses sustained by the CubeSat due to the static acceleration component of the launch loads are significantly below the yielding point and with a margin of more than enough to accommodate any error that might exist in the results. As for the modal analysis, in the hard-mounted condition, it was seen that the fundamental frequency was comfortably above the required level. In the free-free conditions simulations, the first natural frequency of each component became lower, due to the addition of the accelerometer masses, as expected, increasing confidence in the correct set-up of the model.

During modal testing, while the use of hammer excitation and accelerometers presented some physical limitations, mainly due to relative size and mass when compared with the CubeSat's size and weight, it was still possible to obtain good coherence measurements and FRFs with clear peaks associated to the components' modes. Still, for the chosen tip it only became possible to obtain good data up to 1400 Hz, not allowing correlation for the upper part of the frequency range experienced during launch (1400-2000 Hz).

When comparing computational and experimental frequencies and mode shapes, although not all ECSS requirements for the measured components were met, it was still possible to see that there was correlation between the FE and the experimental models (albeit in need of some FE model updates - see 'Good level of Correlation?' step in figure 2.1, chapter 1), increasing confidence in all obtained FE results (even those not present in this work, but that are required by the launch authority). And since these ECSS requirements were only suggestions, the actual levels that would be used for the FE model

to be considered validated and allow for the waiver or relief of the very intensive verification tests before launch would have to be discussed between the ISTSat team and ESA.

Nevertheless, despite the need for further updates, corrections, testing and analysis, it can be concluded that it is feasible and that it has a promising future potential, the use of impact hammer testing to obtain validated University-based CubeSats FEM models at a reduced amount of time and resources, despite the many physical limitations and reduced spacecraft size, increasing the confidence in FEA and reducing the need for an aggressive test campaign that might needlessly overstress the CubeSat before launch, incurring in costs that the University teams have no capacity to support.

7.1 Achievements

The major achievements of the present work are as follow:

- A detailed FE model of the ISTSat-1 and its main subsystems was created;
- The FE results showed that the ISTSat-1 meets the launch authority requirements regarding static loads and the fundamental frequency;
- A modal testing campaign that allowed for the extraction of the CubeSats' modal parameters was successfully carried out, providing a framework for future CubeSats' modal testing campaigns;
- For lower frequencies, the MAC yielded good values for the subsystems that were tested. For higher frequencies, while not so good values were obtained, these still allowed to verify the existence of correlation between modes;
- It was demonstrated that impact testing is possible and feasible to obtain validated University-based CubeSats FEM models.

7.2 Future Work

Based on the results and conclusions drawn from this work, the following ideas could be investigated and explored in greater detail.

- Update the FE model, namely the materials. As it was assumed that all PCBs and SP had the same properties (with exception of density), with the obtained experimental results it becomes possible to individually fine-tune the material of each PCB and see the impact that each PCBs' specific electronic components have on the overall stiffness.
- Use smaller accelerometers that allow for the testing and validation of the remaining PCBs that were not tested during the present work.
- Study and test with more detail the SPs response.

- Excite the structure with a shaker and compare the results to see if a shaker-based excitation provides clearer results than impact testing.
- Use other correlation metrics and compare the results with the ones obtained with MAC.
- Finally, as this work is integrated into the ISTSat project, one of the most important objectives with great future potential would be the application of all the work that was presented here to future CubeSats developed by the team, namely the ISTSat-Q. Contrary to the present work, which was performed at a late stage of the development phase of ISTSat-1, the structural analysis and validation of the ISTSat-Q could be developed from an early phase, allowing for a meaningful impact and improvement on the CubeSat structure.

Bibliography

[1] H. Jones. NASA Technical Reports Server (NTRS). In *48th International Conference on Environmental System*, Albuquerque, New Mexico, July 2018.

[2] C. A. Knight, M. Remedia, and G. S. Aglietti. A Methodology for Reducing Overtesting on Spacecraft Structure Equipment. In *2018 AIAA/ASCE/AHS/ASC Structures, Structural Dynamics, and Materials Conference*, page 1996. American Institute of Aeronautics and Astronautics, Jan. 2018. doi: 10.2514/6.2018-1996. URL `https://arc.aiaa.org/doi/abs/10.2514/6.2018-1996`.

[3] G. Konecny. SMALL SATELLITES – A TOOL FOR EARTH OBSERVATION?

[4] Cal Poly – San Luis Obispo CA. CubeSat Design Specification Rev 14, July 2020.

[5] NASA. CubeSat 101: Basic Concepts and Processes for First-Time CubeSat Developers. Oct. 2017.

[6] M. Swartwout. The First One Hundred CubeSats: A Statistical Look. *Journal of Small Satellites*, 2 (2):213–233, 2013.

[7] E. Kulu. Nanosats database. `https://www.nanosats.eu/`, Accessed on 19^{th} March 2021.

[8] NASA. State-of-the-Art Small Spacecraft Technology, Oct. 2020.

[9] J. P. Monteiro, R. Afonso, and J. Pinto. ISTSat-1 – The First Portuguese University CubeSat. *13th Congress of the Portuguese Comitee of URSI*, 2019.

[10] E. ECSS Secretariat. ECSS-E-HB-32-26A - Spacecraft mechanical loads analysis handbook, Feb. 2013.

[11] E. ECSS Secretariat. ECSS-E-ST-32-03C – Structural finite element models, July 2008.

[12] E. ECSS Secretariat. ECSS-E-ST-10-03C - Testing, June 2012.

[13] E. ECSS Secretariat. ECSS-E-ST-32-11C - Modal survey assessment, July 2008.

[14] M. B. V. Guedes. Cubesat Structural and Thermal Analysis Methodology ISTsat-1 Design. Master's thesis, Instituto Superior Técnico, University of Lisbon, June 2019.

[15] S. S. Rao. *Mechanical Vibrations*. Prentice Hall, 5^{th} edition, 2011.

[16] J. N. Reddy. *An Introduction to the Finite Element Method*. McGraw-Hill, 3^{rd} edition, 2006.

[17] V. Adams and A. Askenazi. *Building Better Products with Finite Element Analysis*. Onword Press, 1998.

[18] B. Akan. *CUBESAT STRUCTURAL ANALYSIS AND DESIGN*. PhD thesis, Istanbul Technical University, July 2020.

[19] B. Kelsey, C. Anderson, N. Petilli, and R. Cuerdon. Mechanical Design, Structural and Thermal Analysis for a 6U eLEO CubeSat. Master's thesis, Worcester Polytechnic Institute, Massachusetts, USA, Mar. 2020.

[20] E. E. Bürger, G. Loureiro, R. Z. G. Bohrer, L. L. Costa, C. Hoffmann, D. Zambarno, and G. Jaenisch. Development and Analysis of a Brazilian CubeSat Structure. In *22nd International Congress of Mechanical Engineering*, Nov. 2013.

[21] C. Born. Structural Design Methodology and Analysis for Small-Sats/CubeSats. *Honors Projects and Posters, Iowa State University*, Jan. 2019.

[22] G. I. Barsoum, H. H. Ibrahim, and M. A. Fawzy. Static and Random Vibration Analyses of a University CubeSat Project. *Journal of Physics: Conference Series*, 1264, July 2019.

[23] V. M. Chau and H. B. Vo. Structural Dynamics Analysis of 3-U CubeSat. *Applied Mechanics and Materials*, 894:164–170, 2019.

[24] E. ECSS Secretariat. Ecss-e-st-10-02c – verification, Mar. 2009.

[25] A. Ampatzoglou and V. Kostopoulos. Design, Analysis, Optimization, Manufacturing, and Testing of a 2U Cubesat. *International Journal of Aerospace Engineering*, June 2018.

[26] J. J. Furtal. Structural Design and Finite Element Analysis of DESCENT CubeSats. Master's thesis, York University, Toronto, Ontario, Canada, Aug. 2019.

[27] D. Mori, A. Ishikawa, H. Seki, and R. Funase. Structural Design of Lunar CubeSat EQUULEUS and Lessons Learned for Future Missions. In *Proceedings on the 32nd ISTS*, Fukui, Japan, June 2019.

[28] K. Nakaya, K. Konoue, H. Sawada, K. Ui, H. Okada, N. Miyashita, M. Iai, and S. Matunaga. Tokyo Tech CubeSat: CUTE-I - Design & Development of Flight Model and Future Plan. In *21st International Communications Satellite Systems Conference and Exhibit*. American Institute of Aeronautics and Astronautics, Apr. 2003.

[29] M. Remedia, G. Aglietti, M. Appolloni, A. Cozzani, and A. Kiley. An enhanced methodology for spacecraft correlation activity using virtual testing tools. *Journal of Sound and Vibration*, 409:180–200, Nov. 2017. doi: 10.1016/j.jsv.2017.07.054.

[30] R. Allemang. The modal assurance criterion - Twenty years of use and abuse. *Sound & vibration*, 37:14–23, Aug. 2003.

[31] T. G. Carne and C. R. Dohrmann. A modal test design strategy for model correlation. Technical Report SAND-94-2702C; CONF-950240-4, Sandia National Labs., Albuquerque, NM (United States), Dec. 1994.

[32] G. Pierlot. Oufti-1 : flight system configuration and structural analysis. Master's thesis, University of Liège, Liège, Belgium, June 2009.

[33] R. J. Guyan. Reduction of stiffness and mass matrices. *AIAA Journal*, 3:380–380, 1965. ISSN 0001-1452. doi: 10.2514/3.2874.

[34] G. Aglietti, S. Walker, and A. Kiley. On the use of SEREP for satellite FEM validation. *Engineering Computations*, 29(6):580–595, Aug. 2012. ISSN 0264-4401. doi: 10.1108/02644401211246292.

[35] J. F. Mercer, A. M. Kiley, and G. S. Aglietti. BepiColombo: sine test FEM correlation experiences. In *Proceedings of ISMA2014*, volume Proceedings of ISMA2014 of *Dynamics of aerospace structures*, pages 835–849, Leuven, Sept. 2014.

[36] J. F. Mercer, G. S. Aglietti, M. Remedia, and A. Kiley. An assessment of spacecraft target mode selection methods. *Acta Astronautica*, 140:537–553, Nov. 2017. ISSN 0094-5765. doi: 10.1016/j.actaastro.2017.09.013.

[37] J. Mercer, G. S. Aglietti, M. Remedia, and A. Kiley. Investigations concerning the effectiveness of the spacecraft finite element model correlation and update process. Toulouse, France, 2016.

[38] S. Manzato, B. Peeters, R. Osgood, and M. Luczak. Wind turbine model validation by full-scale vibration test. *European Wind Energy Conference and Exhibition 2010, EWEC 2010*, 5, Jan. 2010.

[39] D. Ribeiro, R. Calçada, R. Delgado, M. Brehm, and V. Zabel. Finite element model updating of a bowstring-arch railway bridge based on experimental modal parameters. *Engineering Structures*, 40:413–435, July 2012. ISSN 0141-0296. doi: 10.1016/j.engstruct.2012.03.013.

[40] A. F. Bower. *Applied Mechanics of Solids*. CRC Press, 1^{st} edition, Oct. 2009.

[41] G. T. Mase and G. E. Mase. *Continuum Mechanics for Engineers*. CRC Press LLC, 2000 N.W. Corporate Blvd., Boca Raton, Florida 33431, 2^{nd} edition, 1999.

[42] Y.-c. Fung. *A First Course in Continuum Mechanics for physicial and Biological Engineers and Scientists*. Pearson, 3^{rd} edition, July 1993.

[43] R. v. Mises. Mechanik der festen körper im plastisch- deformablen zustand. *Nachrichten von der Gesellschaft der Wissenschaften zu Gottingen, Mathematisch-Physikalische Klasse*, 1913:582–592, 1913.

[44] N. M. M. Maia, J. M. M. Silva, J. He, N. A. J. Lieven, R. M. Lin, G. W. Skingle, W.-M. To, and A. P. V. Urgueira. *Theoretical and Experimental Modal Analysis*. Research Studies Press LTD., 1997.

[45] J. R. Wright and J. E. Cooper. *Introduction to Aircraft Aeroelasticity and Loads*. Aerospace Series. John Wiley & Sons Ltd,, 2^{nd} edition, Dec. 2014.

[46] T. Irvine. Modal Participation Factor, Dec. 2015.

[47] F. P. Beer, J. E. Russell Johnston, J. T. DeWolf, and D. F. Mazurek. *Mechanics of Materials*. McGraw-Hill, 6^{th} edition, 2012.

[48] R. G. Budynas and J. K. Nisbett. *Shigley's Mechanical Engineering Design*. McGraw-Hill series in mechanical engineering. McGraw-Hill, 9^{th} edition, 2011.

[49] ASME. B1.13m - metric screw threads: M profile, 2005.

[50] R. Bracewell. *The Fourier Transform & Its Applications*. McGraw-Hill, 3^{rd} edition, June 1999.

[51] P. Avitable. *Modal Test: A Practitioner's Guide*. Wiley/SEM Series on Experimental Mechanics. John Wiley & Sons Ltd, 1^{st} edition, 2017.

[52] C. Sanathanan and J. Koerner. Transfer function synthesis as a ratio of two complex polynomials. *IEEE Transactions on Automatic Control*, 8(1):56–58, Jan. 1963. ISSN 1558-2523. doi: 10.1109/TAC.1963.1105517. Conference Name: IEEE Transactions on Automatic Control.

[53] R. van Herpen, T. Oomen, and M. Steinbuch. Optimally conditioned instrumental variable approach for frequency-domain system identification. *Automatica (Journal of IFAC)*, 50(9):2281–2293, Sept. 2014. ISSN 0005-1098. doi: 10.1016/j.automatica.2014.07.002.

[54] A. A. Ozdemir and S. Gumussoy. Transfer Function Estimation in System Identification Toolbox via Vector Fitting. *IFAC-PapersOnLine*, 50(1):6232–6237, July 2017. ISSN 24058963. doi: 10.1016/j.ifacol.2017.08.1026. URL `http://arxiv.org/abs/2003.06289`.

[55] N. M. M. Maia. *Extraction of valid modal properties from measured data in structural vibrations*. PhD thesis, Imperial College of Science, Technology and medicine - University of London, London, Dec. 1988.

[56] T.-I. Lee, C. Kim, M. S. Kim, and T.-S. Kim. Flexural and tensile moduli of flexible FR4 substrates. *Polymer Testing*, 53:70–76, Aug. 2016.

[57] M. Herrmann. Packaging - Materials review. In *AIP Conference Proceedings 1597*, pages 121–133, Freiberg, Germany, 2014. doi: 10.1063/1.4878483. URL `http://aip.scitation.org/doi/abs/10.1063/1.4878483`.

[58] SIEMENS. Element library reference, 2014.

[59] E. ECSS Secretariat. ECSS-E-ST-32-10C - Structural factors of safety for spaceflight hardware, Aug. 2019.

[60] J. A. E. Agency. Jx-espc-101133-b - jem payload accommodation handbook - vol. 8 - small satellite deployment interface control document, Jan. 2015.

[61] MathWorks. Modal parameters from frequency-response functions - matlab modalfit. https://www.mathworks.com/help/signal/ref/modalfit.html, acessed 16 June 2021.

Appendix A

Hard mounted configuration modes

For illustrative purposes, so that a notion of the hard mounted configurations mode shapes can be had, some figures are presented in this appendix.

In images A.1 to A.8, some of the modes indicated in table 4.3 can be seen. The values on the scale, in millimetres, only serve as a relative indicator between the displacement of different nodes, not representing actual displacements. The similar shape between PCB modes is evident.

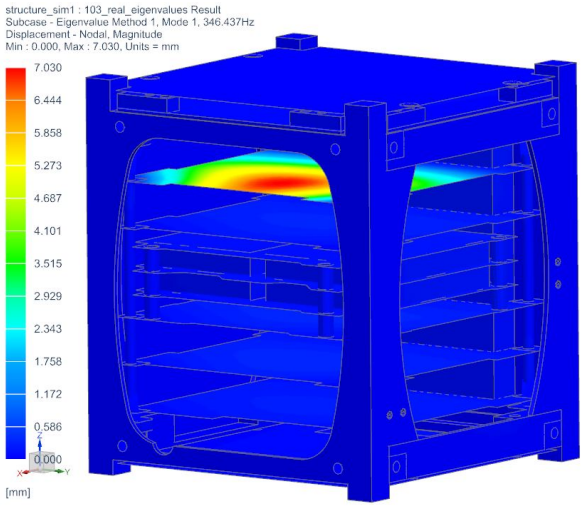

Figure A.1: ISTSat-1 Mode 1: TTC (Hard mounted configuration).

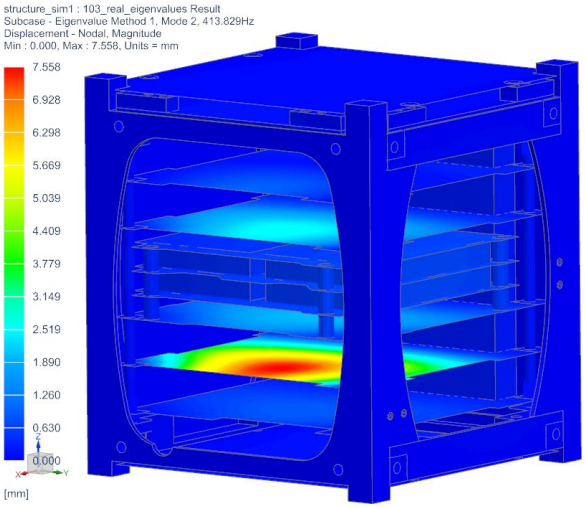

Figure A.2: ISTSat-1 Mode 2: COM (Hard mounted configuration).

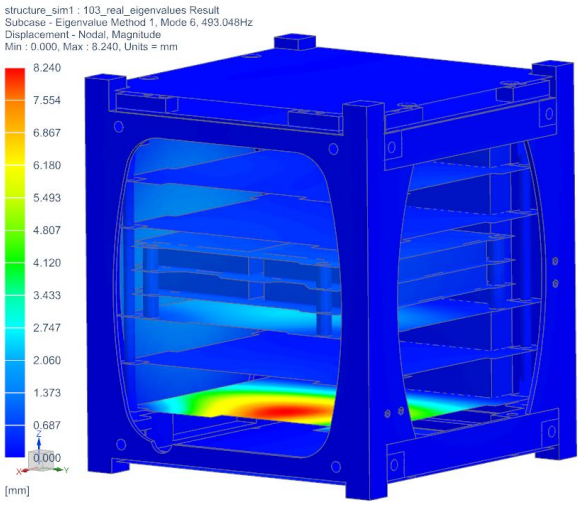

Figure A.3: ISTSat-1 Mode 6: PL (Hard mounted configuration).

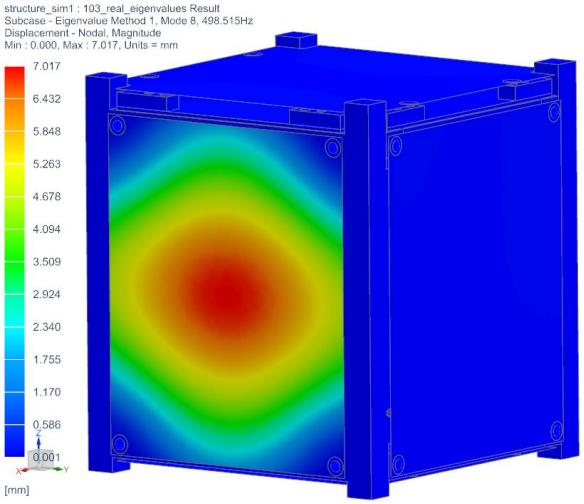

Figure A.4: ISTSat-1 Mode 8: $\pm$X Solar Panels (Hard mounted configuration).

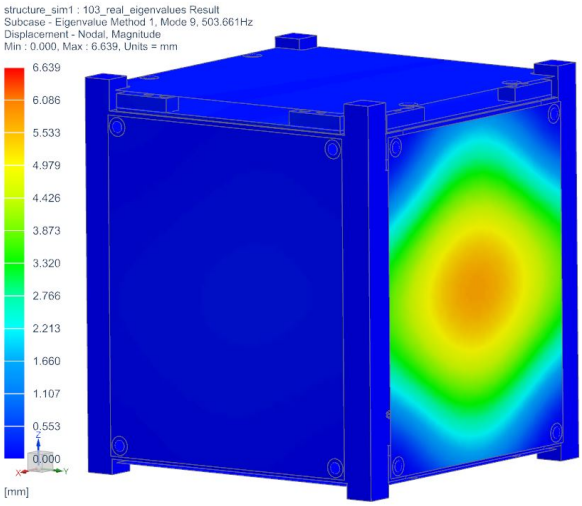

Figure A.5: ISTSat-1 Mode 9: $\pm$Y Solar Panels (Hard mounted configuration).

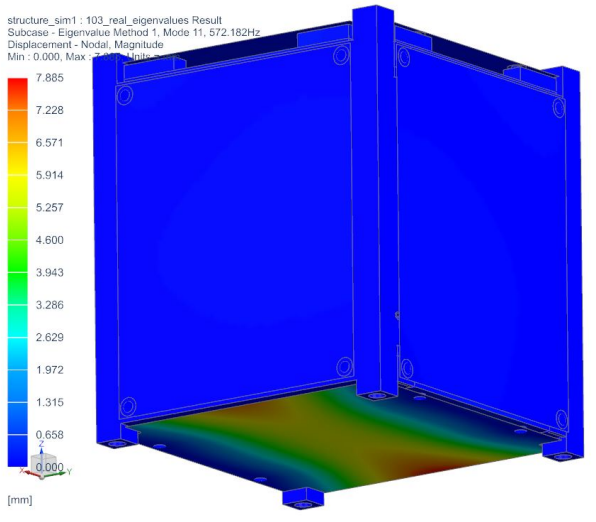

Figure A.6: ISTSat-1 Mode 11: -Z Patch Antenna (Hard mounted configuration).

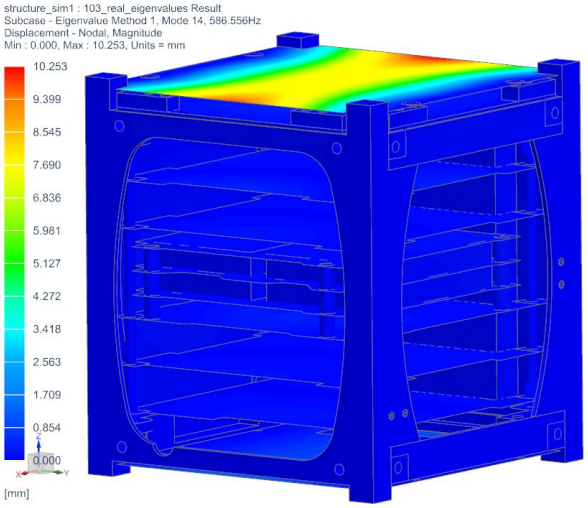

Figure A.7: ISTSat-1 Mode 14: +Z Solar Panel (Hard mounted configuration).

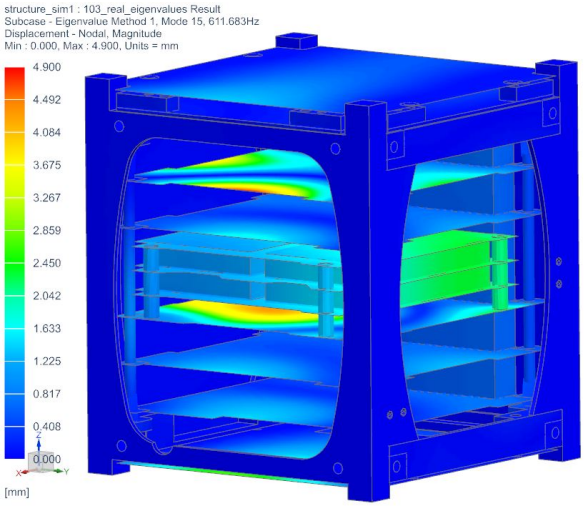

Figure A.8: ISTSat-1 Mode 15: PCB Stack (Hard mounted configuration).